ANALYSIS OF PACKAGING AND DEPLOYMENT OF ULTRALIGHT SPACE STRUCTURES

Thesis by

Lee Wilson

In Partial Fulfillment of the Requirements

for the Degree of

Doctor of Philosophy

California Institute of Technology

Pasadena, California

2017

(Defended April 25, 2017)

Lee Wilson

ORCID: [0000-0002-5865-9903]

Acknowledgments

Out of all people who helped me get to this point, the most deserving of my thanks is my advisor, Professor Sergio Pellegrino, who has gone above and beyond in his support and advice. His hands on approach has kept me on track and focused on solving interesting research questions. His tireless support has helped me finally make it to the end of the PhD journey.

I am also grateful for my fellow graduate student and post-doc collaborators, including Christophe Leclerc, Manan Arya, Miguel Bessa, and James Umali, for enabling my research.

To the fellow members of the AAReST project, who I have spent hours discussing spacecraft design and testing with, thank you. In particular Dr. Federico Bosi for sharing the hours spent by the shake table, Dr. Nicolas Lee and Dr. Steve Bongiorno for being able to bounce microsatellite subsystem design ideas off, and Serena Ferraro for carrying on the design and testing of the subsystem I poured my heart and soul into. I am also grateful to Dr. Gregory Davis, John Baker, and Dr. James Breckinridge for advice and mentorship.

Of course I also want to thank the Caltech staff for helping me with the more hands on aspect of my research, in particular Petros Arakelian for help in the lab, and John van Deusen, Joe Haggerty, and Ali Kiani for advice in machining and design. Thanks also to Kate Jackson, Christine Ramirez, and Dimity Nelson who kept the administrative part of my work running smoothly.

And of course, I want to thank my fellow members of the Space Structures Laboratory, for ideas, discussion, and support, including but not limited to Dr. Melanie Delapierre, Dr. John Steeves, Dr. Kristina Hogstrom, Thibaud Talon, Dr. Keith Patterson, Dr. Ignacio Maqueda Jimenez, Dr. Xin Ning, Yuchen Wei, Maria Sakovsky, and Gina Olson.

Finally, last but certainly not least, thanks so much to my family and friends.

Abstract

This thesis presents a new approach to modeling in finite element analysis (FEA) creased thin-film sheets such as those used for drag sails, as well as modeling the packaging behavior of coilable deployable booms. This is highly advantageous because these deployable space structures are challenging to test on the ground due to their lightweight nature and the effects of gravity and air resistance. Such structures are utilized in the space industry due to their low mass and ability to be packaged into a small volume during their launch into space.

It is shown that removing the crease bending stiffness in creased sheets still allows the deployment behavior of a benchmark problem to be captured, including deployment forces and equilibrium configurations. In addition, folding creased sheets from a flat state into a packaged configuration can result in crease crumpling and excessive wrinkling. To avoid this the Momentless Crease Force Folding (MCFF) technique is developed.

Further presented is the behavior of tape springs and Tubular Rollable and Coilable (TRAC) booms when coiled to radii greater than their natural bend radius. Under these conditions the booms can form multiple localized folds which may jam during boom deployment. Understanding this behavior is important for extending the use of these booms to large scale space structures such as orbital solar power stations.

A useful analytical model is developed determining when the localized folds in a tape spring will bifurcate and is verified against simulation results. Additionally, a numerical model of the wrapping an isotropic tape spring around a hub with a radius greater than the localized fold radii is validated against physical experiments. This model is used to predict trends in the force required to fully wrap a tape spring around a given hub radii.

Finally, when examining the coiling and uncoiling behavior of TRAC booms it was found that the tension force required to keep a TRAC boom tightly coiled is significantly less than the force required to initially coil the boom.

Published Content and Contributions

[1] Conte, D., Budzyn, D., Burgoyne, H., Di Carlo, M., Fries, D., Grulich, M., Heizmann, S., Jethani, H., Lapôtre, M., Roos, T., Serrano Castillo, E., Schermann, M., Vieceli, R., Wilson, L., Wynard, C. Innovative Mars Global International Exploration (IMaGInE) Mission-First Place Winning Paper. In *AIAA SPACE 2016* (2016), p. 5596. DOI: http://dx.doi.org/10.2514/6.2016-5596

L.W. researched and authored the in-situ resource utilization, space solar power and lander mass estimate sections of the paper.

[2] Leclerc, C., Wilson, L., and Pellegrino, S. Characterization of ultra-thin composite triangular rollable and collapsible booms. In *4th AIAA Spacecraft Structures Conference*, (2017), p. 0172. DOI: http://dx.doi.org/10.2514/6.2017-0172

L.W. performed experiments and numerical analysis on the coiling of ultra-thin composite booms and co-authored the paper.

[3] Ota, N., Wilson, L., Neto, A. G., Pellegrino, S., and Pimenta, P. Nonlinear dynamic analysis of creased shells. *Finite Elements in Analysis and Design 121* (2016), 64-74. DOI: https://doi.org/10.1016/j.finel.2016.07.008

L.W. performed numerical analysis on the snapping behavior of hemispherical polymer shells and co-authored the numerical examples section of the paper.

[4] Umali, J. A., Wilson, L., and Pellegrino, S. Vibration response of ultralight wrapped spacecraft structures. In *4th AIAA Spacecraft Structures Conference* (2017), p. 1115. DOI: http://dx.doi.org/10.2514/6.2017-1115

L.W. performed the higher fidelity numerical vibration model and wrote the corresponding sections of the paper.

[5] Wilson, L., Pellegrino, S., and Danner, R. Origami sunshield concepts for space telescopes. In *54th AIAA/ASME/ASCE/AHS/ASC Structures, Structural Dynamics, and Materials Conference* (2013), p. 1594. DOI: http://dx.doi.org/10.2514/6.2013-1594
L.W. performed mathematical and numerical analysis of the folding schemes, built lab-scale physical models, and the wrote paper.

Contents

List of Figures

List of Tables

Chapter 1

Introduction

1.1 Overview

1.1.1 Deployable Structures

Deployable structures are an integral component of many spacecraft. One common feature of these systems is an ability to be tightly packaged during launch, and then deployed into a much larger configuration once in space. Deployable structures are implemented in applications as diverse as antennae, solar sails, solar panels, booms, and inflatable habitats. Of key importance is the packaging efficiency, stiffness in deployed configuration, and predictability of the deployment process. The predictability of deployment is often the most difficult to capture without flight testing.

1.1.2 Testing of Deployable Structures

On the ground, gravity adds an extra variable to the testing of deployable structures that is not present in space. Gravity offload systems are the traditional solution, but more applicable to sufficiently stiff structures whose deployment is motorized. In offload systems, components are suspended by cables from low friction rollers that travel along rails above the deployable structure. However, even for scenarios such as these, this technique is not perfect. Friction between the rollers and rails can reduce deployment speed, while pendulum motion can occur due to the presence of the cables themselves. This approach becomes even more challenging for ultralight structures, such as thin carbon-fiber booms and planar arrays made from Kapton (polyimide) or Mylar that are on the order of tens of microns thick. Although the mass is lower, so too is the stiffness. This can cause booms and thin-films to sag, which can then change the deployment dynamics significantly.

Midway between testing on the ground and testing in space lie drop towers and zero-gravity flights. With drop towers the device to be tested is released from the top of a tower, and experiences weightlessness as it falls [39]. The effects of atmospheric drag can be reduced by pumping the air out, although there is always residual air resistance [22]. This approach is acceptable for small devices whose deployment time is on the order of seconds, that are either rugged enough to survive the fall or inexpensive enough to replace after each test.

For larger systems, on the order of meters, or those with longer deployment times, reduced-gravity flights are an option. Here an airplane flies in a series of parabolic arcs that allows the interior to experience weightlessness for durations of approximately 30 seconds. However, air-resistance is still present which can be problematic for deploying thin-film structures, such as solar sails.

In addition to these drawbacks, ground testing can be very expensive. An alternative to pure testing is to build either a numerical or analytical model of the deployment structure and use testing to validate this model. Once the model is validated, gravity and air-resistance can be removed from the model and the in-space performance estimated.

1.1.3 Analytical and Numerical Models of Deployable Structures

Many deployable structures utilize membrane or thin-shell components. There are two broad classes of approaches to modeling the behavior of these components. The first is a purely analytical approach. This can include capturing the bending energy within a coiled boom [8], or the stiffness in a series of folds in a packaged membrane [21].

However, these analytical approaches run into trouble when contact is a significant factor. Since the entire purpose of a deployable structure is to be packaged into a small volume, the effect of contact quickly becomes vitally important to include in the modeling approaches.

The final approach is to use numerical analysis, and in particular finite element analysis, or FEA. Here the system is divided into a large number of elements with nodes at each of the vertices. FEA can further be broken down into the numerical solver used, either implicit or explicit. Implicit solvers are best for quasi-static analysis without significant contact. Although commercial solvers are making progress in implementing robust contact algorithms in implicit solvers, explicit solvers are still better able to capture the behavior of systems with multiple contact conditions. A good

example is a creased thin-film sheet for a solar sail which has multiple overlapping layers when packaged. For these reasons, this work focuses on using explicit finite element analysis to capture both the static and dynamic behavior of ultralight deployable structures.

1.2 Objective and Scope

This work focuses on the deployment of creased thin-film structures, as well as strain-energy deployed tape springs and Triangular, Rollable and Coilable (TRAC) booms.

The deployment of creased thin-film structures differs significantly from traditional deployment mechanisms such as pantographs. Firstly, sheets with thicknesses on the order of tens of microns are extremely flexible and yet sufficiently stiff that it is important to consider the effect of bending stiffness in a numerical model. Secondly, the creases that are introduced can have a significant effect on both the deployment force and dynamic deployment behavior. One objective of this work is to determine if accurate quantitative and qualitative deployment forces can be obtained if the crease stiffness is removed entirely. Following this is the objective to develop a method for folding from flat and then deploying creased thin films structures in finite element software.

The second area of research focused upon in this body of work is strain-energy deployed booms. These booms have the advantage over traditional telescoping or pantograph booms in that they do not need motors to deploy. This reduces the number of failure points in the design as well as the overall complexity. However, to date neither tape springs nor TRAC booms, a derivative of tape springs, have been used in large space structures. This means they have not been packaged or deployed from being coiled to radii significantly greater than their local bend radius. Rather than fully conform to the large radius, these booms attempt to form many localized bends on the order of the natural bend radius of the boom. The final objective of this work is to simulate the effect these localized folds have on coiling behavior and wrapping forces. This includes developing FEA models that capture the localized fold behavior in tape springs and TRAC booms, including how the folds travel along the boom, how they bifurcate, and the corresponding force profiles. Trends in the forces required for wrapping tape springs to hub diameters greater and smaller than natural bend radius are also investigated.

1.3 Layout of Dissertation

This dissertation consists of seven chapters, including this first introductory chapter.

Chapter 2 is a literature review of both creased thin-film deployable structures and strain energy deployed booms. The modeling techniques used to capture these structures' behavior is then reviewed in detail.

Chapter 3 utilizes Abaqus/Explicit and LS-Dyna to capture the deployment behavior of wrapped polyimide sheets. These sheets are folded according to the GP92 fold pattern developed by Pellegrino & Guest [45] and are potentially useful in solar-sail packaging schemes.

Chapter 4 compares experiments, analytical, and simulation models of tape springs to validate the simulation approach for strain-energy deployed booms. These simulations capture the dynamic behavior of unfolding a single tape spring hinge and the dynamic uncoiling of a tape spring from around a fixed spool.

Chapter 5 extends the body work on tape springs to the force profile required to coil them around hubs of radii greater than and less than their natural bend radius.

Chapter 6 presents the results of extending the simulations to TRAC booms manufactured from ultra-thin carbon fiber composite.

Chapter 7 concludes the dissertation and provides recommendations for future work.

Chapter 2

Background

This thesis is primarily concerned with applying explicit finite element solvers to better understand and predict the deployment of ultralight deployable structures. In particular, the focus is on (a) creased thin-film sheets used for large planar spacecraft, such as solar sails and drag sails, and (b) strain-energy deployed booms such as tape springs and TRAC booms.

This chapter is split into three sections. The first section provides a general overview of the importance to space applications of these two classes of deployable structures. The second section focuses on modeling techniques currently used to analyze the behavior of large planar thin-film structures. The final section details the methods used to characterize and predict the behavior of strain-energy deployed booms.

2.1 Spacecraft Deployable Structures

Deployable structures are commonly used on spacecraft for their ability to be tightly packaged into a rocket payload fairing for launch and then deployed into a larger configuration once in orbit. These structures can range from wideband UHF helical antennae [38] to inflatable habitats under development by Bigelow Aerospace [29].

2.1.1 Large Planar Thin-Film Structures

Ever since Japan Aerospace Exploration Agency's (JAXA) IKAROS mission, solar sails have come under renewed scrutiny as a means of moving spacecraft around the solar system [43]. Solar sails are effectively very large sheets of a thin material such as Kapton or Mylar, stiffened by three or more booms. As light reflects off these sails, it imparts momentum which accelerates the whole

spacecraft. Since the force imparted by light is exceptionally small, solar sails need to be very large and lightweight. Other smaller solar sail missions include LightSail-1 by the Planetary Society [6] and NASA's NanoSail-D [17].

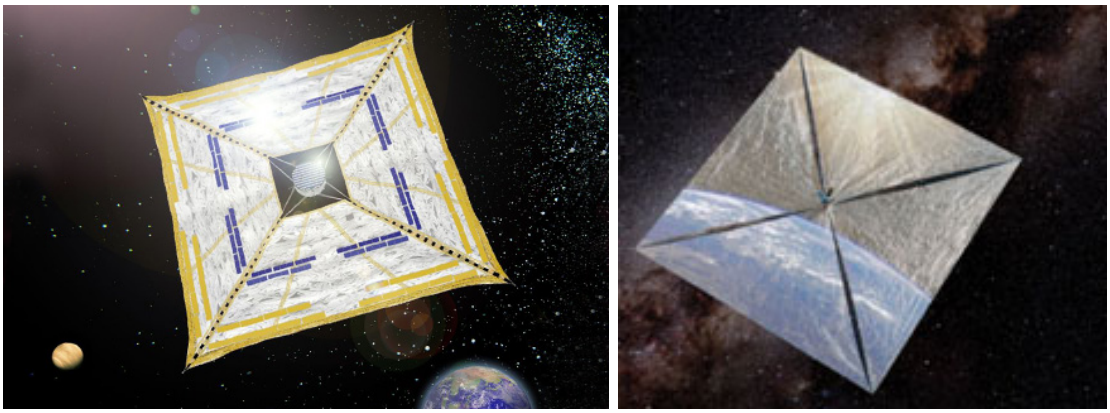

(a) (b)

Figure 2.1: Artist impressions of deployed solar sails for (a) IKAROS [43], and (b) LightSail-1 [6].

A similar system is a drag sail such as the University of Surrey's CubeSail [19, 48]. With the proliferation of cubesats (a class of satellites with side lengths ranging from 0.1 m to 0.3 m), orbital debris mitigation is a key concern. The UN Space Debris Mitigation Guidelines state satellites must de-orbit within 25 years of their design lifetime [15] or be moved to a graveyard orbit above 2000 km. This places an upper altitude limit of 600 km on cubesat orbits because with their small form factor, atmospheric drag is insufficiently strong to de-orbit cubsats above this altitude. When equipped with a drag sail the projected area of the satellite is increased substantially, increasing atmospheric drag and leading to a much faster de-orbit.

To be effective these types of systems need to be stiffened. LightSail-1, NanoSail-D, and most other solar sail designs call for four equispaced booms to force a square sail into planarity. Since these booms also need to be packaged into a tight configuration all of these booms are also ultralight deployable space structures in their own right.

2.1.2 Strain Energy Deployed Booms

There are a large number of classes of deployable booms, including telescoping booms like those used on the James Webb Space Telescope [2] and cylindrical booms that can be inflated with internal pressure and become rigid once in space, for instance via a reaction with UV light [11, 44].

These booms are relatively complex, heavy, and often require motors for deployment. This increases the number of potential failure points in the spacecraft design and operations if these motors fail. One solution is strain-energy deployed booms such as thin-walled composite tubes with tape-spring hinges [24]. In this case a dog-bone shape is cut out from the cylindrical tube to form tape spring hinges, the folded and deployed configurations are shown in Figure 2.2 below.

When these booms are packaged, elastic strain energy is introduced through bending. A hold-down and release mechanism is added to the system to keep the boom packaged during launch. Once in orbit, the boom is released and allowed to deploy, either with or without a control system. With fewer ancillary mechanisms required, the booms require less space than more complex solutions.

(a) (b)

Figure 2.2: Cylindrical carbon fiber boom incorporating dog-bone cutout hinges in (a) deployed configuration, and (b) folded configuration.

2.1.3 Coilable Deployable Booms

A subclass of strain-energy deployed booms are coilable, deployable booms. These booms are distinct from other stored energy booms because they can be flattened and tightly wrapped around a centralized hub. This allows for a very efficient packaging scheme ideal for space based applications. Sails in particular benefit from this approach as they need to be packaged bi-axially. Four main classes of these booms are tape springs, Storable Tubular Extendible Member (STEM) booms, Collapsible Tubular Masts (CTM), and Tubular Rollable and Coilable (TRAC) booms.

Tape springs, also known as carpenter's tapes, are the most simple of the coilable booms and because of this are often used in cubesat missions. Both metal [19] and carbon reinforced polymers [32, 16] have been used to fabricate these booms. One such deployment mechanism is shown

in Figure 2.4. Tape springs do, however, have low torsional stiffness and in most cases, do not have equal stiffness in both bending directions.

Figure 2.3: Tape spring [51]

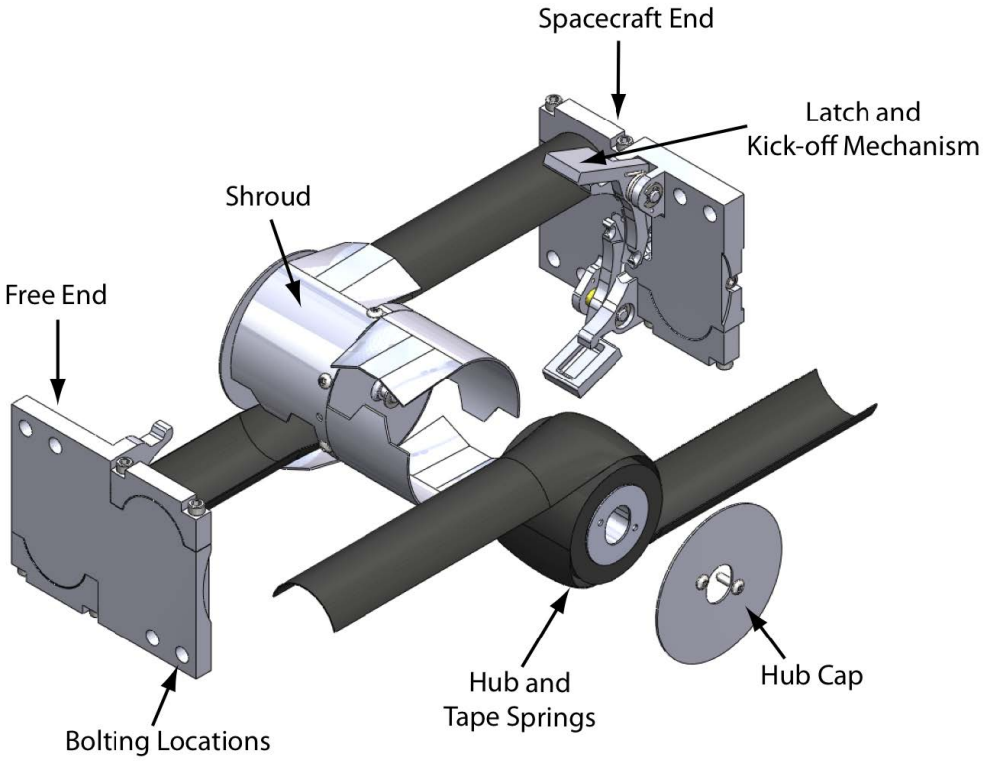

Figure 2.4: Exploded hub view of a CubeSat boom in initial stage of deployment [16].

A slight modification of a tape spring is the Storable Tubular Extendible Member (STEM) architecture, developed in Canada in the 1960s [24, 42] shown in Figure 2.5. Like a tape spring, it consists of a thin-walled cylindrical shell that can be flattened and rolled on a hub. The main difference is the arc-length of the cylindrical cross-section exceeds 2π radians. The increased arc-length results in higher axial and bending stiffness but the torsional stiffness is still low due to the

open cross section. Additional modifications are the bi-STEM concept as per Figure 2.5(b), where two STEM booms are overlapped during deployment. An interlocking STEM boom is displayed in Figure 2.5(c) and has a higher torsional stiffness than a standard bi-STEM boom.

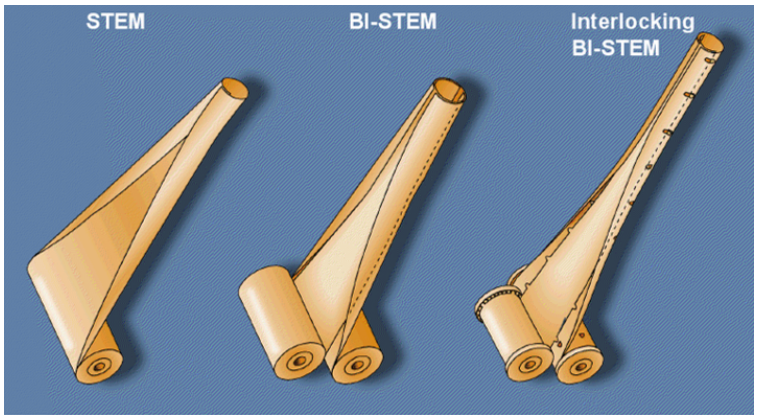

Figure 2.5: Storable Tubular Extendible Member booms [42] (a) Pure STEM (b) bi-STEM (c) Interlocking bi-STEM.

Collapsible Tubular Masts (CTMs) on the other hand have a closed cross-section and are formed by bonding two Ω shaped thin-shells together along the shared edge regions [24]. Figure 2.6 shows such a boom developed by DLR and made from composite material. It was found that for the DLR boom excessive strain energy in the coiled state led to unstable deployment dynamics and thus required an active deployment control mechanism [7].

Figure 2.6: Example of a carbon fiber Collapsible Tubular Masts developed by DLR [7].

The final type of coilable, strain energy deployed boom considered here is the Triangular Rollable

and Collapsible (TRAC) boom [33]. Originally developed at the Air Force Research Laboratory, it consists of two tape springs joined together along one edge. Figure 2.7 shows a schematic of a TRAC boom in both the coiled and deployed configurations. The open cross-section allows TRAC booms to be flattened and coiled more easily than CTMs [4]. An advantage over tape-springs is the comparitive simplicity in selecting design parameters to achieve equivalent bending stiffness in the X and Y directions [34]. These advantages led to TRAC booms being used in several cubesat missions [6, 52], where their low mass, high packaging efficiency, and ability to self-deploy were an asset.

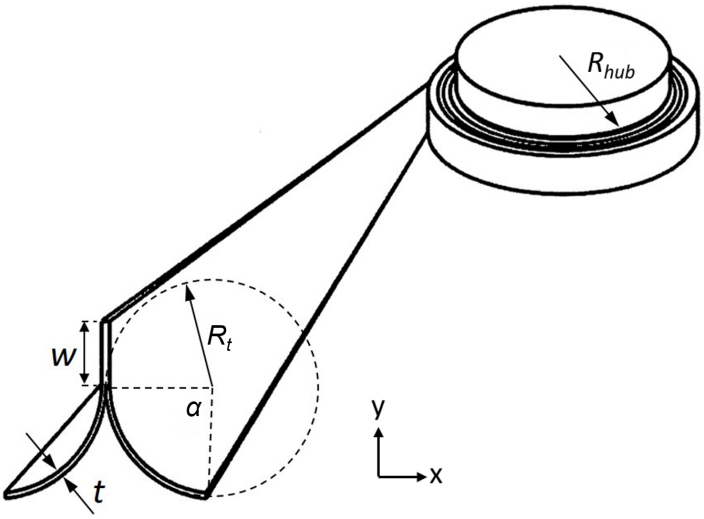

Figure 2.7: Schematic of a TRAC Boom [4].

2.2 Finite Element Modeling Approaches

Due to their low thickness when compared to overall size, ultralight deployable structures such as solar sails and coilable booms can be modeled with thin-shell elements in finite element analysis (FEA). Shells are useful for modeling thin components, since more than one element through the thickness is not required and thickness does not factor into the time step calculation for explicit solvers. The number of integration points through the thickness can be specified for shell elements. For nonlinear materials, a minimum of three through thickness integration points is recommended so that a nonlinear stress distribution can be calculated. Two integration points through the thickness are generally sufficient for elastic materials [23].

In general, reduced integration quadrilateral shell elements are preferred due to their low computational cost as well as the fact they do not experience shear or membrane locking. However, with the exception of triangular shells, any underintegrated shell formulation undergoes nonphysical modes of deformation called hourglass modes. These modes can be inhibited by tailoring internal 'hourglass forces' to counteract these deformations, among other methods [5].

Neither fully integrated quadrilateral, or triangular shell elements experience hourglass modes, however, they can be overly stiff under particular loading conditions [23]. In certain circumstances shear locking occurs, which is when transverse shear strain appears even if the material is under pure bending. Membrane locking on the other hand occurs if, due to the mesh, a finite element cannot bend without stretching. Shells have low bending stiffness when compared to their membrane stiffness. If the bending energy is incorrectly shifted into membrane energy, then the resulting displacements and strains will be under predicted. Controlling membrane locking is particularly important for simulating buckling [5].

Commercial FEA packages include Abaqus/Explicit and LS-Dyna. Abaqus/Explicit contains S4 fully integrated quadrilaterals, S4R reduced integration quadrilaterals, and S3 triangular thin-shell elements [1]. LS-Dyna offers are wide array of shell element formulations that can be specified in the simulations. The standard LS-Dyna shell elements are the reduced integration Belytschko-Tsay quadrilateral and C^0 triangular elements. The Belytschko-Tsay shell includes co-rotational coordinates that allow elements to twist/warp up to 1%. Belytschko-Wong-Chiang (BWC) elements are modified Belytschko-Tsay elements that can include additional warping. The C^0 triangular shell element is based on Mindlin-Reissner plate theory. LS-Dyna also offers a fully integrated quadrilateral shell element formulations, named Type 16, with assumed strain interpolants to alleviate locking and enhance in-plane bending behavior [13].

2.2.1 Implicit vs Explicit Finite Element Analysis

FEA can further be broken down into the numerical solver used, either implicit or explicit. In general implicit solvers are preferred because solution accuracy can be controlled through the selection of a suitable tolerance, while relatively large time steps are allowed. Explicit solvers control stability and accuracy through the use of time steps governed by the element level stress wave speed which can increase simulation time significantly. However, implicit solvers can be

inefficient for problems involving high velocity impact or high frequency vibration, and for problems with poorly conditioned contact stiffness [41], such as when multiple thin-film layers are packaged against each other. Explicit solvers are generally necessary in those cases.

Benchmark problems have been compared to determine the relative effectiveness of Sierra Solid Mechanics code, both implicit and explicit, and LS-Dyna explicit code [30, 41]. One study by researchers at JPL investigated four benchmark problems, including the dynamics of three masses connected with highly flexible straps, and fabric contacting flexible straps. They compared the multi-body code MSC/ADAMS, the explicit solver in LS-Dyna, and the implicit and explicit solvers within Sierra Solid Mechanics finite element codes. The most significant result was all three codes could handle the presence of contact between flexible bodies, but required varying degrees of simulation tuning to be convergent. For example, the Sierra implicit parallel solver was found to function up to two orders of magnitude faster than the corresponding explicit solver for a given number of processors. However, this advantage was found to degrade in the presence of high speed contacts and for soft contact.

2.3 Modeling Approaches for Large Thin-Film Planar Structures

Packaging large planar structures such as solar sails for launch requires creases to be introduced into the thin-film. Creases are narrow regions of high curvature where the film has deformed plastically. These creases not only reduce the level of flatness that can be achieved in the fully deployed structure, but also affect the deployment force required. Deployment is a complex process. It may appear to be random in nature, but successful automated deployment requires quantitative estimates and/or measurements of the maximum deployment force to be developed. It has been found, both during ground testing and in-orbit deployment, that the required deployment forces are difficult to predict, and the difficulty of reliably predicting the maximum force level has led to unexpected complications and failures [28, 35].

Characterizing the deployment behavior numerically or analytically requires determining the material properties of the sheet, the bending properties of the creases and friction response when the sheet comes into contact with itself. In general, the material and friction properties can be determined with standard ground tests. Crease responses are more challenging to capture, although substantial work has been done to analytically and numerically characterize the behavior of a single

crease [14, 20, 54].

Moving beyond a relatively simple crease model requires understanding the behavior of sheets with multiple creases where additional factors are important. In particular, when a wrapped film unfolds, it is governed by the interaction between the creases and the surrounding uncreased regions, as well as the sliding self-contact between different parts of the film.

For simulating sheets with multiple creases, one option is to represent creases with a moment vs angle relationship, as was done for simulations of the IKAROS solar sail mission. The sail was modeled as a membrane (endowed with finite extensional stiffness but zero bending stiffness) consisting of a large number of point masses connected by springs [37, 36, 46]. Crease bending moments were implemented by applying forces to the point masses either side of the creases.

This method does not account for the bending stiffness of the film, a key effect in capturing the actual shape, localized buckling, and wrinkling. To include this, a different model can be employed using thin shell elements and commercial FEA software [40] such as Abaqus or LS-Dyna.

In these packages typically creases are modeled as a kink in the meshed surface. This approach has been utilized to model the interaction between creases with wrinkles [53]. The crease stiffness, or the bending moment as a function of crease angle, depends on the initial kink angle. This approach has two key disadvantages. Firstly, the crease material stiffness is the same as that of the base film. Secondly, and more importantly, for structures that include many creases it is often impossible to ensure all creases have the correct initial crease angle, which will substantially change the crease stiffness.

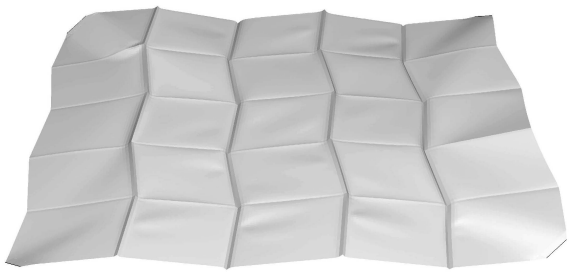

Figure 2.8: Abaqus simulation of a systematically creased sheet with a Miura-Ori crease pattern [40].

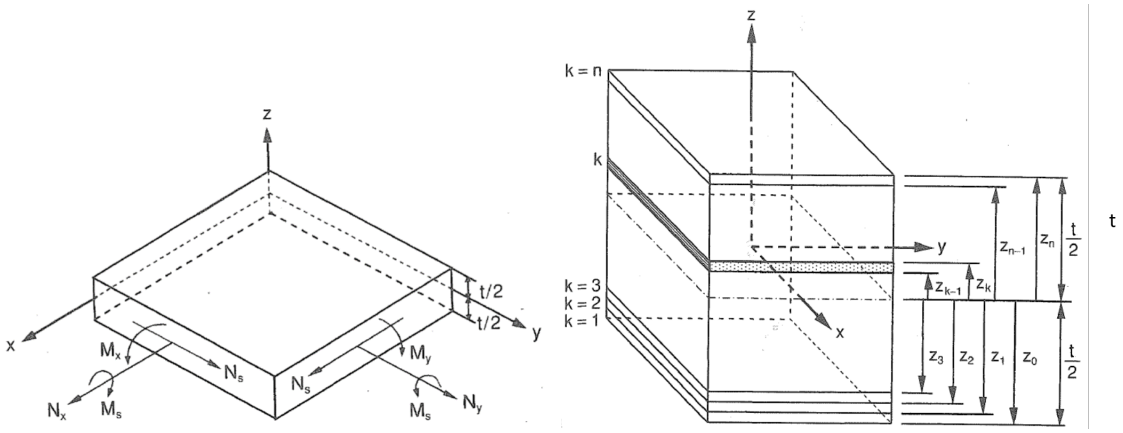

Figure 2.9: (a) Infinitesimal element of a thin-shell laminate with force and moment resultants, and (b) Infinitesimal element of a thin-shell laminate including coordinate notation for individual plies [9].

2.4 Modeling Thin-Shell Deployable Booms

There has been a significant amount of research characterizing the behavior of strain energy deployed booms, and in particular tape springs. The first subsection provides a brief overview in classical lamination theory. The following three subsections focus on the analytical characterization of the behavior and deployment of tape springs and draw heavily on work performed by Seffen & Pellegrino [45]. The final two subsections cover numerical approaches used to model tape springs and TRAC booms.

2.4.1 Classical Lamination Theory

The mechanical properties of thin-shell booms can be described with classical lamination theory [9], and in particular with the ABD matrix which relates shell force and moment resultants to the applied strains and curvature. Figure 2.9(a) shows an infinitesimal elements of a multi-ply laminate with a thickness t with force and moment resultants applied. Figure 2.9(b) shows the individual ply layups within the laminate, measured from a common reference plane. N_x, N_y are normal forces per unit length, and N_s is the shear forces per unit length. M_x, M_y are bending moments forces per unit length, and M_s is the twisting moment per unit length. The forces and moments can be found by integrating the in-plane and shear stress through the thickness of the laminate.

$$\begin{bmatrix} N_x \\ N_y \\ N_s \end{bmatrix} = \sum_{k=1}^{n} \int_{z_{k-1}}^{z_k} \begin{bmatrix} \sigma_x \\ \sigma_y \\ \tau_s \end{bmatrix}_k dz \tag{2.1}$$

and

$$\begin{bmatrix} M_x \\ M_y \\ M_s \end{bmatrix} = \sum_{k=1}^{n} \int_{z_{k-1}}^{z_k} \begin{bmatrix} \sigma_x \\ \sigma_y \\ \tau_s \end{bmatrix}_k z dz \tag{2.2}$$

The stresses in each ply can be found by first finding the stresses in the principle material direction of each ply in terms of the principle strains

$$\begin{bmatrix} \sigma_1 \\ \sigma_2 \\ \tau_6 \end{bmatrix}_k = \begin{bmatrix} Q_{11} & Q_{12} & 0 \\ Q_{21} & Q_{22} & 0 \\ 0 & 0 & Q_{66} \end{bmatrix}_k \begin{bmatrix} \epsilon_1 \\ \epsilon_2 \\ \gamma_6 \end{bmatrix}_k \tag{2.3}$$

where for an orthotropic material

$$Q_{11} = \frac{E_{11}^2}{E_{11} - \nu_{12} E_{22}},\ Q_{12} = \frac{\nu_{12} E_{11} E_{22}}{E_{11} - \nu_{12}^2 E_{22}},\ Q_{22} = \frac{E_{11} E_{22}}{E_{11} - \nu_{12}^2 E_{22}},\ Q_{66} = G_{12} \tag{2.4}$$

with E_{11} and E_{22} the Young's modulus values in the longitudinal and transverse material directions, ν_{12} the poisson ratio and G_{12} the shear modulus. Transforming the system into the laminate coordinates, rather than the material coordinates of each ply, gives

$$\begin{bmatrix} \sigma_x \\ \sigma_y \\ \tau_s \end{bmatrix}_k = \begin{bmatrix} Q_{xx} & Q_{xy} & Q_{xy} \\ Q_{xy} & Q_{yy} & Q_{sy} \\ Q_{sx} & Q_{sy} & Q_{ss} \end{bmatrix}_k \begin{bmatrix} \epsilon_x \\ \epsilon_y \\ \gamma_s \end{bmatrix}_k \tag{2.5}$$

or in brief,

$$\underline{\sigma_k} = Q_k \underline{\epsilon} \tag{2.6}$$

Finally, the strains at any point in the laminate can be written in terms of the strains at a

reference plane in the laminate and the curvature of the laminate

$$\begin{bmatrix} \epsilon_x \\ \epsilon_y \\ \gamma_s \end{bmatrix} = \begin{bmatrix} \epsilon_x^0 \\ \epsilon_y^0 \\ \gamma_s^0 \end{bmatrix} + z \begin{bmatrix} \kappa_x \\ \kappa_y \\ \kappa_s \end{bmatrix} \tag{2.7}$$

where κ_x, κ_y, and κ_s are the bending and twisting curvatures in the laminate, and ϵ_x^0, ϵ_y^0, and γ_s^0 are the in-plane and twisting strains at the laminate reference plane. Combining Equation 2.5 and Equation 2.7 gives

$$\underline{\sigma_k} = Q_k \underline{\epsilon^0} + z Q_k \underline{\kappa} \tag{2.8}$$

Equation 2.1 and Equation 2.2 then become

$$\begin{bmatrix} N_x \\ N_y \\ N_s \end{bmatrix} = \sum_{k=1}^{n} \left\{ \begin{bmatrix} Q_{xx} & Q_{xy} & Q_{xy} \\ Q_{xy} & Q_{yy} & Q_{sy} \\ Q_{sx} & Q_{sy} & Q_{ss} \end{bmatrix}_k \begin{bmatrix} \epsilon_x^0 \\ \epsilon_y^0 \\ \gamma_s^0 \end{bmatrix} \int_{z_{k-1}}^{z_k} dz + \begin{bmatrix} Q_{xx} & Q_{xy} & Q_{xy} \\ Q_{xy} & Q_{yy} & Q_{sy} \\ Q_{sx} & Q_{sy} & Q_{ss} \end{bmatrix}_k \begin{bmatrix} \kappa_x \\ \kappa_y \\ \kappa_s \end{bmatrix} \int_{z_{k-1}}^{z_k} z dz \right\} \tag{2.9}$$

and

$$\begin{bmatrix} M_x \\ M_y \\ M_s \end{bmatrix} = \sum_{k=1}^{n} \left\{ \begin{bmatrix} Q_{xx} & Q_{xy} & Q_{xy} \\ Q_{xy} & Q_{yy} & Q_{sy} \\ Q_{sx} & Q_{sy} & Q_{ss} \end{bmatrix}_k \begin{bmatrix} \epsilon_x^0 \\ \epsilon_y^0 \\ \gamma_s^0 \end{bmatrix} \int_{z_{k-1}}^{z_k} z dz + \begin{bmatrix} Q_{xx} & Q_{xy} & Q_{xy} \\ Q_{xy} & Q_{yy} & Q_{sy} \\ Q_{sx} & Q_{sy} & Q_{ss} \end{bmatrix}_k \begin{bmatrix} \kappa_x \\ \kappa_y \\ \kappa_s \end{bmatrix} \int_{z_{k-1}}^{z_k} z^2 dz \right\} \tag{2.10}$$

This can be simplified into the form

$$\begin{bmatrix} N \\ M \end{bmatrix} = \begin{bmatrix} A & B \\ B & D \end{bmatrix} \begin{bmatrix} \epsilon^0 \\ \kappa \end{bmatrix} \tag{2.11}$$

where A, B, and D are 3x3 matrices of the form

$$
\begin{aligned}
A_{ij} &= \sum_{k=1}^{n} Q_{ij}^{k} \left(z_k - z_{k-1}\right) \\
B_{ij} &= \frac{1}{2} \sum_{k=1}^{n} Q_{ij}^{k} \left(z_k^2 - z_{k-1}^2\right) \\
D_{ij} &= \frac{1}{3} \sum_{k=1}^{n} Q_{ij}^{k} \left(z_k^3 - z_{k-1}^3\right)
\end{aligned}
\tag{2.12}
$$

2.4.2 Characterizing Tape Spring Bending Moment

Seffen & Pellegino have shown that the behavior of a tape spring can be represented by a moment-angle relationship $M(\theta)$ as shown in Figure 2.10 [45]. The initial unloaded configuration is represented by O at the origin. In Figure 2.10 the positive bending moment corresponds to opposite sense bending, where the applied bending moment induces compression loading along the edges of the tape spring. The moment-angle relationship is linear between O and A, after which the tape spring buckles into two almost straight sections connected by a localized bend, as shown in Figure 2.11(a). From B to C the radius of the localized bend remains unchanged, but its arc length increases while the bending moment is constant. Upon unfolding, the tape spring follows the constant-moment path from C to D until it suddenly snaps to E.

When a negative moment is applied, however, the moment-angle relationship is linear until a sudden bifurcation occurs at F, corresponding to a flexural torsional deformation. For equal-sense bending the unloading path is almost identical to the loading path.

For an isotropic material, the strain energy areal-density μ in the localized fold region can be found from the standard expression for bending strain energy per unit area in a thin-shell. Since purely cylindrical bending is assumed the stretching strain energy is neglected.

$$
\mu = \frac{1}{2} D \left(\Delta\kappa_t^2 + 2\nu\Delta\kappa_t\Delta\kappa_l + \Delta\kappa_l^2\right) \tag{2.13}
$$

where $\Delta\kappa_l$ and $\Delta\kappa_t$ are the change in longitudinal and transverse curvature, respectively. ν is the Poisson ratio and D the flextural stiffness

$$
D = \frac{Et^3}{12(1-\nu^2)} \tag{2.14}
$$

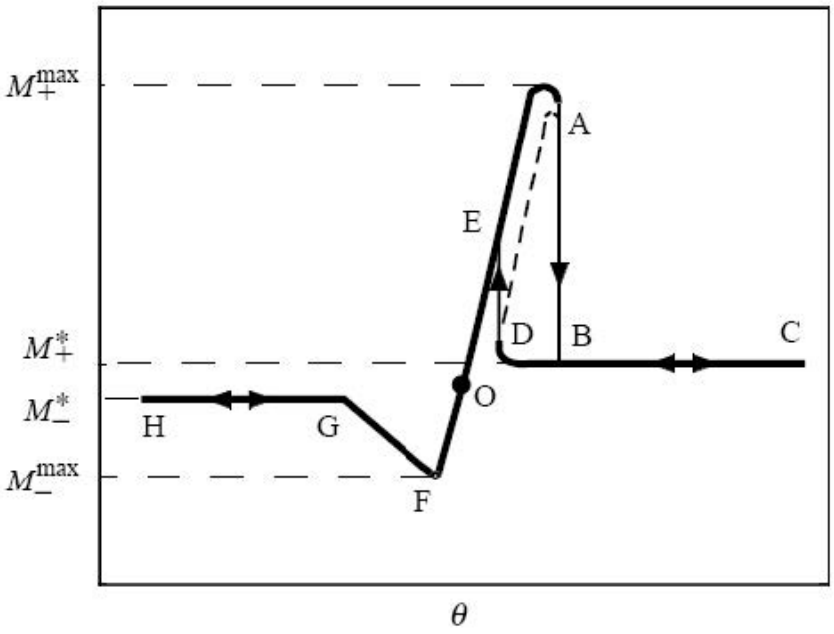

Figure 2.10: Moment-angle relationship for a general tape spring [45].

where E is the Young's modulus and t the thickness of the tape spring. As the transverse and longitudinal directions are principal directions of curvature, $\Delta\kappa_l = \pm\frac{1}{R_i}$, $\Delta\kappa_t = \frac{1}{R_t}$, where + corresponds to opposite-sense curvature, and - to equal-sense curvature. R_i is the natural bend radius of the localized fold region. Since the transition region between the localized fold and the straight undeformed tape spring is independent of R_i, the energy contained in the transition region can be neglected from the analysis to find R_i [8].

By minimizing the total energy in the fold region, it has been shown that the radius of the localized bend R_i depends on the initial transverse radii of the tape spring R_t, and the longitudinal and transverse bending stiffness D_{11} and D_{22}, respectively [8]. D_{11} and D_{22} are elements of the D matrix defined in Equation 2.12.

$$R_i = R_t\sqrt{\frac{D_{11}}{D_{22}}} \tag{2.15}$$

For an isotropic material, $D_{11} = D_{22}$ and thus $R_i = R_t$. Therefore, for an isotropic material, the energy areal density can be simplified to

$$\mu = \frac{D(1 \pm \nu)}{R_t^2} \tag{2.16}$$

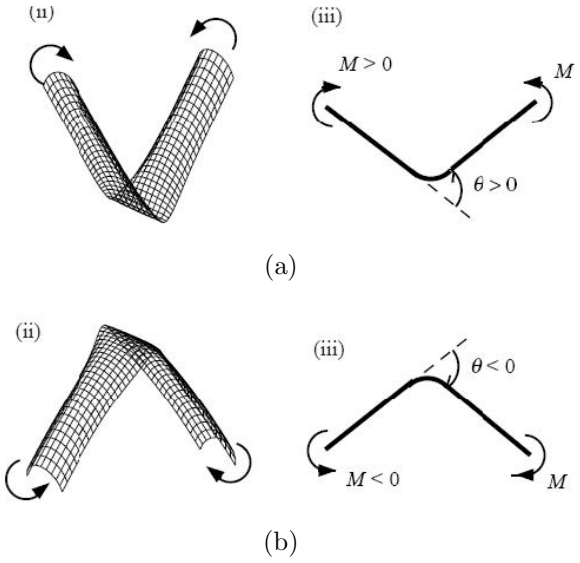

Figure 2.11: Tape spring bending in (a) opposite-sense, and (b) equal-sense [45].

The total energy in the localized fold U for an isotropic tape spring can be found by multiplying Equation 2.16 with the surface area of the localized fold.

$$U = \mu R_t^2 \alpha\theta = D(1 \pm \nu)\alpha\theta \tag{2.17}$$

where α is the arc-angle of the tape spring in the transverse direction, and θ is defined in Figure 2.11.

2.4.3 Unfolding of a Tape Spring with a Single Fold

In 1999 Seffen & Pellegrino [45] developed two analytical models of the unfolding of a tape spring with a single opposite sense fold. Figure 2.12 shows a schematic of this system including key parameters. λ is the ratio of deployed length to total length, and θ is the deployed angle. The difference between y and ξR is the transition region length. g indicates the direction of gravity.

When released from an initially folded configuration, the straight section λL rotates towards the vertical position, while the localized fold travels along the tape spring, until it reaches the clamped end. The localized fold then reflects off the clamped end and travels back up the tape spring. This effect is seen experimentally, as shown in Figure 2.13. Figure 2.13 contains a series of photos taken of a 0.54 m long tape spring with radius $R_t = 13.3$ mm, $\alpha = 150^o$ starting in an initially folded configuration with $\theta_0 = 90^o$. The images are taken at intervals of $\frac{1}{25}$ s running from top left to

bottom right. The tape was encased in epoxy at the base.

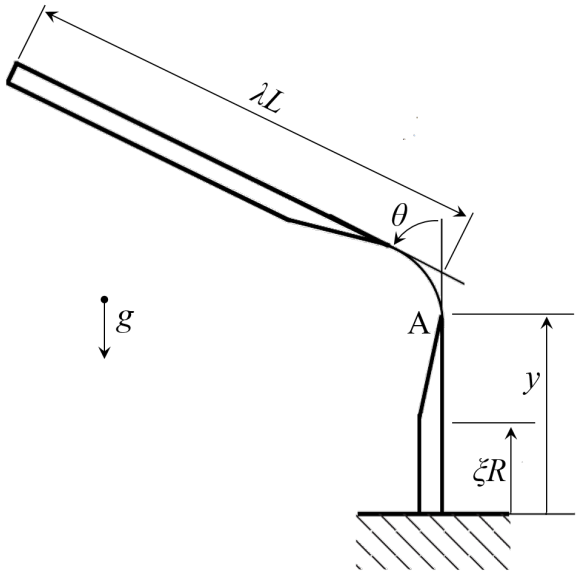

Figure 2.12: Schematic of a tape spring with a localized fold distance y away from a clamped end [45].

Of the two analytical models developed to capture this behavior, the first was based on an energy formulation that included the gravitational potential and kinetic energy in the tape spring, and the strain energy in the tape spring folds. As the tape spring unfolds, the localized fold travels along the tape spring until it reflects off a clamped end. However, the approach enforced conservation of energy and did not account for energy loss through the boundary. Without this loss, the tape spring would return to its initial configuration after each reflection of the localized fold from the clamped end.

To account for this energy loss, the second model was based on an impulse-momentum approach. This approach used a different formulation of the equations of motion which did not assume energy conservation. The impulse-momentum approach was compared against experimental data from three tests of tape springs clamped in three different orientations with respect to gravity. The results for the case corresponding to that in Figure 2.12 are plotted in Figure 2.14.

The model and experiments captured the first reflection of the localized fold at 0.1 s, after which the fold traveled up the tape spring until 0.19 s. The fold traveled back down to the clamped region at 0.25 s. After each reflection θ increased, but reached a lower peak value because of the energy loss associated with the fold reflecting off the clamped end. After 0.31 s the tape spring was

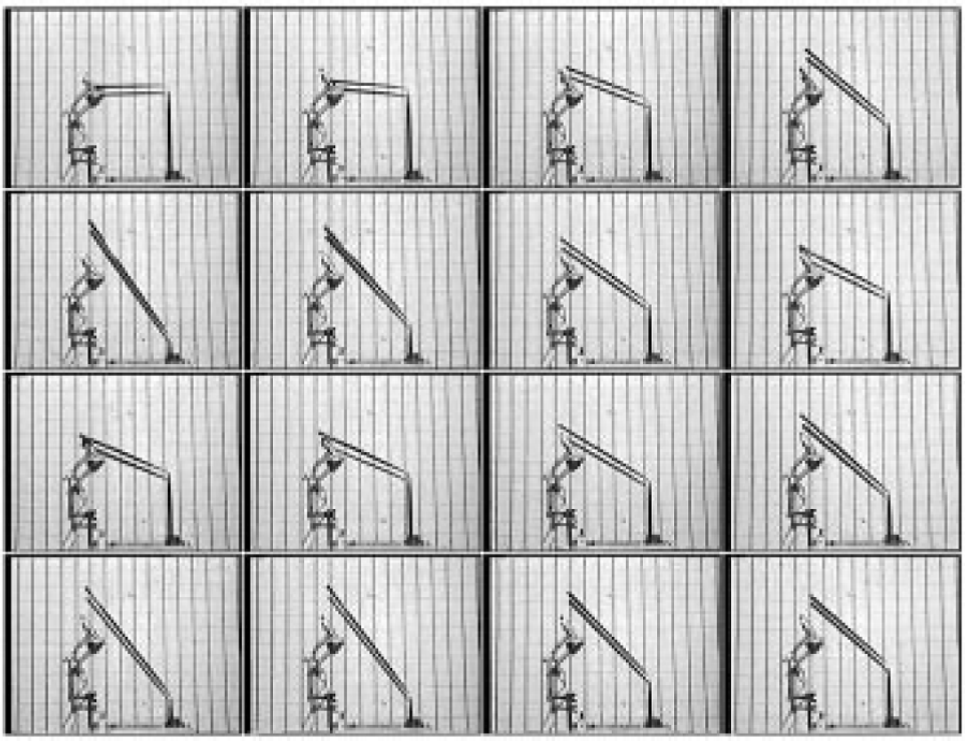

Figure 2.13: Deployment sequence of a 0.54 m long tape spring with a localized fold of 90^o in the middle. Time delay between successive frames is 0.04 s [45].

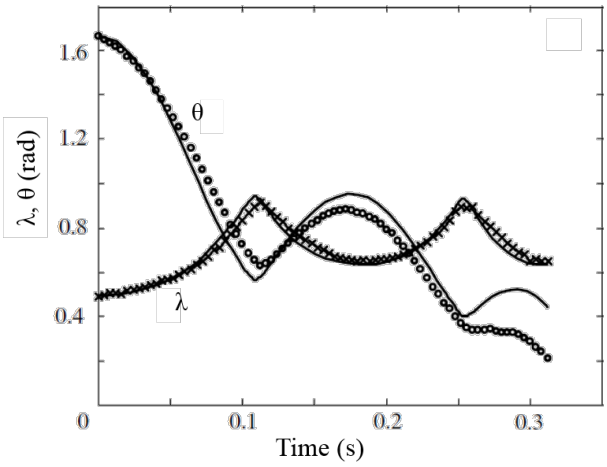

Figure 2.14: The solid lines are the predictions of θ and λ during deployment, based on an impulse-momentum formulation [45]. The circles and crosses correspond to experiment measurements of θ and λ, respectively.

almost fully deployed and straight.

2.4.4 Uncoiling Tape Spring Booms

In 1999 Seffen & Pellegrino also developed the theory for the two-dimensional deployment dynamics of isotropic tape springs coiled on a free-turning circular spool whose radius R_{hub} is approximately equal to the transverse radius of curvature R_t of the tape. The theory is applicable to the main part of the deployment process, during which the tape spring uncoils. They focused on the case where $R_{hub} \approx R_t$ because this is the radius the tape will attempt to form when coiled. For the case where $R_{hub} \leq R_t$ the radius expands as soon as deployment starts and for $R_{hub} \geq R_t$ the tape forms a series of localized folds of radius R_t connected by straight regions. These types of behavior were beyond the scope Seffen & Pellegrino studies.

Assuming that $R_{hub} \approx R_t$ and that the tape does not change radius, the tape was modelled in two parts as shown in Figure 2.15. The first part is a straight deployed section of tape spring of length λL, where L is the total length of tape spring. The second is a section of tape spring coiled around a spool of radius R_{hub}. ξ corresponds to the angle of rotation of the entire spool and γ to the total angle of the remaining coiled tape spring.

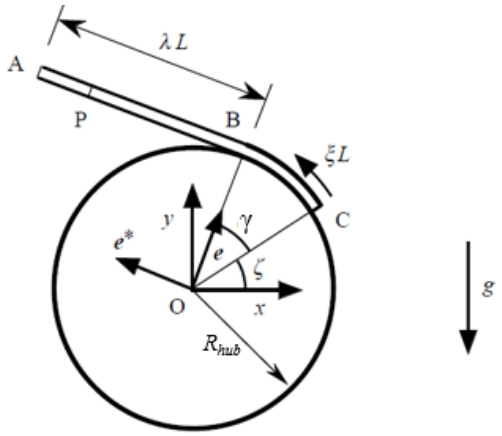

Figure 2.15: Schematic diagram of a tape spring coiled around a fixed spool [45].

With these assumptions Seffen & Pellegrino derived equations for the motion of a coiled tape spring by the application of Lagranges equations

$$\frac{d}{dt}\left(\frac{\partial \mathcal{L}}{\partial \dot{q}_i}\right) - \frac{\partial \mathcal{L}}{\partial q_i} = Q_i \tag{2.18}$$

where q_i are the generalized coordinates of the system, in this case γ and ξ. Q_i are the generalized

forces corresponding to any non-conservative forces acting on the system and $\mathcal{L}$ is the Lagrangian of the system, specifically the difference between the total kinetic and potential energies. By neglecting the transition region and gravity, and assuming a fixed spool, i.e., $\xi = 0$, $\dot{\xi} = 0$, and $\ddot{\xi} = 0$, Seffen & Pellegrino derived the following equation

$$\frac{1}{3}\rho(L - R_{hub}\gamma)^3\ddot{\gamma} - \frac{1}{2}\rho(L - R_{hub}\gamma)^2\dot{\gamma}^2 + \mu R_{hub}R_t\alpha = 0 \tag{2.19}$$

The first and last terms are derived from the potential energy of the coiled tape spring, and the second term from the tape kinetic energy as it deploys. It was shown that

$$\dot{\gamma}^2 = \frac{6\mu R_{hub}R_t\alpha}{\rho}\frac{\gamma_0 - \gamma}{(L - r\gamma)^3} \tag{2.20}$$

Setting the deployed length of the tape spring as λL, γ and $\dot{\gamma}$ become

$$\begin{aligned} \gamma &= (1 - \lambda)\frac{L}{R_{hub}} \\ \dot{\gamma} &= -\frac{\lambda\dot{L}}{R_{hub}} \end{aligned} \tag{2.21}$$

Finally, by assuming that at $t = 0$ the tape is in the fully coiled configuration with $\lambda = 0$ and integrating with respect to time, the ratio of deployed length to total length was derived as

$$\lambda = \sqrt[4]{\frac{6\mu R_t R_{hub}^2\alpha}{\rho L^4}}\sqrt{2t} \tag{2.22}$$

Seffen & Pellegrino validated their equation experimentally and obtained the result in Figure 2.16. Figure 2.16 shows Seffen & Pellegrino's results assuming no air drag, and including a drag parameter that was tuned such that the model matches the analytical prediction. Gravity was also included in the second model but was found to have only a small effect on the results.

2.4.5 Numerical Models for Tape Springs

While analytical approaches to predicting tape spring behavior have focused on isotropic tape springs, significant numerical work has been performed on both composite tape springs and tape springs coupled to additional parts.

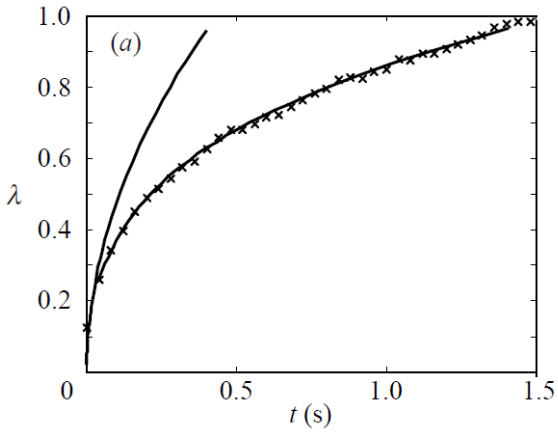

Figure 2.16: Deployment plot of a coiled tape spring under opposite sense bending on a fixed spool. Crosses are experimental results; solid lines are analytical predictions. Top solid line is the deployment assuming no air drag, lower solid line includes air drag with a tuned drag coefficient [45].

In particular, tape spring hinges have been the focus of many numerical studies. The composite booms detailed in Section 2.1.2 have been modeled in Abaqus/Explicit with S4 fully integration quadrilateral shell elements, or S4R reduced integration quadrilateral shell elements [26, 27, 55]. The main advantage of using explicit solvers for the folding and deployment simulations is that these solvers deal efficiently with changing contact conditions and are insensitive to ill conditioning of the stiffness matrix. These features are particularly useful in the analysis of ultra-thin shell structures that are folded and allowed to dynamically deploy.

A standard approach is to start with the thin-shell structures in an unstressed configuration, and then use either boundary conditions or contact with another part to flatten the tape spring. Once flattened, the tape spring can be folded by applying boundary conditions to the ends. An example of folding a composite boom containing a tape spring hinge is shown in Figure 2.17.

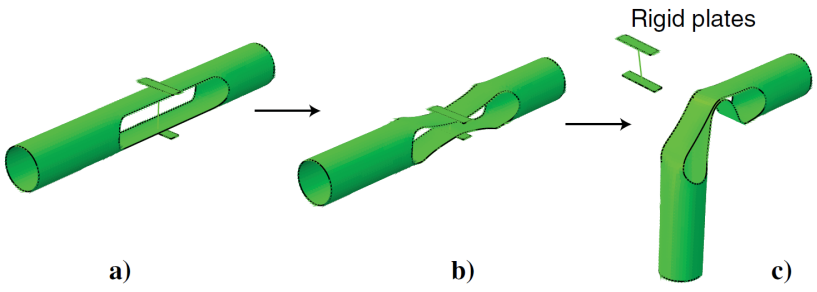

Figure 2.17: Folding stages of a composite tape spring hinge in Abaqus/Explicit [26] (a) Initial configuration, (b) Rigid plates compress tape springs, (c) Boundary conditions fold hinge.

Explicit code can be used for quasi-static problems involving significant contact as well. However, techniques such as varying loading rates, or applying numerical damping such as bulk viscosity or viscous damping, are required to remove excess kinetic energy. Mass scaling is an alternative technique where the density of a part is increased. The specific effect of each of these parameters has been studied in depth [25].

Additional FEA studies have determined the bending stiffness of deployed booms and the buckling load [10, 50]. Abaqus/Explicit has even been used to simulate the coiling of a carbon fiber tape spring around a hub [47], where $R_{hub} \simeq R_i$. Figure 2.18 depicts the fully coiled configuration.

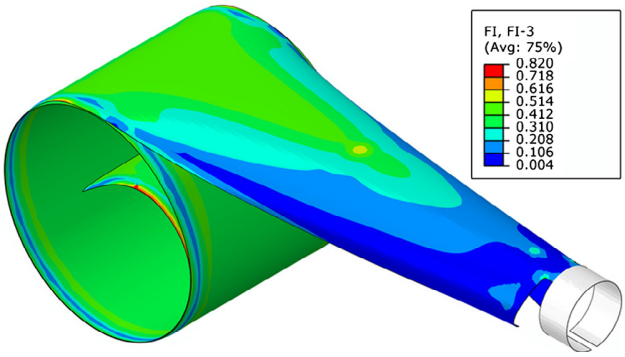

Figure 2.18: Coiled composite tape spring in Abaqus/Explicit [47]. Contours correspond a failure index.

2.4.6 TRAC Boom Characterization

As explained in Section 2.1.3, Tubular Rollable and Coilable (TRAC) booms are derived from tape springs, but designed to allow for increased bending and torsional stiffness [33, 34]. They consist of two tape springs of radius R_t and arc length $R_t\alpha$ joined along a single, common edge with a bond region of height w, as shown in Figure 2.19. This architecture allows the boom to be flattened and coiled around a central hub of radius R_{hub}, similar to a tape spring. The upper section has a natural bending radius that corresponds to that of a tape-spring with equal radius and material properties. The addition of the flat bond region increases the natural bend radius.

Previous characterizations of the mechanical properties of deployed TRAC booms have focused on booms made from carbon fiber composite with flange thickness of $\sim$1 mm [4]. Such characterizations have included bending stiffness and estimation of the buckling load, both through experiments as well as Abaqus simulations. One such buckling mode is shown in Figure 2.20. Their

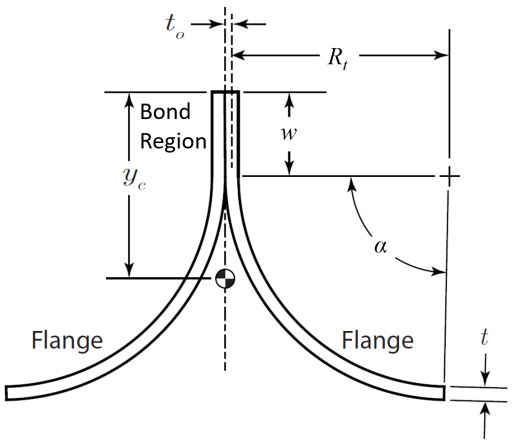

Figure 2.19: TRAC boom cross-section including variable names [34].

Figure 2.20: TRAC boom buckling mode [4].

vibration properties have also been characterized at the Air Force Institute of Technology [49].

One challenge with employing TRAC booms on spacecraft larger than small satellites is TRAC booms exhibit 'triangular buckles' when coiled to radii significantly larger than the natural bending radius of the boom [34]. If the bond region is constrained to larger radii, the inner flange will open as shown in Figures 2.21(a) and 2.21(b). These 'buckles' can cause stress concentrations in the boom which in turn can cause delamination between composite layers.

For spacecraft that require long TRAC booms, by necessity the maximum coiling radii will be greater than the natural coiling radii of the boom. Although current work has identified the existence of these 'buckles', little has been done to quantitatively understand them.

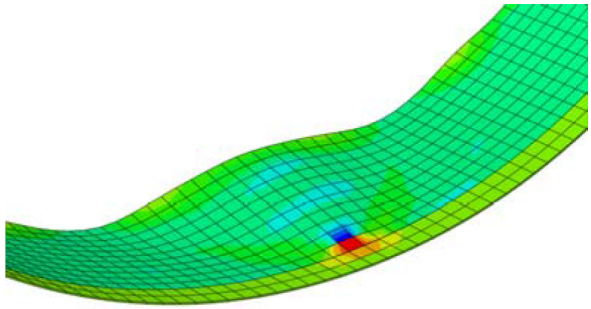

(a)

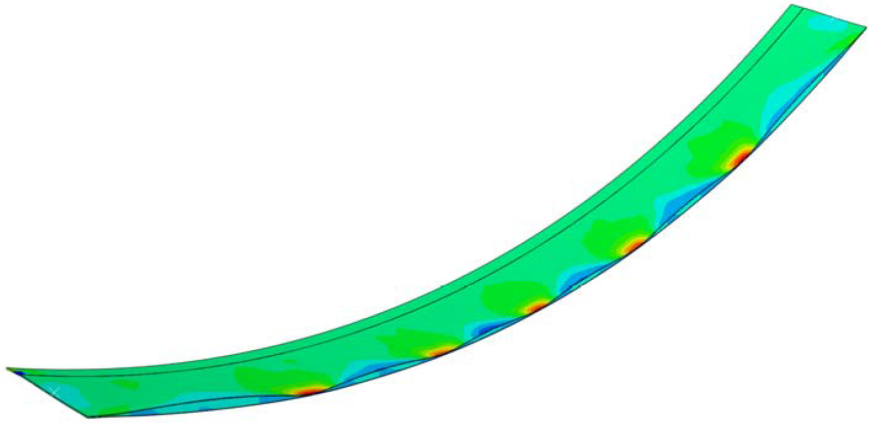

(b)

Figure 2.21: FEA image of 'triangular buckles' identified in TRAC booms when coiled to a radius greater than its natural bending radius [34] (a) close up of 'buckle', and (b) a series of 'buckles'.

Chapter 3

Packaging & Deployment of Creased Thin-Film Sheets

This chapter presents accurate FEA models of the packaged configuration of creased thin-film sheets. The effectiveness of excluding bending stiffness when modeling creases is investigated. Simulations of a benchmark crease pattern are used to develop a general technique for modeling the packaging and deployment of creased thin-film sheets, including avoiding excessive wrinkling, crumpling and ensuring creases remain straight. The knowledge gained from these simulations is used to formulate the Momentless Crease, Force Folded (MCFF) modeling technique for the folding of creased thin-film sheets with minimal defects in FEA software such as LS-Dyna.

3.1 Obtaining an Accurate Wrapped Configuration

As detailed in Section 2.1.1, creased thin-film sheets are useful for a large range of spacecraft applications, including solar sails, drag sails, and deployable antennas. One significant advantage of using thin-film sheets is their high packaging efficiency. However, to take advantage of this, the sheet needs to be folded into a tightly packaged configuration by forming a suitable set of creases in the sheet.

Creases are narrow regions of high curvature where the film has deformed plastically. These creases not only reduce the level of flatness that can be achieved in the fully deployed structure, but also affect the deployment force required. Due to the difficulties of testing these ultra-thin lightweight structures on the ground, as explained in Section 1.1.2, finite element analysis is an important tool to obtaining a qualitative and quantitative understanding of the deployment behavior

and forces.

To capture this behavior, custom models are traditionally developed [37, 36, 46]. These can be time consuming to implement and may neglect real physical behavior such as bending stiffness of the film. In addition, these analysis approaches start in an already packaged configuration that is generated analytically. This has the downside of being an approximation, as well as being unable to include any of the stresses within the sheet in the folded configuration. Finally, depending on the folding process, the exact folded configuration may not be initially known.

This leads to the need to find the wrapped or packaged configuration after starting with an undeformed sheet surface. For developable surfaces, this means starting with an initially flat, planar surface and then folding into the packaged configuration. This is a highly challenging problem because thin-films have very low bending stiffness and can easily be wrinkled or crumpled. In addition to being a problem in the physical world, in FEA simulations wrinkling can be on the order of the element length and generate mesh artifacts that lock into place, as covered in Section 3.4.

3.2 Implenting Creases in FEA Software

Abaqus/Explicit and LS-Dyna were selected as the FEA software to develop the technique for folding and deploying creased thin-film structures because of their robust algorithms for handling contact efficiently. Both sets of software are also widely used by the aerospace community [23].

In these FEA packages sheets can be meshed with either membrane, thin-shell or continuum shell elements. Membrane elements neglect the bending stiffness of the sheet and so are not used here. Continuum shell elements are better suited to sheets with thickness-to-length ratios much greater than those found in solar or drag sails. Thin-shell elements are therefore utilized for the following simulations. More details on elements available in these FEA packages can be found in Section 2.2.

3.2.1 Capturing Crease Behavior

In previous finite element work [40] creases have been introduced into a sheet as simple kinks in the surface meshed with thin-shell elements. There are two key drawbacks to this approach. Firstly, the crease stiffness k is constant and entirely dependent on the material properties of the base film.

(a) (b)

Figure 3.1: Schematics of a crease cross-section, meshed with thin-shell elements of length L. (a) Initial configuration and (b) configuration with bending moment M applied

Secondly, for structures that include many creases, it is difficult to set the initial kink crease angle θ_0 equal to the neutral crease angle θ_n for all creases. θ_n is the crease angle when zero external force or moment is applied. If $\theta_n \neq \theta_0$ then the opening and closing moments M are incorrect and may change the force required to deploy the structure. A schematics of crease cross-sections meshed with thin-shell elements is shown in Figure 3.1, and the relationship between angle and moment is

$$M = k(\theta)\,(\theta - \theta_n) \tag{3.1}$$

A modification of this strategy involves imposing a thermal gradient through the sheet thickness in the elements on either side of a crease. This approach still represents creases as kinks in the surface. However, the imposed thermal gradient will control θ_n. Even if additional creases constrain θ_0 in the folded configuration, θ_n will depend only on the thermal gradient and the bending stresses will reflect that. Never the less k will still depend upon the material properties of the sheet. Also, unless the coefficient of thermal expansion is orthortopic and set to zero along the crease direction, additional non-realistic stresses would be introduced due to expansion of the material in the crease direction.

The approach proposed in this chapter is to remove the crease bending stiffness entirely and set $k = 0$. While this approach neglects the bending moment contribution from the creases, it does not impose unrealistic crease moments that change with θ_0, θ or mesh density. This approach is implemented in the following sections for Abaqus/Explicit via connector elements and in LS-Dyna via tied constraints.

3.2.2 Generating Zero-Stiffness Creases in Abaqus/Explicit

To generate zero-stiffness creases in Abaqus, an effective way is to separate the material on either side of the crease into separate parts, and mesh the two parts so the nodes on either side of a crease have the same x,y,z coordinates. CONN3D connector elements then join the translational degrees of freedom of each set of nodes with the same x,y,z coordinates together, effectively creating a pin-joint. The row of pin-joints approximates a zero-stiffness crease with $k = 0$.

3.2.3 Generating Zero-Stiffness Creases in LS-Dyna

Similar to Abaqus, one way to create zero-stiffness creases in LS-Dyna is to split the sheet on either side of the crease into separate parts. Once meshed, one part is defined as the slave and the other the master. The nodes on the edge of the slave part have their translational degrees of freedom tied to the adjacent master facet elements, using the Contact_Tied_Nodes_to_Surface command.

One challenge to creating creases in LS-Dyna is that even if the master and slave nodes perfectly intersect, the solver may not identify the correct master surface to project the tied slave node onto, as shown in Figure 3.2(a). In practice it was found that in some cases a small overlap of the slave node on the master surface of up to 25 µm was needed for elements 2 mm wide, for the tied constraint to initialize on all slave nodes. In the benchmark problem simulations presented in Section 3.4 an overlap of 10 µm was sufficient.

3.2.4 Contact & Crease Model Interaction

Self-contact is critical for modeling the packaged configuration of creased sheets. In both Abaqus/Explicit and LS-Dyna, contact can be specified as either pairs of master and slave surfaces, or a single surface under self-contact. For sheets with a large number of creases and individual facets, utilizing a single self-contact surface is simpler and more robust.

In LS-Dyna self-contact can be applied through the Automatic_Single_Surface keyword, while in Abaqus/Explict the *General Contact* command is used. To stop the self-contact conditions from conflicting with the tied constraint or connector elements forming the crease, elements on one side of every crease are excluded from the self-contact surface, as illustrated in Figure 3.2(b). At vertices, only one facet can be part of the self-contact condition. If this is insufficient for capturing all the contact that occurs in the structure, additional self-contact surfaces can be defined.

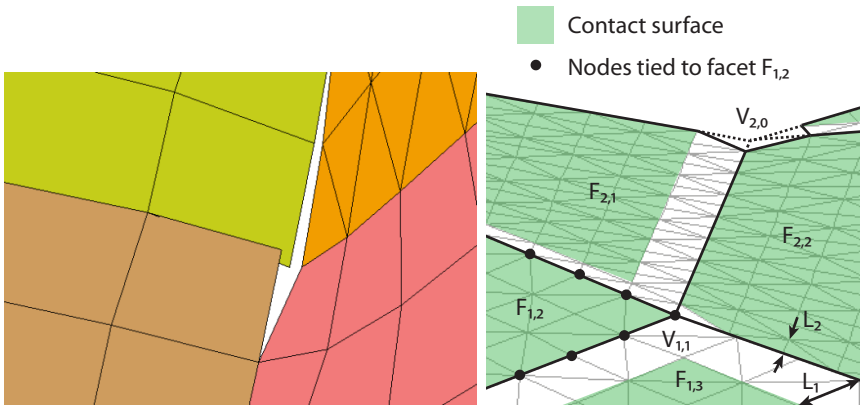

Figure 3.2: (a) Vertex not subjected to tie constraint in LS-Dyna due to insufficient overlap between the three slave parts and the master part. (b) Close up of vertex $V_{1,1}$ after surface has been meshed in LS-Dyna. Black dots are nodes from facets $F_{2,1}, F_{2,2}$, and $F_{1,3}$ that have their translational degrees of freedom tied to facet $F_{1,2}$. Green highlighted regions are included in the self-contact condition, white regions are excluded to avoid interference with the creases.

3.3 Benchmark Problem

To develop a robust technique for finding the folded configuration of a creased thin-film structure, a benchmark problem was selected. This problem is the folding of a thin-film sheet according to the GP92 crease pattern proposed by Guest & Pellegrino [12]. The GP92 crease pattern is shown in Figure 3.3, and consists of n radial sectors. Solid lines represent mountain folds that fold out of the page, while dotted lines are valley folds and fold into the page. Individual regions separated by creases are called facets. Each radial sector is bordered by two major creases which fold up to π radians and contain m minor creases which fold to $\frac{2\pi}{n}$ radians. Facet and vertices are labeled $F_{i,j}$ and $V_{i,j}$, with i corresponding to the radial sector and j to the facet number from the hub. P_0 & P_1 are locations on the creases used to define regions used during folding.

This crease pattern enables biaxial compaction and was proposed as part of a study of packaging schemes for solar sails. In addition to being a practical problem, there are several aspects that make the GP92 crease pattern ideal for testing the packaging and deployment behavior when excluding crease bending stiffness. Firstly, to accurately model the deployment of the sheet, both twisting and bending of the facets need to be captured. Secondly, in the folded state the thin-film layers are tightly packed together and any in-depth analysis of the structure must capture this self-contact and the contact between the film and the hub.

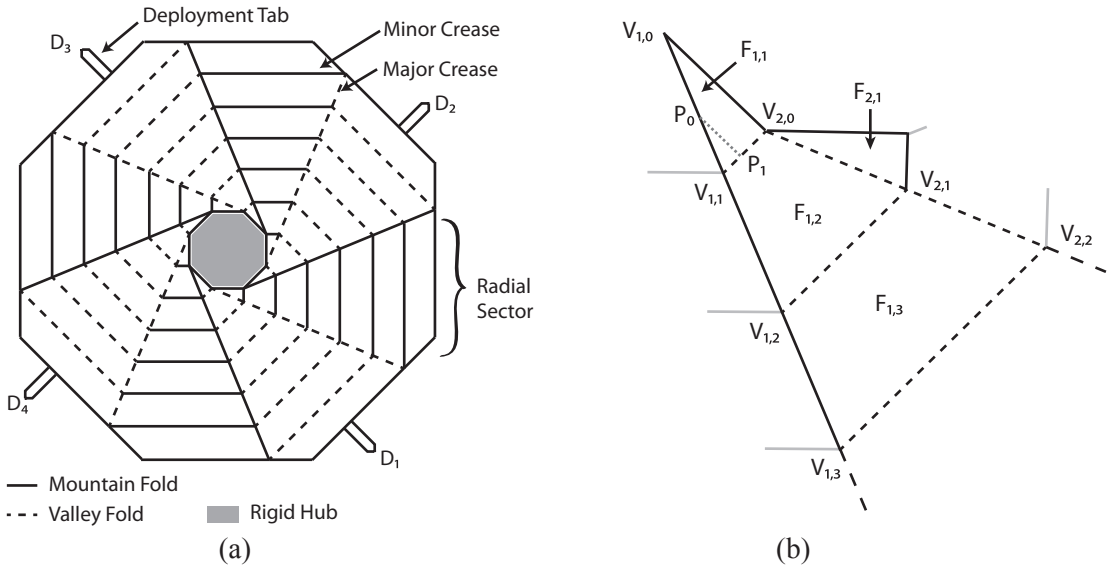

Figure 3.3: (a) Test case GP92 crease pattern that enables wrapping a thin-film around a polygonal hub. Here there $n = 8$ major creases and $m = 6$ minor creases per radial sector. This corresponds to six quadrilateral and one triangular facets per radial sector. (b) First three facets in radial sector 1, facets are labeled $F_{i,j}$ and vertices $V_{i,j}$.

The folding of this crease pattern has been studied as a kinematic structure [18], where the crease pattern was represented as a pin-jointed structure. The deployment behavior of this crease pattern has also been studied experimentally [3] and can be compared against deployment simulations, as covered in Section 3.8.2. In the experiments 50 µm thick polyamide film with Young's modulus of 2.5 GPa and Poisson's ratio of 0.3 was used. The octagonal film had a diameter of 244 mm and was first perforated with a laser cutter to create preferential crease locations, then folded around a 20 mm radius polygonal hub. Finally the hub was suspended with string. Deployment was controlled by linear actuators that pulled the tips of the tabs radially outwards.

The radial force required to deploy the wrapped GP92 fold pattern is plotted in Figure 3.4. The deployed fraction d_f is defined as

$$d_f = \frac{R - R_{Packaged}}{R_{Deployed} - R_{Packaged}} \tag{3.2}$$

where R is the tab radius, $R_{Packaged} = 54$ mm, corresponding to the hub radius plus the tab length. $R_{Deployed} = 144$ mm is the tab radius when the structure is fully deployed.

The experiments showed three broad force peaks with the force dropping to zero between these

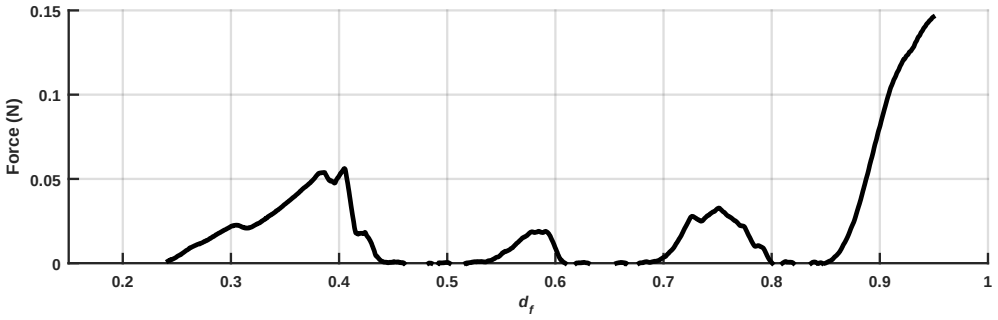

Figure 3.4: Average radial force required to deploy the folded GP92 creased film [3].

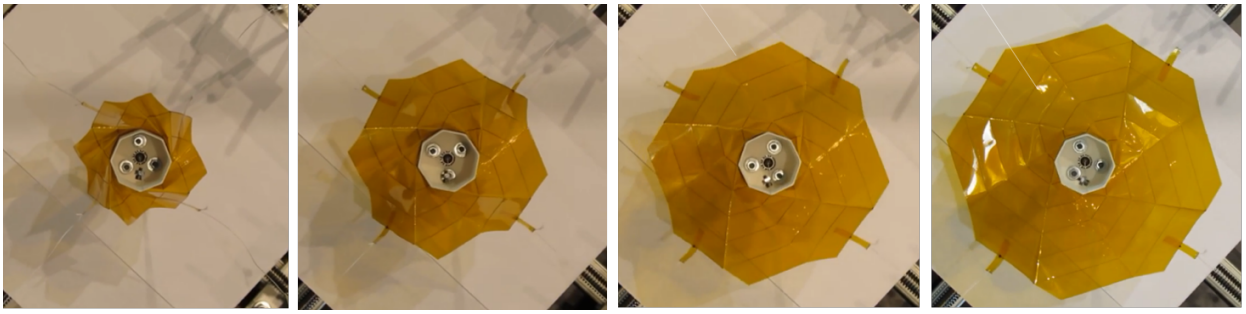

Figure 3.5: Top views of experiment at force equilibrium points. Snapshots taken at $d_f = 0.24$, 0.44, 0.62, 0.80 [3].

peaks. The regions where the force equals zero are caused by the structure over-deploying and the tabs going slack. When the structure over deploys, it is jumping to a stable equilibrium configuration with a larger radius. The tabs remain slack until d_f corresponds to the radius of the equilibrium configuration. Three different equilibrium configurations can be clearly seen during deployment, occurring at deployed fractions of 0.44, 0.62, and 0.8. Each configuration corresponds to the unwrapping of another ring of facets. In the packaged state 2.5 facets are deployed, then 3.5, followed by 4.5, and finally 5.5 as shown in Figure 3.5. After the deployment fraction exceeds 0.85, the creases are opened beyond their neutral angle causing the deployment forces to significantly increase.

3.4 Simulating Wrapping of a GP92 Creased Thin-Film Sheet

To package the GP92 crease pattern in Abaqus/Explicit and LS-Dyna software, two separate folding approaches were investigated. In the first instance, the creases are formed as a row of pin-joints created by connector elements in Abaqus and the sheet folded with boundary conditions. In the

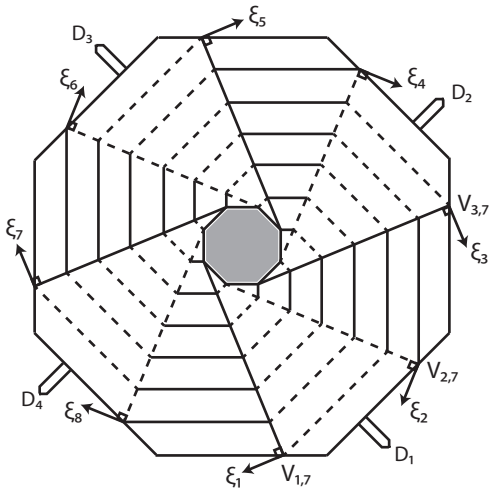

Figure 3.6: GP92 fold pattern showing local coordinate directions ξ_i, associated with vertices $V_{i,7}$. To enforce symmetry these vertices are constrained to not move in ξ_i directions during folding. During the deployment stage radial displacement boundary conditions are applied to $D_1 - D_4$.

second, creases were modeled with tied constraints in LS-Dyna, and the sheet folded with boundary conditions and forces. The simulations were designed to match the experiments performed by Arya [3], with thin-film sheet of 50 µm thick polyamide (Kapton) film, Young's modulus of 2.5 GPa and Poisson ratio of 0.3. The exact crease pattern simulated is shown in Figure 3.6. The gray region in the center is the eight sided polygonal hub 20 mm in diameter. To enforce axi-symmetric wrapping the nodes at the ends of the major creases, labeled $V_{1,i}$ are constrained against movement in the ξ_i direction. D_1 to D_4 are tabs used to deploy the packaged sheet and validate the deployment force and behavior against the experimental data.

3.5 Folding GP92 Crease Pattern with Zero-Stiffness Creases in Abaqus/Explicit

The Abaqus model consists of a rigid eight-sided polygonal hub whose translational and rotational degrees of freedom, except about Z, are fully constrained. The Kapton sheet is modeled as 56 separate parts, with connector elements representing the creases, as shown in Figures 3.7(a) and 3.7(b). Each Kapton part contains 100 S4 quadrilateral or S3 triangular shell elements, each with five thickness integration points. The translational degrees of freedom of the facet nodes adjacent

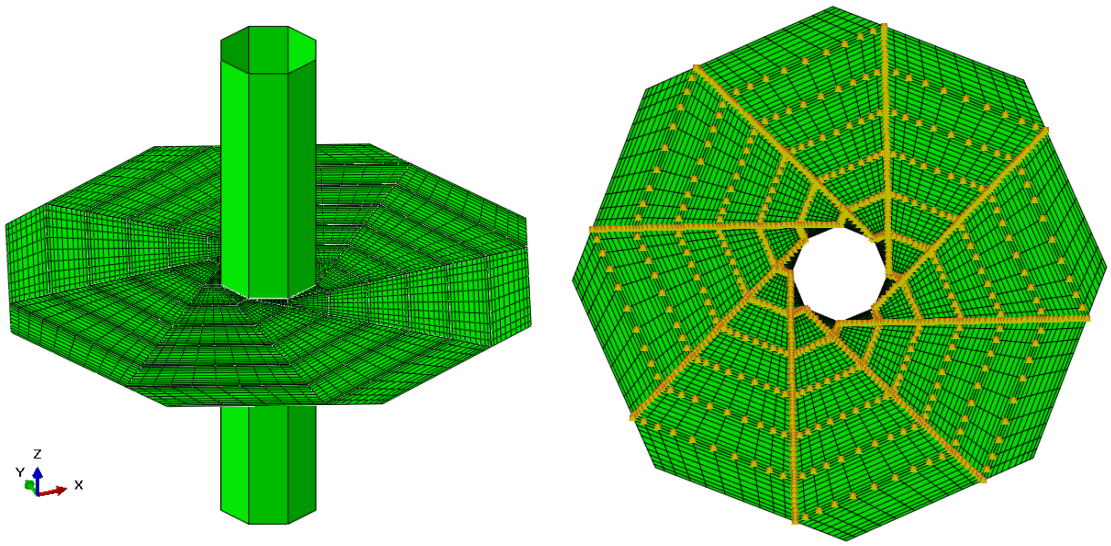

(a) (b)

Figure 3.7: (a) Abaqus/Explicit FEA model of GP92 crease pattern with $n = 8$, $m = 6$. (a) Isometric view, and (b) top view. Yellow triangles correspond to connector elements that model the creases.

to the hub are tied to the hub itself.

Boundary conditions are applied smoothly with the Abaqus/Explicit command **Amplitude, Definition = Smooth Step*. This prescribes the boundary conditions to follow a fifth order time dependent polynomial with the first and second time derivatives equal to zero at the beginning and end of the time interval.

To reduce vibrations two types of damping were implemented. The first type of damping, viscous damping, introduces a velocity-dependent normal pressure on the shell elements. The total opposing force is

$$\underline{F_v} = -\gamma A \underline{v} \tag{3.3}$$

where A is the surface area, γ the viscous damping coefficient, and $\underline{v}$ the nodal velocity.

The second type of damping, bulk viscosity, introduces an in-plane strain-rate dependent pressure

$$p_b = \xi \rho c_d l \dot{\epsilon_v} \tag{3.4}$$

and an in-plane curvature-rate dependent moment [24].

$$m = \xi \frac{t^2}{12} \rho c_d \dot{\kappa} \tag{3.5}$$

where ξ, and l denote the fraction of critical damping in highest frequency mode and the element length, respectively. ρ, t, and c_d are the density, shell thickness, and wave speed, respectively. The exact damping profile is shown in Appendix A.

To apply contact between the layers, general contact was applied to all surfaces, with the elements adjacent to the creases excluded as specified in Section 3.2.4. To ensure numerical errors do not disrupt the energy balance, Abaqus inputs artificial energy during contact and when elements distort.

3.5.1 Folding with Hub and Facet Rotation

Folding is a four step process. This section provides an overview of the process, with additional details in Appendix A. In the first step, boundary conditions are applied to rotate each triangular facet 90° over a period of 0.07 s so each facet surface becomes parallel to the local hub surface. This time was selected to ensure kinetic energy was $< 5\%$ of internal energy at the end of the folding step. The boundary conditions are applied smoothly via Abaqus/Explicit's *Smooth Step* command. The hub is allowed to rotate freely about Z during this step. In step 2, the rotational boundary conditions acting on the triangular facets are removed, and arbitrarily large peak viscous damping of $\gamma = 50,000$ Ns/m^3 is applied to the Kapton to damp out all excess vibration and kinetic energy. In step 3, the hub is rotated 150° over a period of 0.14 s to complete the wrapping process.

Throughout the simulation the outermost nodes of the major crease lines have boundary conditions applied that enforce zero circumferential motion about Z, as specified in Figure 3.6.

The simulation was stopped after the hub rotated 80° due to excessive wrinkling. Snapshots of the sheet at the end of the rest step and when the simulation was stopped are shown in Figure 3.9. As shown in Figure 3.9(a) and 3.9(c), the resulting folded configuration was not completely rotationally symmetric. Slight perturbations, due to vibrations, mean the major crease along two arms were not sharp. As rotation continues dimples form along these arms and cause half of the wrapped pattern to bunch up. At the end of the folding stages stress concentrations of 81 MPa form at the vertices. Also, several geometric imperfections have formed in the partially folded state as

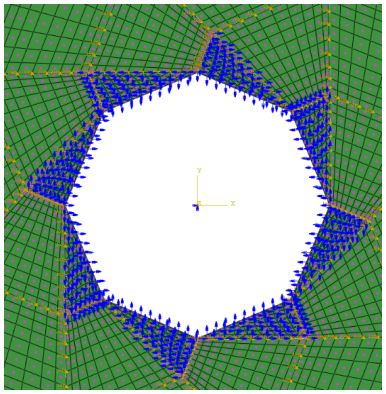

Figure 3.8: (a) Schematic of rotational boundary conditions applied to the triangular facets during step 1.

shown in Figure 3.9(d). Once in place, geometric imperfections continue to grow and act as stress concentrations. These include vertex formation where a crease forms a saddle configuration. In addition, since the creases have zero bending stiffness in the transverse direction they can lose a crisp definition as Figure 3.9(a) shows. Once a kink in the meshed surface forms away from a crease line, it becomes locked in position. As wrapping continues, the stress concentrations increase to 124 MPa at the vertices.

Figure 3.10 shows the energy in the simulation. The folding step occurs from 0 s to 0.07 s. The non-kinematic nature of folding is clearly evident in the large change in internal energy during folding. Artificial energy does build up to 0.0017 J, or 35% of the internal energy at the end of the folding step. However, once the boundary conditions on the triangular facets are released and viscous damping applied the ratio of artificial to internal energy drops to 5.8%.

3.5.2 Removing Vertices

Enforcing rotation of the triangular facets creates an over constrained problem that requires the adjacent quadrilateral facets to deform. This creates a stress singularity near the vertices of the quadrilateral facets adjacent to the hub. To reduce this stress, the elements surrounding these vertices were removed as shown in Figure 3.11. By removing these elements the vertex no longer acts as a stress singularity, and the sheet requires less energy to fold, as shown in Figure 3.13.

Removing the elements minimized the formation of geometric imperfections during the folding and wrapping steps, depicted in Figure 3.12(c). The lack of geometric imperfections allowed the

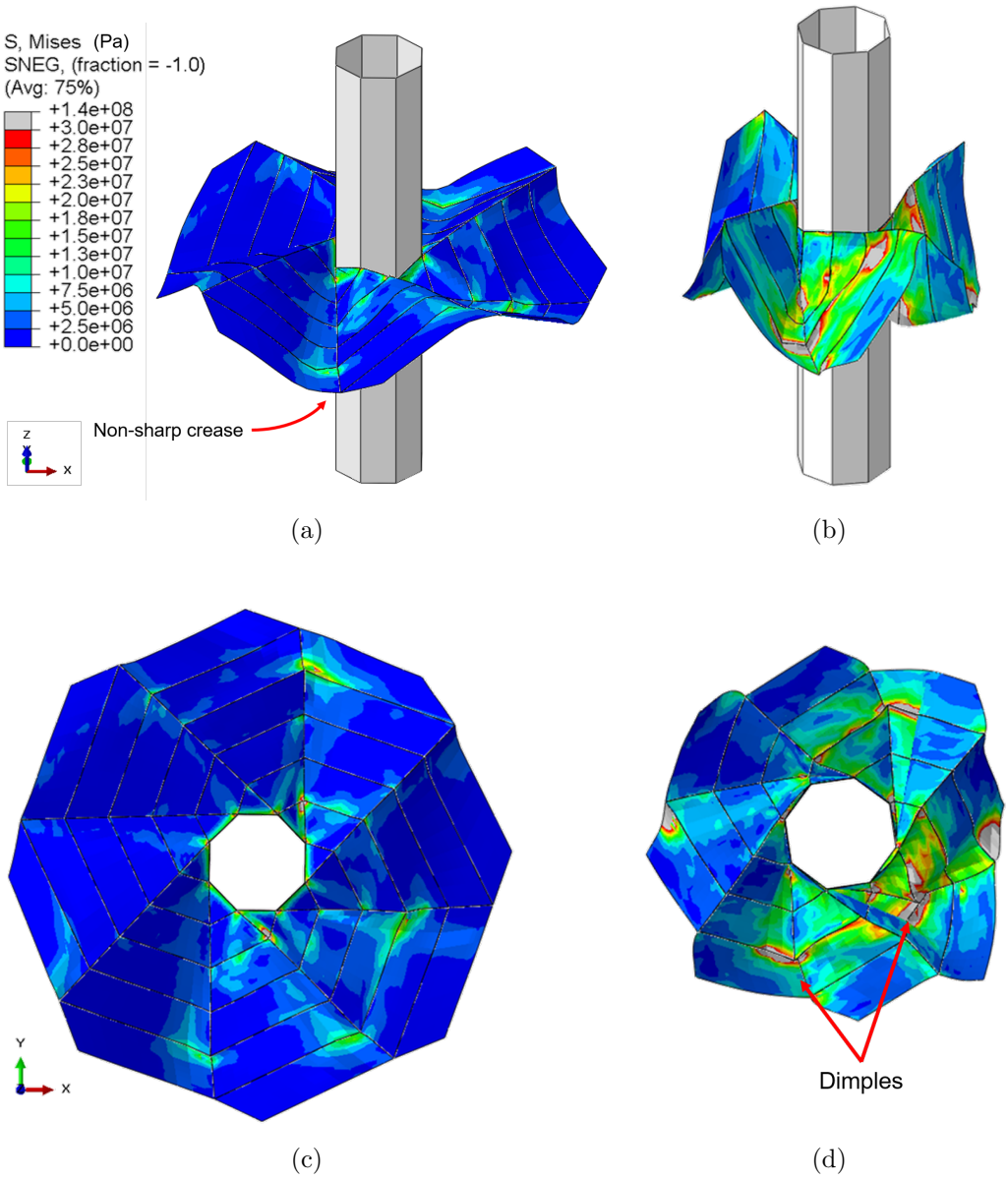

Figure 3.9: Von Mises stresses within the creased thin-film sheet during folding in Abaqus/Explicit. (a), (c) the end of the rest period after folding, and (b), (d) 0.07 s through the wrapping step, corresponding to hub rotation of 80°.

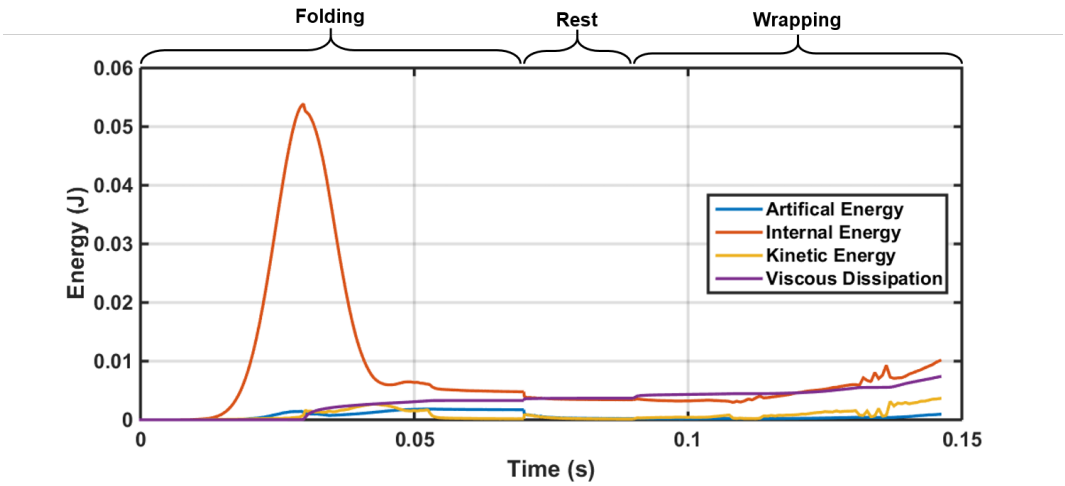

Figure 3.10: Energy in Abaqus/Explict wrapping simulation of the GP92 crease pattern.

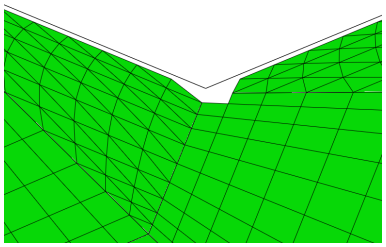

Figure 3.11: Removing elements closest to the hub vertices, to reduce the stress concentration.

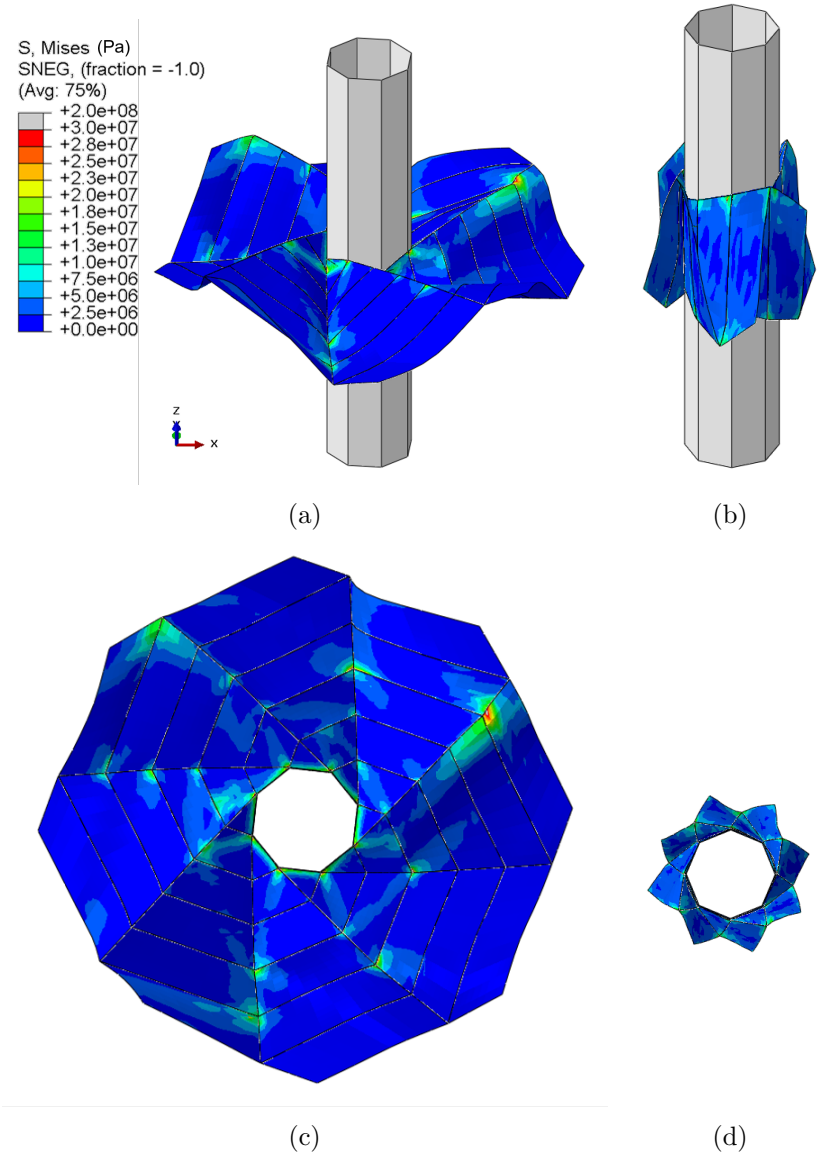

Figure 3.12: Von Mises stresses within the creased thin-film sheet during folding for the Abaqus/Explicit scenario where the vertices closest to the hub were removed. (a), (c) the end of the rest period after folding, and (b), (d) 0.14 s through the wrapping step, respectively.

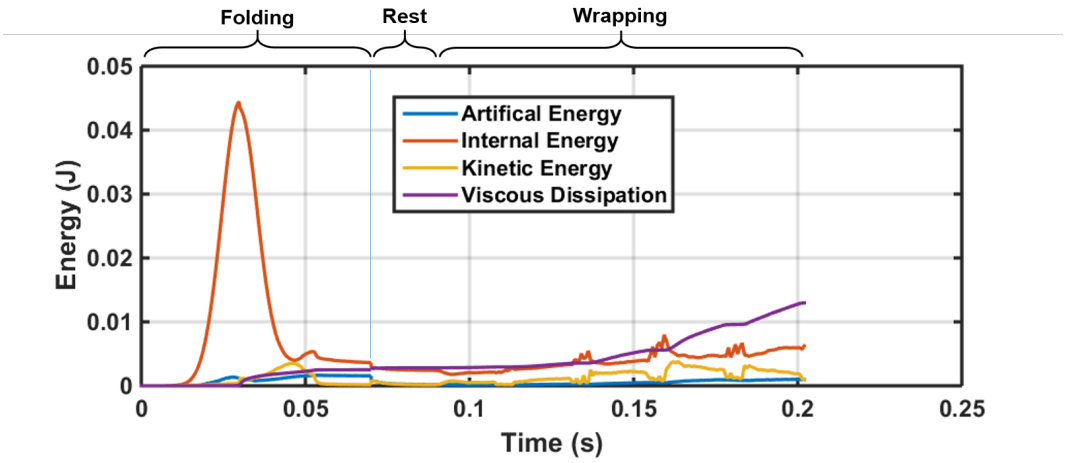

Figure 3.13: Energy in Abaqus/Explict simulation of GP92 crease pattern for the case where elements surrounding the vertices closest to the hub have been removed.

sheet to be more tightly wrapped, with the hub rotated through an angle of 150° and a final wrapped configuration in Figure 3.12(b).

Despite wrapping to 150° instead of 80° the internal energy is only 62% as large as the previous simulation. This is due almost entirely to the lack of geometric imperfections causing stress concentrations and crumpling.

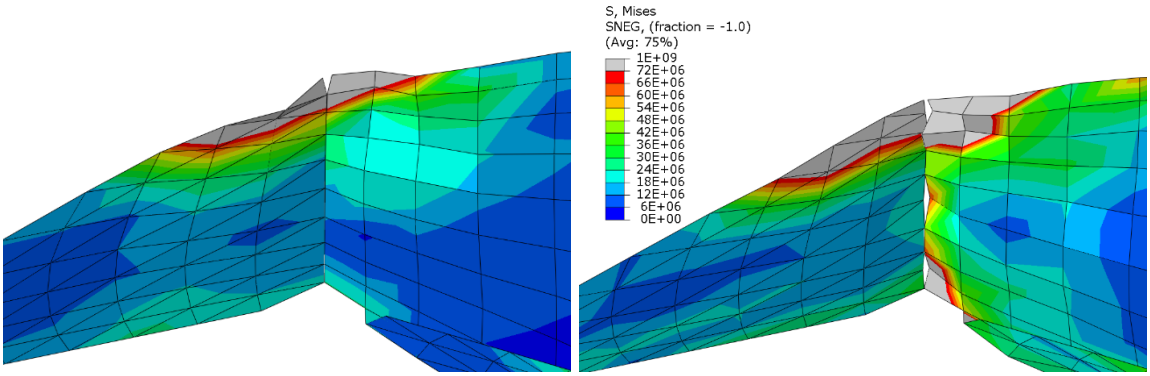

(a) (b)

Figure 3.14: Minor crease between the triangular facet and an adjacent quadrilateral facet (a) end of wrapping step, and (b) first increment into the following rest step. Other facets are hidden for clarity.

The major impediment to applying Abaqus/Explicit to modeling the packaging of creased thin-film sheets is detailed in Figures 3.14(a) and 3.14(b). At the end of the wrapping step shown in

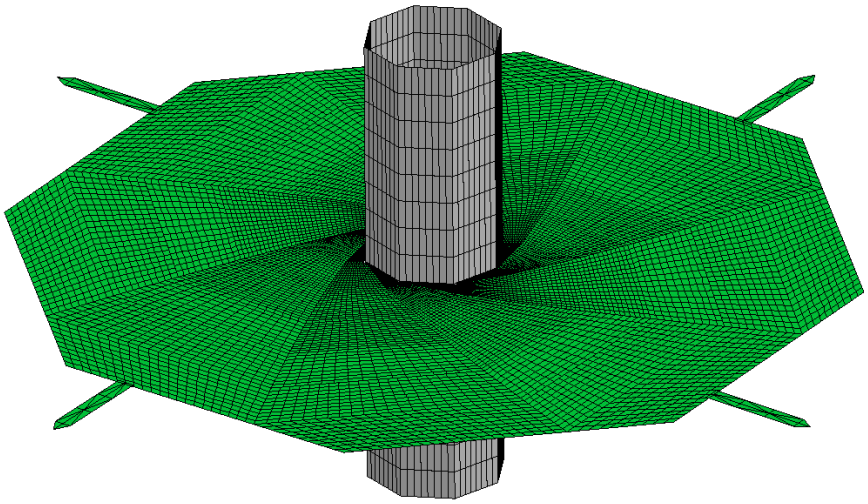

Figure 3.15: LS-Dyna FEA model of GP92 crease pattern.

Figure 3.12(b) the facets are tightly packaged against each other. Under these conditions when Abaqus/Explicit changes from one step to another, some of the connector elements no longer constrain the nodes on adjacent facets to have the same translational degrees of freedom, even without any additional external loads. Reducing this effect is possible but requires multiple iterations of the wrapping step.

Due to both the artificial energy buildup and the connector element issues, folding initially flat creased sheets in Abaqus/Explicit was not pursued further. The deployment of the GP92 crease pattern when starting from a folded configuration is still performed with Abaqus/Explicit in Section 3.9.

3.6 Folding GP92 Crease Pattern with Zero-Stiffness Creases in LS-Dyna

The implementation in LS-Dyna of the GP92 crease pattern, with zero-stiffness creases is shown in Figure 3.15. Each triangular and quadrilateral facet was meshed with between 256 and 512 C^0 triangular and quadrilateral Belytschko-Wong-Chiang shell elements. Details on LS-Dyna shell elements can be found in Section 2.2. Mesh convergence studies and the effect of element type for the unfolding is detailed later in Section 3.9.

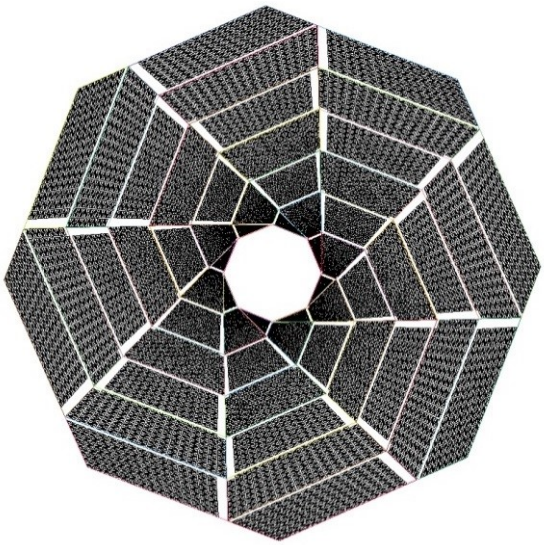

Figure 3.16: Self-contact surface implemented for the LS-Dyna simulation of GP92 crease pattern. Self-contact surface not defined for the elements along one side of each crease to avoid conflict between crease tie-constraint and self contact.

As specified in Section 3.2.3, creases are formed by tying the translational degrees of freedom of the nodes on the edge of one facet to the elements of the adjacent facet. An overlap of 10 µm between facets for elements of side length 2 mm or less was found to be acceptable for ensuring the tied constraints initialized in the following simulations.

Self-contact of the Kapton sheet was implemented with the Automatic_Single_Surface command. To avoid conflict between the tied constraints forming the creases, and the contact condition, the self-contact surface is not defined along one side of the crease. The self-contact surface is shown in Figure 3.16. Contact between the Kapton sheet and the rigid hub was implemented with the Contact_One_Way_Surface_To_Surface keyword.

Unlike Abaqus, LS-Dyna does not allow tied constraints between rigid and deformable bodies. Since the hub was modeled as rigid, the thin-film nodes directly adjacent to the hub were instead specified as part of the rigid body with the keyword `*CONSTRAINED_EXTRA_NODES_SET`. This only constrained the nodes' translational degrees of freedom.

For shell structures that undergo dynamic buckling or compressive deformation, including bulk viscosity for shell formulations in LS-Dyna simulations is recommended [23] . This was achieved by setting TYPE to 2 in the keyword `*CONTROL_BULK_VISCOSITY`. This improved the stability of the model significantly.

In LS-Dyna mass nodal damping is used instead of viscous damping. The force applied to each node by mass nodal damping is

$$\underline{F_v} = -\beta m \underline{v} \tag{3.6}$$

where β is the mass nodal damping coefficient, m is the mass of the node, v is the nodal velocity. It differs from viscous damping in that it applies a force directly opposed to the nodal motion, instead of perpendicular to the surface. The relationship between the coefficient of viscous damping γ in Abaqus and the mass nodal damping coefficient β is

$$\gamma = t\rho\beta \tag{3.7}$$

assuming a film of constant thickness t and density ρ.

3.6.1 Folding with Forces

It was shown in Section 3.5.1 that folding by purely applying rotational boundary conditions to facets can result in significant facet bending and twisting during folding. An alternative to folding with boundary conditions is to fold by applying forces to the surface.

The two types of forces used here are pressure loads and line loads. Pressure loads are applied to the triangular facets to replace the rotational boundary condition. Line loads are distributed loads applied along the creases and are applied in the ±Z direction along the major crease lines. These loads tension the creases and ensure a clear discontinuity in slope across the crease. The exact magnitude and profile of these loads are detailed in Appendix A. These forces were applied over a short time period of 0.016 s.

Figure 3.18 clearly shows two interesting features. The first is the major creases are crisp and provide a sharp discontinuity between the facets, without geometric imperfections. The second is that there are high stress concentrations in the triangular facet despite the removal of elements surrounding the hub vertices. During folding the triangular facets are allowed to bend, as shown in Figure 3.19(a). When folding purely with pressure and line loads however the major crease line bordering the triangular facet is under compression loads of -5 MPa. This causes the facet to crumple, as displayed in Figure 3.19(b).

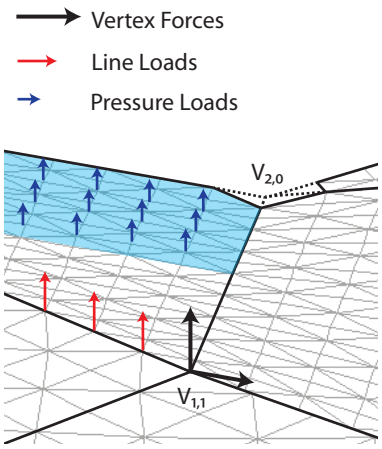

Figure 3.17: Schematic of a creased surface being folded by point, line and pressure loads.

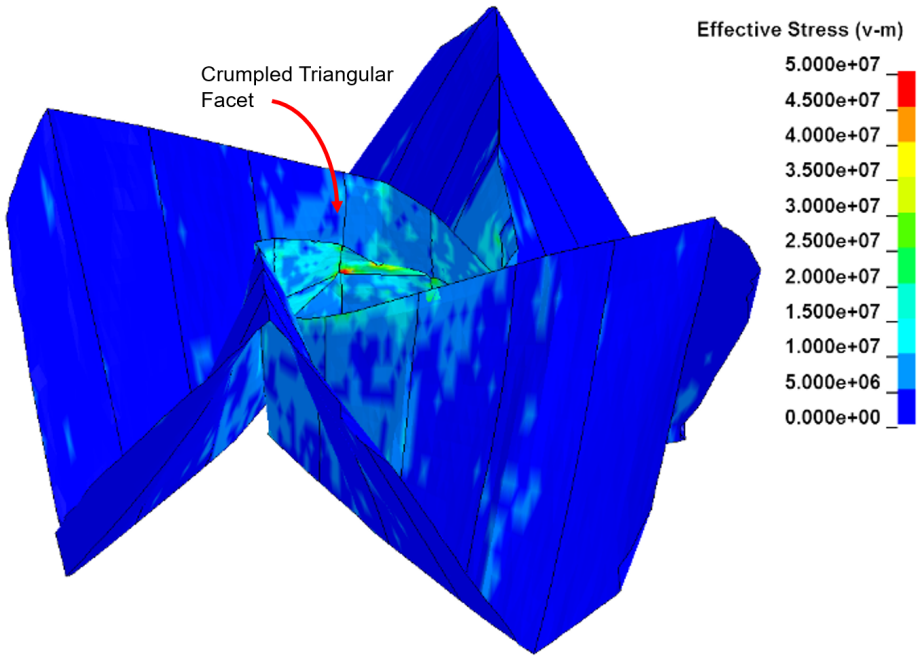

Figure 3.18: (a) Von Mises stress distribution in the wrapped sheet 75% of the way through folding. Stress concentrations up to 141 MPa are present at the vertices of the triangular facets. The hub has been hidden for clarity.

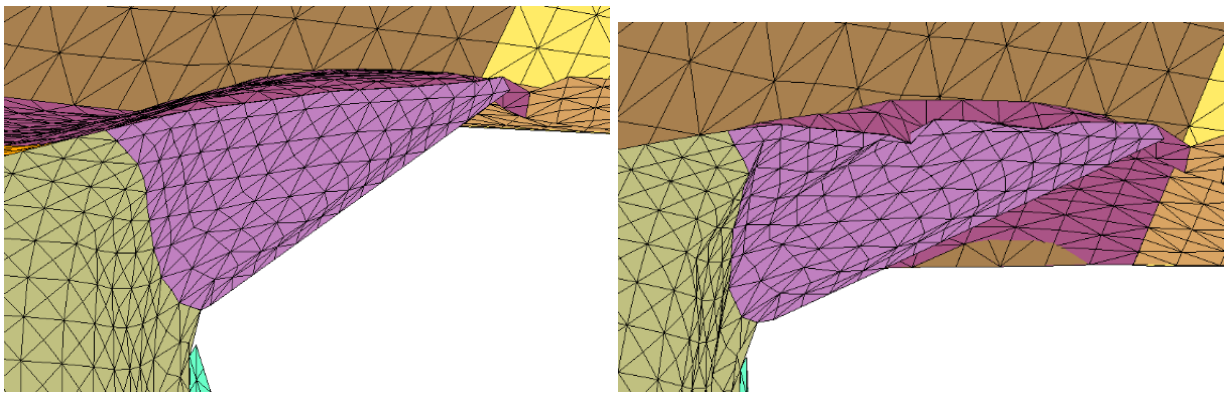

(a) (b)

Figure 3.19: Close up of the triangular facet crumpling during folding at (a) 23% and (b) 30% of the way through the folding step. To clearly show the crease line between the triangular and quadrilateral facets the individual facets are shown in separate colors, and the hub hidden for clarity.

A further challenge is that, to fold rapidly, forces of up to 0.15 N are applied. When folding is complete, the outermost facets end up moving at speeds up to 6 m/s. This results in significant contact and vibration between the layers. In addition, the hub continues to rotate until the facets are fully wrapped, and then there is a shock load at nodes $V_{i,7}$ since these nodes are constrained in the circumferential direction. This shock load causes additional geometric defects to occur in the packaged configuration.

3.6.2 Including Mass Nodal Damping and Vertex Forces

The packaged state obtained in the previous simulation had two key problems. First the triangular facets crumpled during folding and second, at the end of the wrapping process, shock loads generate geometric defects.

To remove the crumpling of the triangular facets, point loads in the ± Z direction were applied to the triangular facet verticies. The exact load profiles can be found in Appendix A. These forces tension the triangular facets and both minimize crumpling during folding as well as removing the geometric defects caused by crumpling after they form. This prevents these defects from becoming locked in place between multiple Kapton layers.

To remove the shock loads that occur at the end of the wrapping stage, arbitrarily large mass nodal damping of up to $\beta = 40,000$ s^{-1} was applied 0.016 s into wrapping. It was at this stage

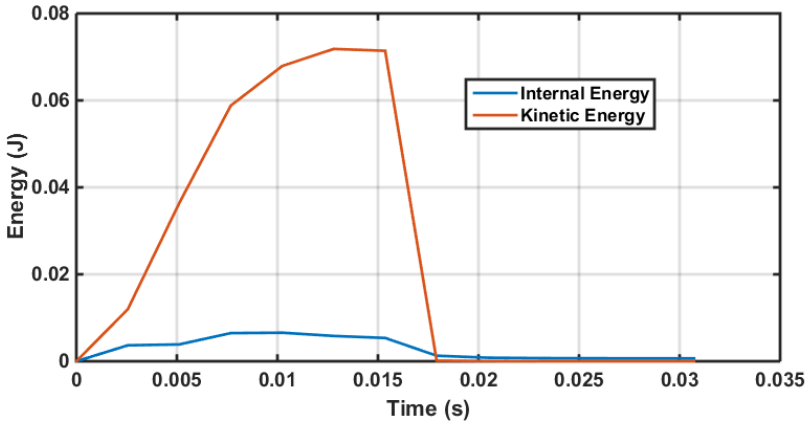

Figure 3.20: Internal and kinetic energy in final LS-Dyna packaging simulation. Packaging ends at 0.016 s, and viscous damping is applied for 0.016 s following that.

in the wrapping process that 2.5 facets remained unwrapped, which corresponded to the starting configuration for the deployment experiments, as shown in Figure 3.5. This completely removed the kinetic energy in the system, as shown in Figure 3.20. The non-uniform profile detailed in Appendix A was used so the Kapton sheet could reach an equilibrium configuration.

The triangular facets experience significant compression during and after folding, as Figure 3.22 shows. Without sufficient tensioning forces during folding, this stress would cause many wrinkles to be present in the folded configuration. The compression in the triangular facets and the large tensile stresses in the first ring of quadrilateral facets are caused by the innermost facets being overly constrained during folding. Simulations starting in the initially folded configuration completely neglect these stresses.

Figures 3.21(a) and 3.21(b) show an axi-symmetric wrapped state with few geometric imperfections, distinct major crease lines and triangular facets that are not crumpled. Qualitatively the packaged configuration is close to that experimentally observed in Figure 3.5. In Section 3.9 this model is validated by comparing the required deployment force in the simulation with the experimental results in Figure 3.4.

3.7 MCFF Modeling Technique

The knowledge gained in the previous sections can be distilled into a standardized approach to modeling the folding of creased thin-film sheets.

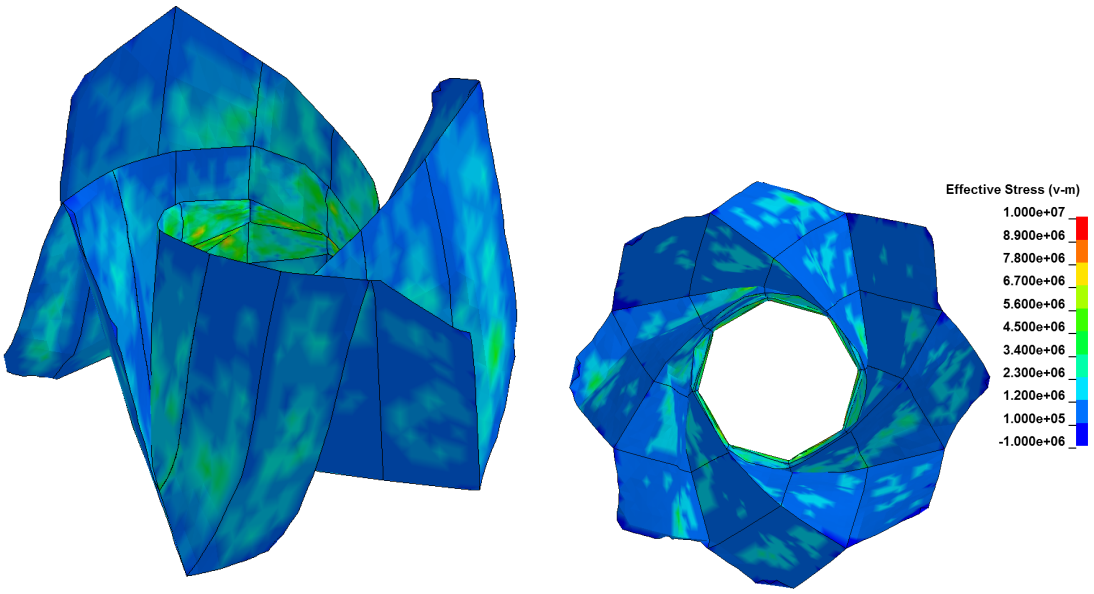

(a) (b)

Figure 3.21: Von Mises stress distribution at end of wrapping stage for LS-Dyna simulation incorporating pressure, line and point loads (a) Isometric view, and (b) top view.

The Momentless Crease Force Folding (MCFF) approach is detailed in Figure 3.23. The MCFF approach starts with the crease pattern in the flat configuration. The facets are generated as separate shell element parts with an overlap between the facets of up to 25 µm for elements with edge length $\leq$ 2 mm. Tie constraints then constrain the nodes of the facets on one side of a crease to the shell elements on the other side of the crease. At vertices where the folding process is over-constrained, the surrounding elements are removed to reduce stress concentrations. Next, a self-contact surface that excludes elements along one side of every crease is defined, to ensure that the tie constraints do not conflict with the self-contact. These steps constitute the initial configuration of the simulation.

To wrap or fold this crease pattern, three types of forces are applied. Pressure loads act as follower forces that fold facets instead of using rotational boundary conditions. Line loads are forces distributed along the length of the creases. Line loads ensure creases are sharp with a distinct discontinuity in gradient across the creases. Vertex or point loads are applied at the vertices, and serve to tension and straighten creases during folding. Point loads keep facets and creases under tension to avoid crumpling or other geometric defects from either appearing, or becoming locked

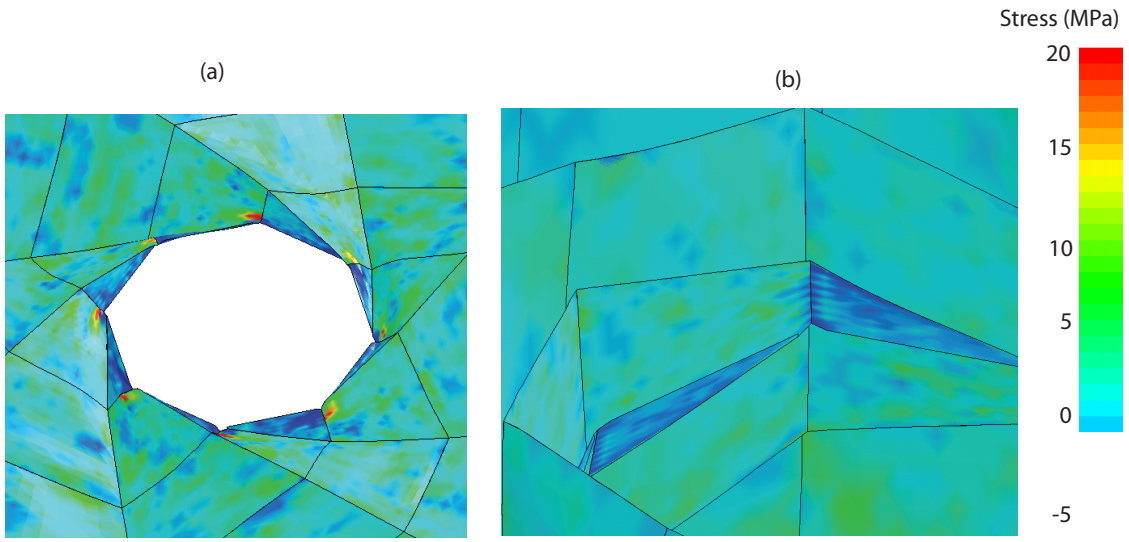

Figure 3.22: The minimum principle in-plane stress for the initially flat simulation, with close up views of the inner rings of triangular and quadrilateral facets when (a) 20% folded and (b) fully folded. The hub is not shown for clarity, and the viewing angle is the same in both (a) and (b).

into place between multiple sheet layers.

Towards the end of the wrapping step, artificially large viscous damping is applied to the creased sheet. This removes excess kinetic energy and avoids multiple layers of the creased sheet vibrating against each other at the end of the packaging process. A non-uniform damping profile, where the system is repeatedly over-damped and under-damped, allows kinetic energy to build up and be removed multiple times until the creased sheet reaches an equilibrium packaged configuration.

3.7.1 Advantages

The advantages of the MCFF technique include:

1. The moment-angle relationship of each crease does not need to be determined in advance of modeling the packaged state.

2. Lack of rotational boundary conditions ensure exact rotation vectors and angles do not need to be determined.

3. The effect of singularities is reduced by removing elements at over-constrained vertices.

4. Forces are more forgiving for folding over-constrained facets than boundary conditions.

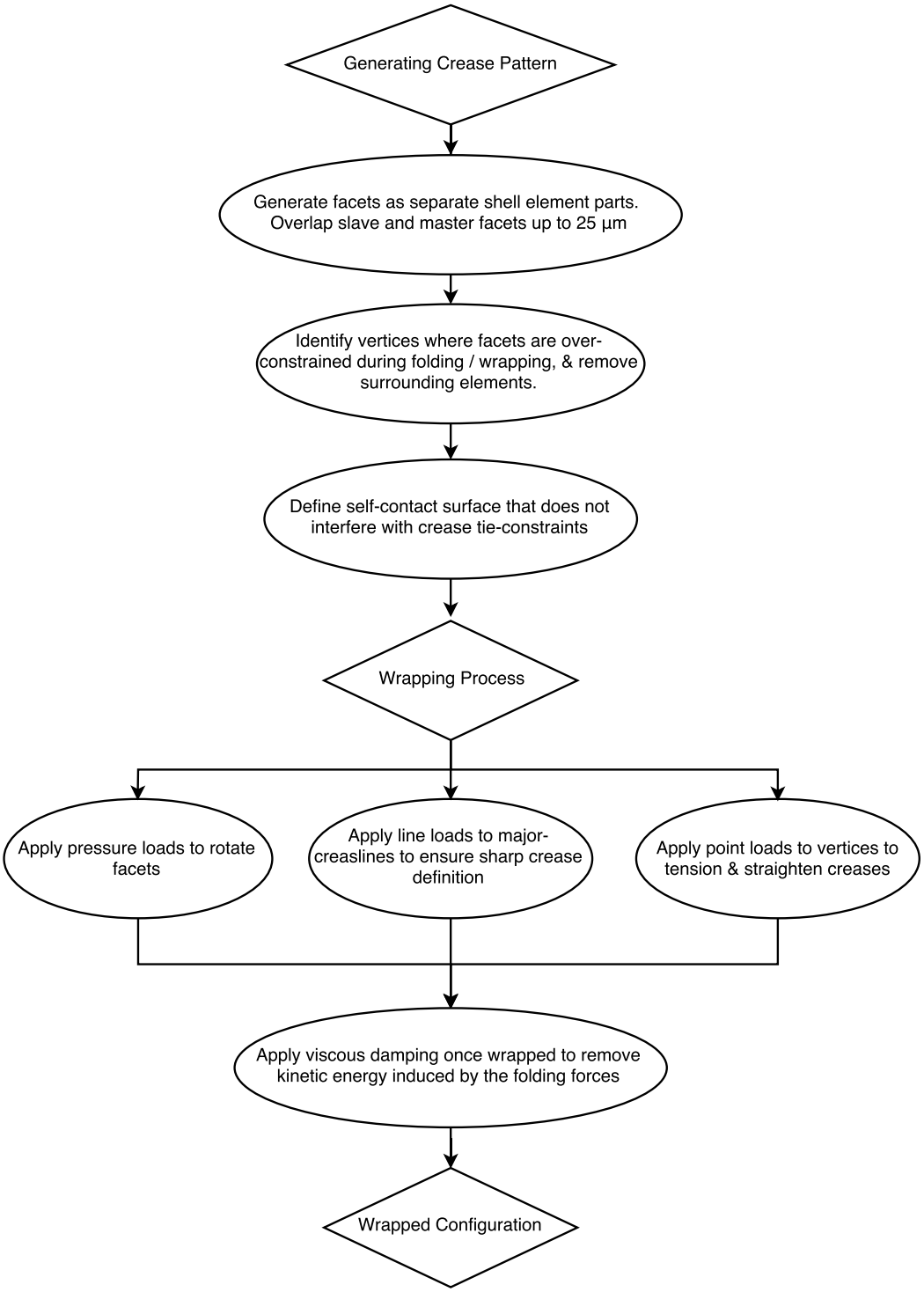

Figure 3.23: MCFF algorithmic approach to model the folding of creased sheets in LS-Dyna.

5. Viscous / mass nodal damping removes shock loads at the end of folding.

3.7.2 Disadvantages

The disadvantages of the MCFF technique include:

1. Simulation does not include actual crease bending moment.
2. Iteration may be required to determine the forces and viscous damping required to achieve the folded configuration.
3. Any geometric defects that appear during folding need to be actively dealt with by applying vertex loads, and will not disappear otherwise.

3.8 Validation of Modeling Techniques

The previous section showed how to fold a creased thin-film sheet into a packaged configuration when the creases have zero bending stiffness. The question remains: can removing crease bending stiffness result in useful information about the deployment behavior, such as the forces required to unwrap a creased thin-film structure?

To validate both the momentless-crease representation in general, and the MCFF technique in particular, the folded GP92 crease pattern was deployed in LS-Dyna, and the deployment forces compared to previous experimental work [3], detailed in Section 3.4. In addition, GP92 deployment simulations in LS-Dyna and Abaqus were performed starting from an approximated folded configuration. This is to control for the effect of momentless creases, vs. the full MCFF approach.

3.8.1 Analytical Approximation of the Folded Configuration

In the GP92 case the folded form is analytically known only in the zero thickness case, where all the radial sectors package on top of each other and $w = 0$ as in Figure 3.24. To accommodate thickness in GP92, the vertex locations can be approximated by moving their position a radial distance $w = tj$ outwards in the folded configuration, for film thickness t and minor crease number j [18]. The facet edges are then linearly interpolated from the vertex locations. With this approach each facet is defined as slightly warped (non-planar), and the entire thin-film will no longer unfold flat.

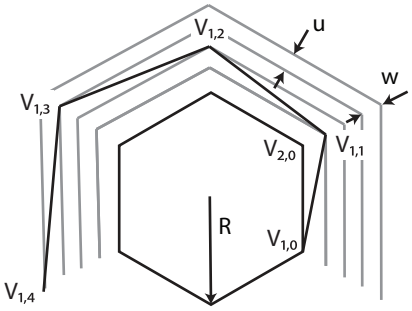

Figure 3.24: Top view of a single GP92 major creaseline when starting in an initially folded configuration. Vertices $V_{i,j+1}$ are a radial distance w further out from $V_{i,j}$ because of non-zero θ_0.

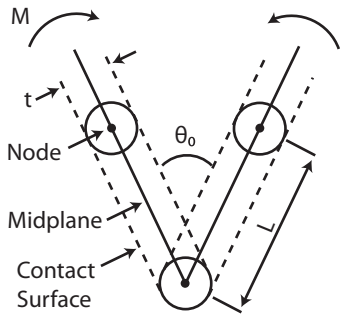

Figure 3.25: Cross-section of crease. Minimum initial fold angle θ_0 is constrained by Equation 3.8 so nodes adjacent to creases do not start the simulation with initial contact interference. In a simulation moment M depends on initial crease angle θ_0 and crease stiffness $k(\theta)$.

To avoid initial contact between tightly packaged layers in the FEA software, a non-zero initial fold angle θ_0 is required, as shown in Figure 3.25. The minimum θ_0 depends on the film thickness t and the length of the elements adjacent to the crease L

$$\theta_0 \geq 2\sin^{-1}\left(\frac{2t}{L}\right) \tag{3.8}$$

The initially folded configuration as implemented in LS-Dyna is shown in Figure 3.26.

3.8.2 Deployment Simulations

Deployment (unfolding) can be carried out in two different ways - dynamic and quasi-static. For purely dynamic simulations where exact accelerations are important, the sheet density, deployment time, and applied damping must match reality as closely as possible.

Quasi-static deployment, however, is slow and controlled. For these simulations the build up

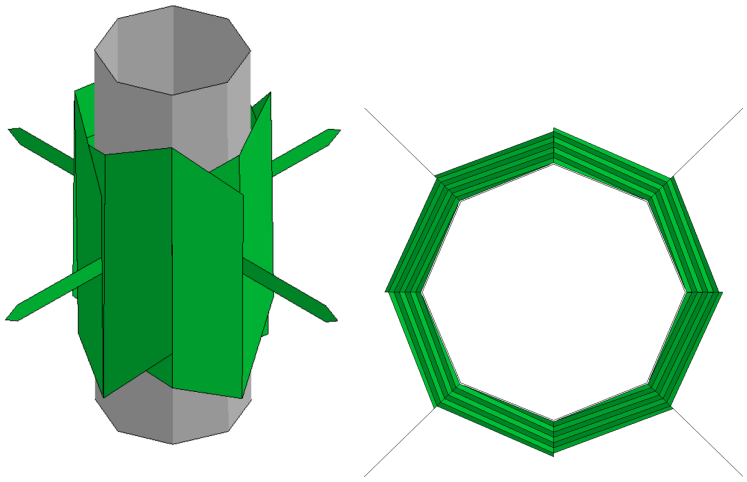

(a) (b)

Figure 3.26: LS-Dyna model of the GP92 crease pattern when starting from an initially folded configuration. (a) Isometric view, and (b) top view.

of spurious vibrations needs to be avoided in order to reduce numerically induced noise in the force deployment. Excessive vibration can change the deployment profile by providing energy for the system to jump from one configuration to a lower energy one. If damping is applied during deployment it can, however, increase the force required to unfold the sheet.

The experiments from prior work and detailed in Section 3.3 on the GP92 crease pattern were performed in a quasi-static manner, except for the naturally occurring dynamic jumps between equilibrium configurations. The solution proposed here is to break the deployment simulation into stages. After each deployment stage apply non-physical viscous damping (Abaqus) or mass nodal damping (LS-Dyna) to remove excess kinetic energy, as shown in Figure 3.27. This damping reaches a peak of $\beta_{max} = 20$ s^{-1} during the four rest periods between deployment. During the non-rest periods $\beta = 0.03$ s^{-1}. This corresponds to a γ of 0.002 Ns/m^3 in the Abaqus simulations. This value was chosen to minimize the effect of viscosity on the required deployment forces.

To match the experiments, deployment tabs were added to the GP92 crease pattern. Rather than completely controlling the boundary conditions on the edge of the GP92 crease pattern, the deployment tabs allow the structure to jump from one equilibrium configuration to another, larger radius one. In this case, the tabs will go slack and the force drop to zero, as shown by the experimental results in Figure 3.4.

To determine the effect of the MCFF approach, a deployment stage was added to the packaging

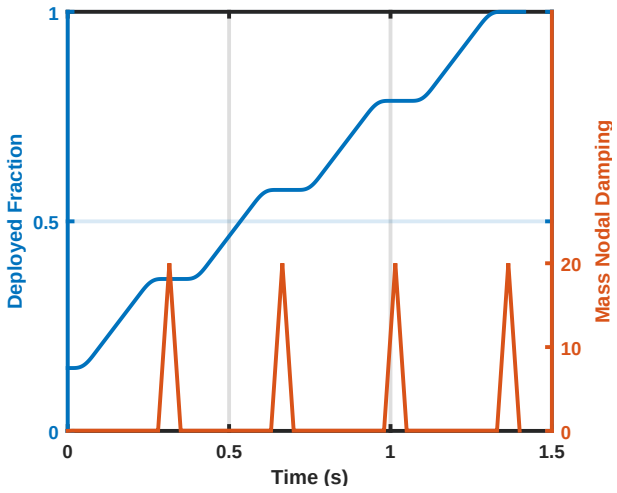

Figure 3.27: Tab displacement (d_f) during deployment and the corresponding mass nodal damping (β) used to remove excess kinetic energy.

simulation in Section 3.6.2. During wrapping the nodes labeled D_i in Figure 3.6 were moved radially inwards with boundary conditions during wrapping to completely control their position and ensure the tabs remained slack. The tabs were modeled as membranes to stop tab bending stiffness from disrupting the rotational symmetry during folding.

3.9 GP92 Deployment Results

3.9.1 Mesh Convergence Study

A mesh convergence study was performed for an initially folded GP92 crease pattern utilizing Belytschko-Wong-Chiang (BWC) quadrilateral shell elements. The resulting deployment force profiles are shown in Figure 3.28. Four cases were tested, $n = 8$, 12, 16, and 20. Here n signifies the number of elements along each edge of the triangular facet. The number of elements throughout the entire crease pattern were scaled accordingly. $n = 16$ and $n = 20$ have converged, with slight differences only at $d_f = 0.58$ and $d_f = 0.70$. For the following simulations, $n = 16$ was used to reduce the total run time.

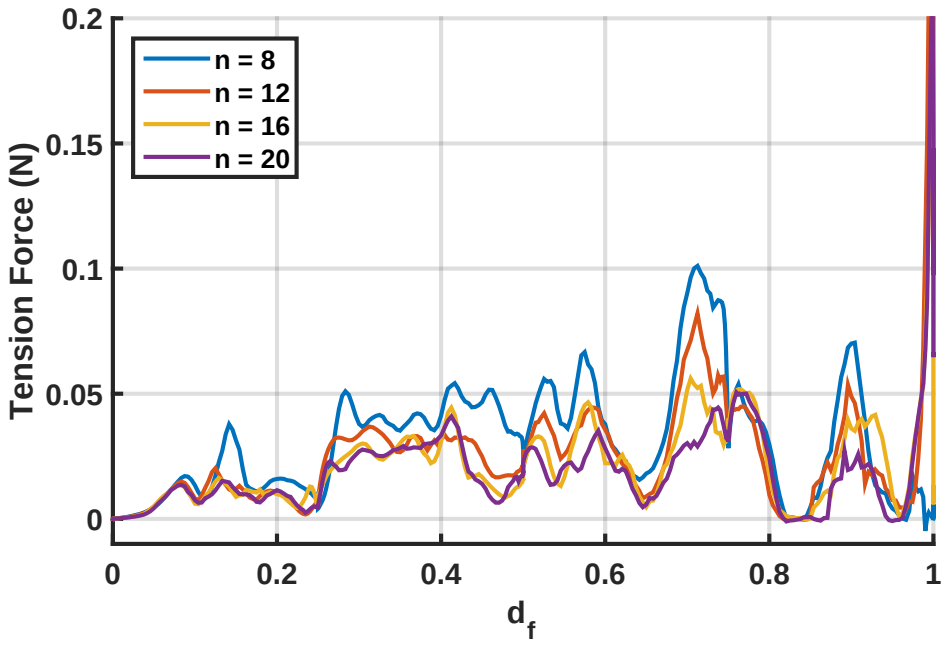

Figure 3.28: Deployment force results from LS-Dyna mesh convergence study. n corresponds to the number of elements along the edge of every the triangular facet.

3.9.2 Comparison of Initially Folded and Initially Flat Results

The effect of meshes containing BWC quadrilateral and C^0 triangular shell elements in LS-Dyna, and S4 shell elements in Abaqus were investigated. The corresponding deployment force results are shown in Figures 3.29(a), 3.29(b) and 3.29(c). The deployment forces plotted are the average forces from the four tabs. Snapshots of the deployment configurations are shown in Figure 3.30.

Like the experiments, the simulations starting from an initially folded state show three broad force peaks, each corresponding to the opening of another ring of facets, as shown in Figure 3.29(a). The regions where the force equals zero are caused by the structure over-deploying and causing the tabs to go slack. Three different equilibrium states can be clearly seen during deployment, occurring at deployment fractions of 0.44, 0.62, and 0.8.

The reduced integration BWC quadrilateral shells capture the peak forces to within factors of 1.24, 1.85, and 1.54 for the three force peaks. The force peaks are broader than those observed experimentally, potentially because the creases are not applying an opening moment. There is a spurious force peak observed at $d_f = 0.5$. This corresponds to the hub rotating as a result of the previous ring of facets opening, until tension in the deployment tabs halts rotation. Then the hub

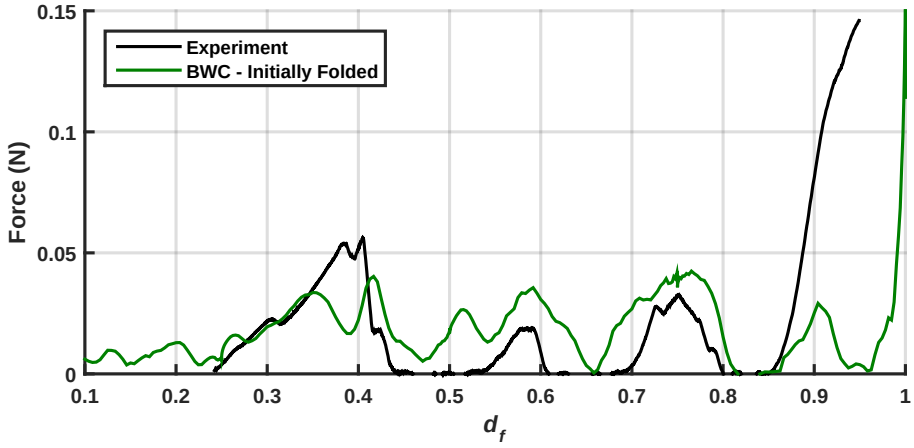

(a)

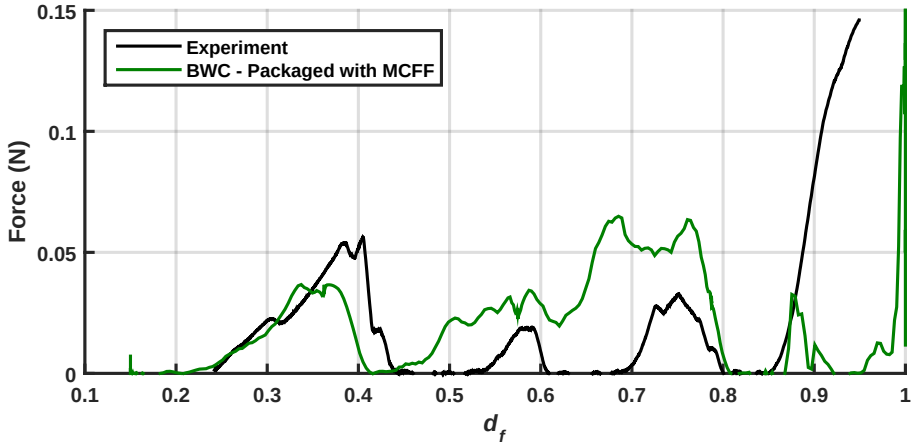

(b)

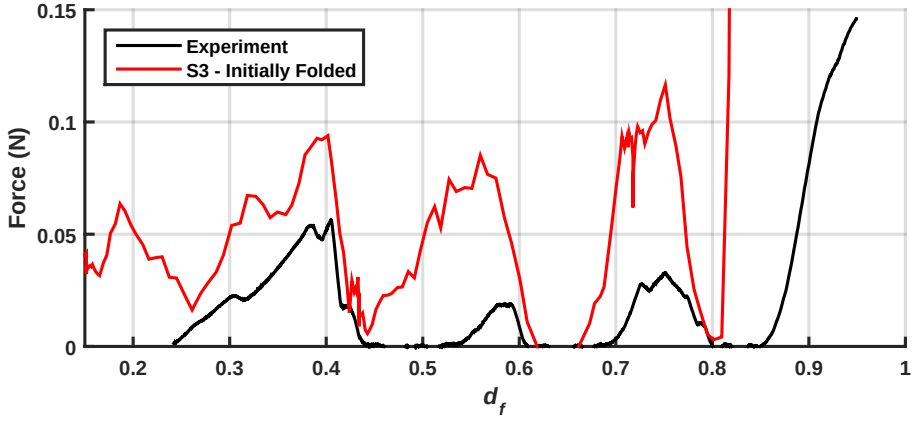

(c)

Figure 3.29: Comparing LS-Dyna deployment force profiles for BWC and C^0 shell elements for (a) the initially folded case and (b) packaged via MCFF technique, and comparing Abaqus/Explicit deployment force profiles for S3 shell elements for the initially folded case.

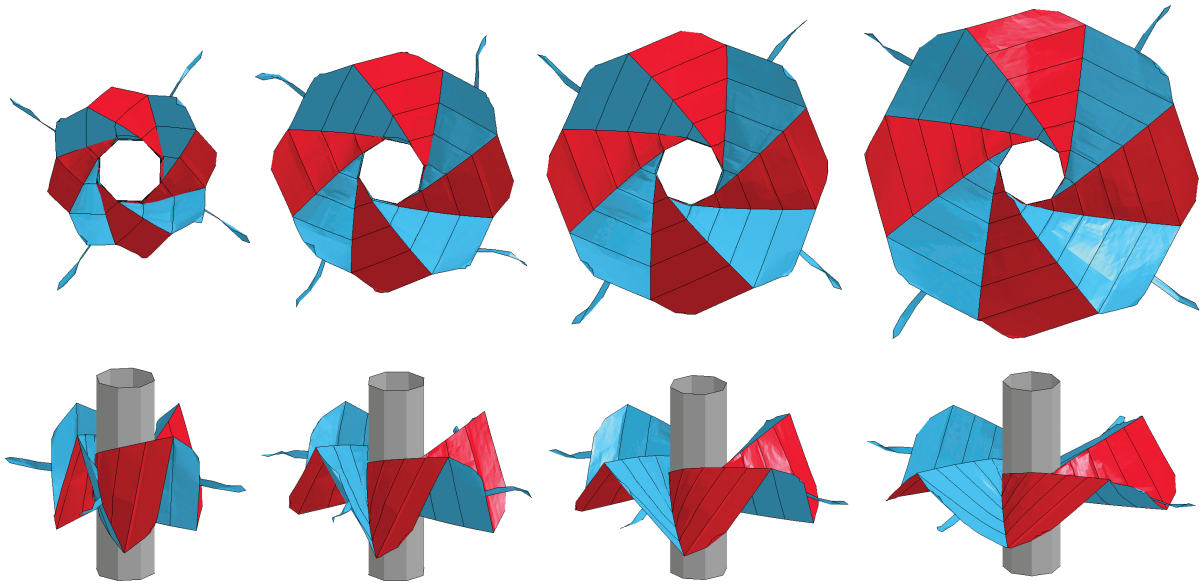

Figure 3.30: Top and isometric views of the initially folded LS-Dyna simulation at equilibrium configurations corresponding to $d_f = 0.23$, 0.42, 0.62 and 0.80.

starts to rotate in the opposite direction. This process causes additional loads on the deployment tabs, and generating a spurious peak.

The Abaqus simulation overestimates the force magnitudes by a factor of up to 4.5x, with the three equilibrium configurations clearly visible. The force increases drastically at $d_f = 0.8$ due to dimples appearing in the triangular facet mesh closest to the hub.

Both initially folded simulations show non-zero forces at $d_f = 0.18$. This corresponds to the first ring of facets opening. The experimental results differs because, due to the crease opening moment, the sheet starts with 2.5 rings of facets already unwrapped, as seen in Figure 3.5.

For the initially folded simulations the force drastically increases at the end of deployment. Experimentally this is caused by creases opening beyond their neutral state. This does not apply in the simulations as the creases are modeled with zero stiffness. For the initially folded simulations the vertex positions have been changed to allow for thickness and contact effects. With these changes the crease pattern no longer folds flat, and hence after $d_f = 0.80$ additional force is required to stretch the thin-film into a flat, fully deployed configuration.

The LS-Dyna simulations where the creased sheet was packaged with the MCFF technique in Figure 3.29(b) have similar force profiles to those starting in the initially folded configuration.

Unlike the initially folded LS-Dyna simulation, the force reaches zero at $d_f = 0.44$, showing a true equilibrium configuration. However, while a force minima can be seen at $d_f = 0.6$, unlike the experimental results it does not reach zero. The first force peak matches the experimental data force peak to within 31%, with the following two peaks a factor of 2 times greater.

The radial force on each tab required to deploy the wrapped GP92 fold pattern is plotted in Figure 3.31 for the LS-Dyna and Abaqus simulations. This data was smoothed using a five-point moving average to reduce noise. All the simulations showed significant variation in the force profiles for each tab. Two factors determine this. First, each radial sector of facets can deploy independently of each other. Second, each time the sheet jumps to a new equilibrium configuration, strain energy is converted into kinetic energy, causing vibrations.

As expected, the minima in internal energy correspond to the equilibrium configuration. The drops in kinetic energy correspond to where large viscous or mass nodal damping is applied to damp out vibrations. For the Abaqus simulation, artificial energy builds up until it is 7% of the internal energy at $d_f = 0.8$.

3.10 Discussion

To model the unfolding of creased thin-films in this chapter it has been necessary to use tools such as the tied-contact condition in LS-Dyna, or connector element in Abaqus/Explicit, for purposes for which they were not designed. In particular, determining the overlap between the nodes and elements of the tied constraint that is sufficient for the constraint to activate at the start of the simulation, while ensuring it is small enough not to affect the simulation results, can be time consuming. To best capture the crease behavior, the development of a dedicated finite element, similar to the connector element in Abaqus/Explicit, is needed. Ideally the rotational stiffness ($k(\theta)$) of this element would be specified initially, and vary non-linearly according to the difference in crease angle from a given baseline value (θ_n), including allowing for a negative stiffness value. There is potential for a user-defined connector element to perform this in Abaqus, however the challenges identified in Section 3.5 would need to be solved first. In addition, the dedicated elements would need allow for differences in mesh density on either side of the crease, and ensure the stiffness of the whole crease is proportional to the length of the crease, regardless of mesh density.

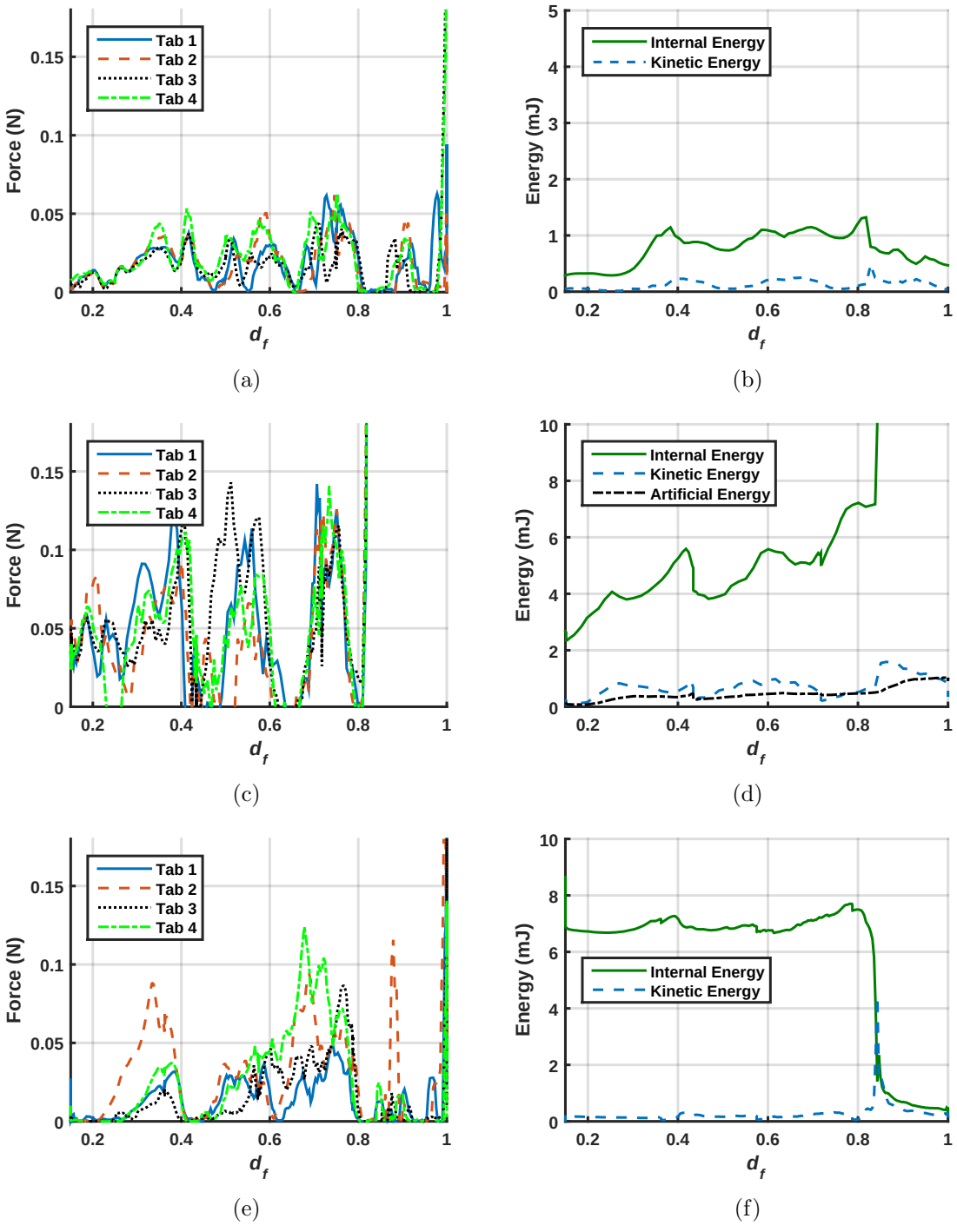

Figure 3.31: Smoothed radial force data (left) required to deploy crease pattern and the corresponding energy (right). (a), (b) are LS-Dyna results when starting from an initially folded configuration. (c), (d) show Abaqus results starting from an initially folded configuration. (e), (f) are LS-Dyna results when first folding from a flat state.

3.11 Summary

Creases have been modeled as lines of momentless hinges in LS-Dyna as tied constraints, and in Abaqus/Explicit with connector elements. Unlike simple kinks in a meshed, thin-shell surface the crease opening angle and moment do not depend upon the baseline sheet stiffness or starting angle. In addition, the momentless crease model allows creased sheets to start in a flat configuration and be packaged in the simulation. It is important, however, to ensure sheet self-contact conditions do not conflict with the tied constraints in LS-Dyna or connector elements in Abaqus/Explicit.

The benchmark problem chosen to test the effectiveness of the momentless crease model was a creased thin-film sheet, whose GP92 crease pattern allowed bi-axial compaction, which is useful for packaging solar and drag sails for space missions. During deployment, a sheet creased in this manner experiences three separate equilibrium configurations, each corresponding to a ring of faces opening away from the hub. LS-Dyna and Abaqus/Explicit simulations starting in an approximation of the folded configuration were able to capture the equilibrium configurations. Simulations in LS-Dyna utilizing BWC quadrilateral shell elements were best able to capture the force magnitudes

The momentless-crease force folded (MCFF) technique was developed. It utilizes pressure, line and vertex loads to fold a creased sheet into a tightly packaged configuration. Pressure loads apply follower forces, they are a replacement for rotational boundary conditions. Line and vertex loads keep creases straight, to avoid crumpling. Rotational boundary conditions were tested for the effectiveness on the benchmark problem; however the facets were over-constrained during folding, leading to significant twisting of the facets. At vertices which are over-constrained, removal of the surrounding elements reduces stress concentrations and the force required for folding. Deployment simulations in LS-Dyna starting from packaged configurations found using the MCFF approach qualitatively matched the simulations starting from an initial approximation of the folded state. In particular, the deployment force was zero at two of the three intermediate equilibrium configurations. The force peaks were also within 27% of the initially folded simulations. This validates the MCFF approach, compared to starting in an approximation of the folded configuration.

These results show that it is simpler to start from an approximation of the folded configuration than a configuration found through MCFF. However, if the folded state is not known, folding a creased sheet from a flat state via MCFF can provide a reasonable approximation of the packaged configuration.

Chapter 4

Dynamic Deployment of Tape Spring Booms

Ultralight deployable space structures often require booms for deployment, and these booms need to be lightweight with high packaging efficiency. Of particular interest are tape spring booms due to the simplicity of their design, potential low cost, and use in existing satellite missions [19, 32, 16].

Analytical models already exist for the unfolding of a tape spring with a single localized fold, and the uncoiling of a tape spring from around a hub $R_{hub} \approx R_i$ [45], refer to Sections 2.4.3 and 2.4.4 for details. These analytical approaches work well for simple cases. To capture more complex behavior such as friction and the interplay of tape springs with other components, finite element models have been developed in the present research.

To develop the numerical modeling approach for tape springs, including capturing the formation and rolling behavior of localized folds, the analytical models are compared against LS-Dyna FEA simulations in this chapter. In Section 4.1 the most suitable elements for modeling the dynamic unfolding of a tape spring are determined, while in Section 4.2 different damping techniques are applied to match experimentally observed energy absorbtion. Section 4.3 covers the simulation of dynamic uncoiling of a tape spring from around a spool, and is compared with a previous analytical model that contains no energy loss tuning factors.

4.1 Unfolding Dynamics of Tape Spring with a Single Fold

In 1999 Seffen & Pellegrino [45] developed two analytical models for the unfolding of tape springs with one end clamped and a single localized fold, as described in Section 2.4.3. One of these

L (mm)	505
R_t (mm)	14.5
t (mm)	0.1
$\alpha(^o)$	108
E (GPa)*	128.7
ν *	0.275

Table 4.1: Properties of tape springs tested by Seffen & Pellegrino [45], * indicates values derived from bending moment experiments.

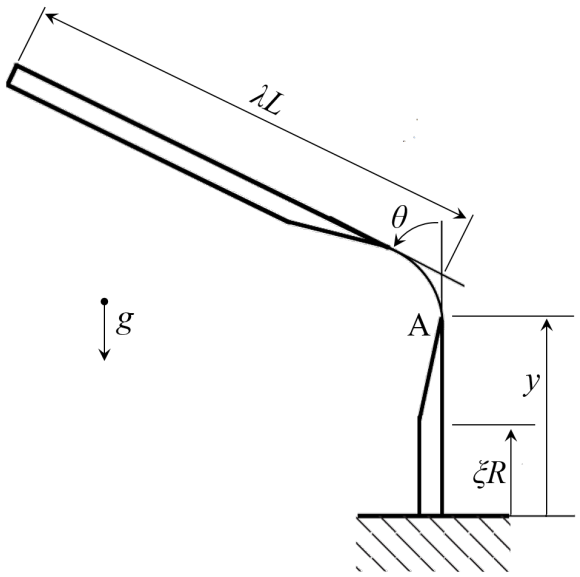

Figure 4.1: Schematic of a clamped tape spring with a single localized fold.

models was the impulse-momentum approach, which was found to work well with experimental data. As the tape deployed, the localized fold traveled down the tape spring until it reflected off the clamped end. Energy was dissipated at the clamped region each time the fold reflected off the boundary. The model was validated with physical experiments utilizing BeCu tape springs. The tape springs were made from Beryllium Copper and had the properties specified in Table 4.1. The clamped boundary condition was obtained by mounting one end in an epoxy base. The Young's modulus (E) and Poisson's ratio (ν) in Table 4.1 were back calculated from the bending moment information in [45], assuming isotropic behavior. The following FEA simulations use these properties when modeling the tape spring.

Figure 4.1 shows a schematic of the folded tape spring part way through deployment. Key deployment variables are λ and θ, where λ is the ratio of deployed length to total length, and θ the

deployed angle. y signifies the distance of the localized fold away from the clamped region, whilst the difference between y and ξR is the transition region length. g indicates the direction of gravity.

4.1.1 Computation of Folded Configuration

The structure was simulated in LS-Dyna, and the model consisted of a 520 mm long tape spring, with the bottom 15 mm subject to clamped boundary conditions. Two temporary cylinders 25 mm in diameter were located either side of the middle of the tape spring, where the localized bend will form. These cylinders aid in the folding process.

Four separate FEA models were created with identical boundary conditions but different shell element types. The element types tested were quadrilateral Belytschko-Tsay shell elements, quadrilateral S/R Hughes-Liu elements, C^0 triangular shell elements and fully integrated quadrilateral shell elements. The elements were sized at the default provided by the LS-Dyna PrePost automesher, at 2 mm. This gave 14 elements transversely across the tape spring. Figure 4.2 shows the Belytschko-Tsay quadrilateral mesh and the node sets used for applying the boundary conditions during folding and deployment.

To fold the tape spring, first displacement boundary conditions were applied in the x direction to the edge nodes, flattening the tape spring. After flattening, frictionless contact was applied between the tape spring and cylinders through the keyword `*AUTOMATIC_SURFACE_TO_SURFACE`. The flattening boundary conditions were released and the tip of the tape spring was displaced, wrapping the tape spring around a cylinder. Once a localized fold in the tape spring was formed, contact between the cylinders was removed and these cylinders ceased to be used in the rest of the simulation. Once the tape spring was fully folded, displacement boundary conditions were applied to all tape spring nodes to remove excess kinetic energy. Once this energy was removed, the tip was constrained in all translational degrees of freedom, and the tape spring allowed to reach an equilibrium folded state. A full description of the applied boundary and contact conditions is detailed in Table 4.2. Gravity was applied through the `*LOAD_BODY_Z` keyword, which applies a body force to the entire tape spring.

A schematic of the folding process is shown in Figure 4.3. The tip displacement during folding was carefully calculated to stop the tape spring from either stretching or buckling. The x, z path

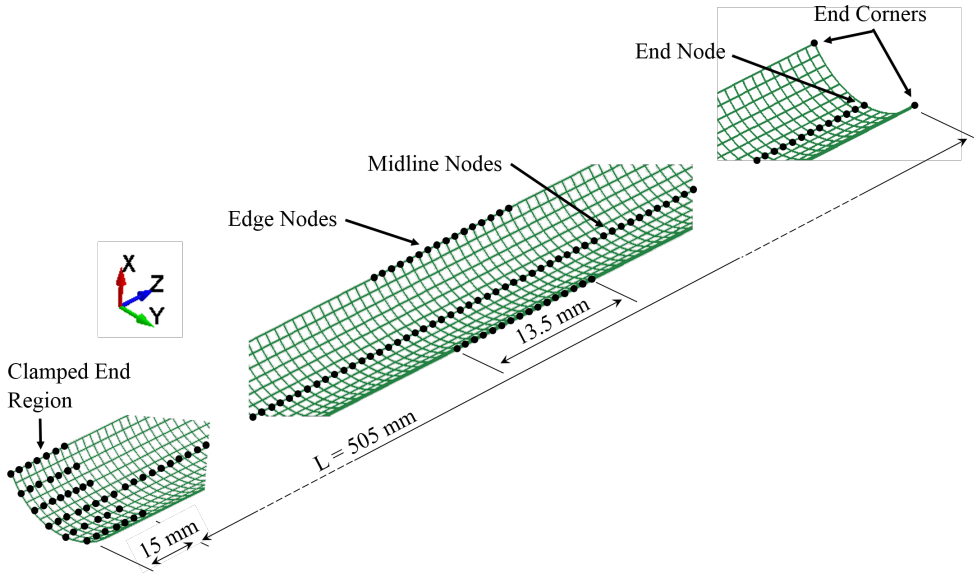

Figure 4.2: Regions of the tape spring to which boundary conditions are applied during the folding process.

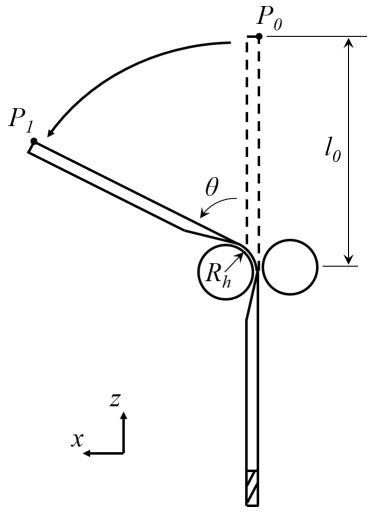

Figure 4.3: Schematic of the folding process. The tape spring is first flattened in the middle, then contact applied between the tape spring and the two cylinders of radius R_{hub}. Point P is displaced, wrapping the tape spring through angle θ around a cylinder.

Description	Time (s)	Node Set	Boundary Conditions Activated
Restrain out of plane displacement	0 - ∞	Midline Nodes	$u_y = 0$
Fix base to model clamped end condition	0 - ∞	Clamped End Nodes	$u_x = u_z = 0$
Constrain corners to minimize tape spring twisting motion	0 - ∞	End corners	$u_y = 0$
Restrain twisting of midline during folding	0 - 0.17	Midline nodes	$\theta_x = \theta_z = 0$
Edges are displaced to flatten tape-spring	0 - 0.04	Edge nodes	$u_x = 5.7$
Fix midline position as edges are flattened	0 - 0.06	Midline nodes	$u_x = u_z = 0$
End node displaced to fold tape spring around cylinders	0.06 - 0.18	End node	$u_x = f(t), u_z = g(t)$
Kinetic energy removed by constraining tape spring X & Y degrees of freedom	0.18 - 0.2	All nodes	$u_x = u_z = 0$
End node held in place	0.20 - 0.21	End node	$u_x = u_z = 0$

Table 4.2: Boundary conditions applied to the tape spring to obtain the folded configuration. $f_1(t), f_2(t), g_1(t), g_2(t)$ were calculated from Equation 4.2.

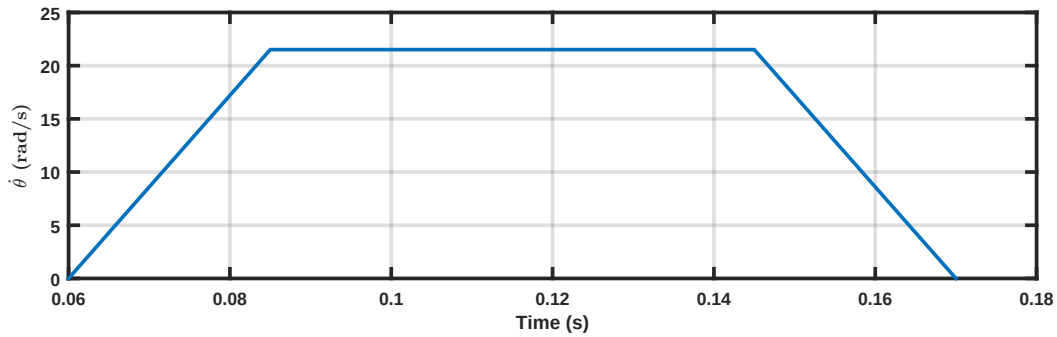

Figure 4.4: Time derivative profile of θ applied to give a smooth folding process. The area under the curve corresponds to $\theta = \frac{\pi}{2}$ radians.

the tip, point P, was constrained to follow during folding is

$$\begin{aligned} x =& x_0 + R_{hub}(1 - \cos\theta) + (l_0 - R_{hub}\theta)\sin\theta \\ z =& (z_0 - l_0) + R_{hub}\sin\theta + (l_0 - R_{hub}\theta)\cos\theta \end{aligned} \tag{4.1}$$

where x_0, z_0 are the initial coordinates of the end node at the tip, R_{hub} the cylinder radius the tape spring is wrapped around, θ the wrapped angle and l_0 the initial free length of tape spring beyond the cylinder, as defined in Figure 4.3. The $(l_0 - R_{hub}\theta)$ term corresponds to the free length of the tape spring that is not wrapped around the cylinder. The boundary condition displacement profile applied to the end node is therefore

$$\begin{aligned} u_x = x - x_0 =& R_{hub}(1 - \cos\theta) + (l_0 - R_{hub}\theta)\sin\theta \\ u_z = z - z_0 =& R_{hub}\sin\theta + (l_0 - R_{hub}\theta)\cos\theta - l_0 \end{aligned} \tag{4.2}$$

In the folding stage θ was applied smoothly according to the time dependent profile shown in Figure 4.4.

4.1.2 Unfolding Results

Snapshots of the unfolding results for simulations incorporating the Belytschko-Tsay quadrilateral and C^0 triangular shell elements are shown in Figures 4.6 and 4.7 respectively. The corresponding λ and θ responses for all simulations are shown in Figure 4.8. λ was found by measuring the distance from the top node to the edge of the localized fold, then adding half the fold arc length.

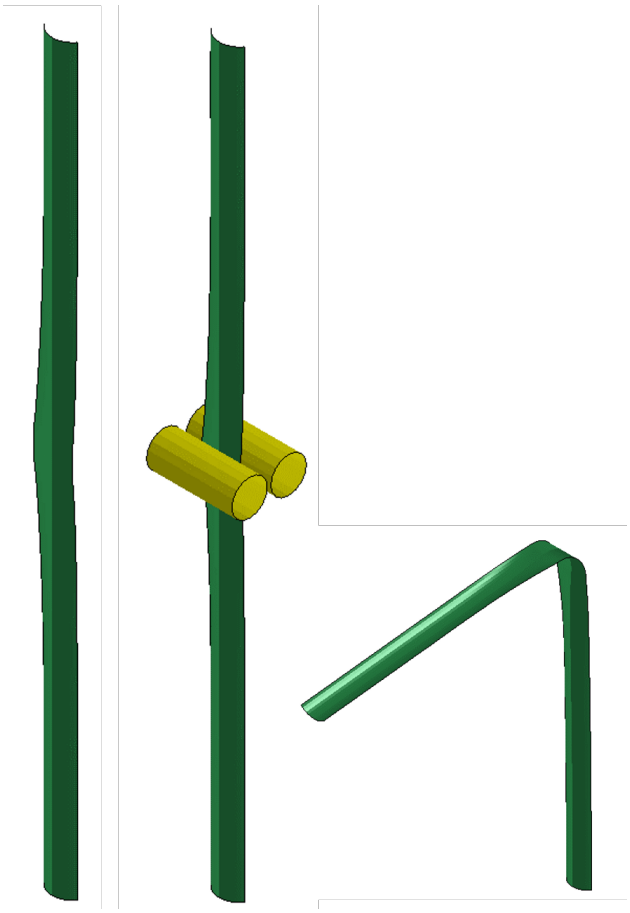

Figure 4.5: Isometric view of the folding process (a) Flattening tape spring, (b) Adding contact with folding cylinders to form localized fold, (c) Final folded configuration.

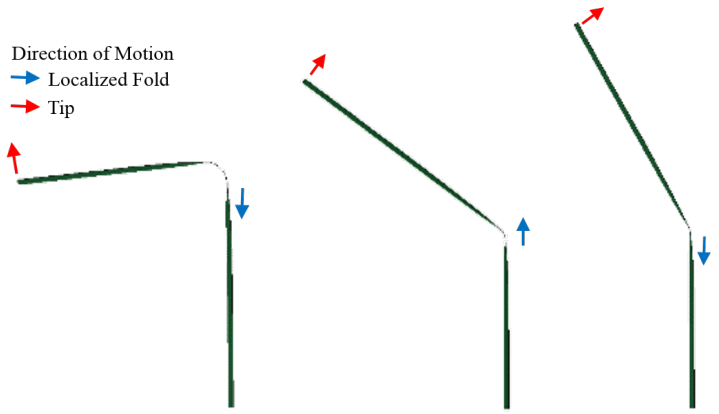

(a) 0.0 s (b) 0.09 s (c) 0.14 s

Figure 4.6: Snapshots during unfolding for a tape spring meshed with Belytschko-Tsay quadrilateral shell elements. The red and blue arrows correspond to the direction the tip and localized fold are moving at time of snapshot.

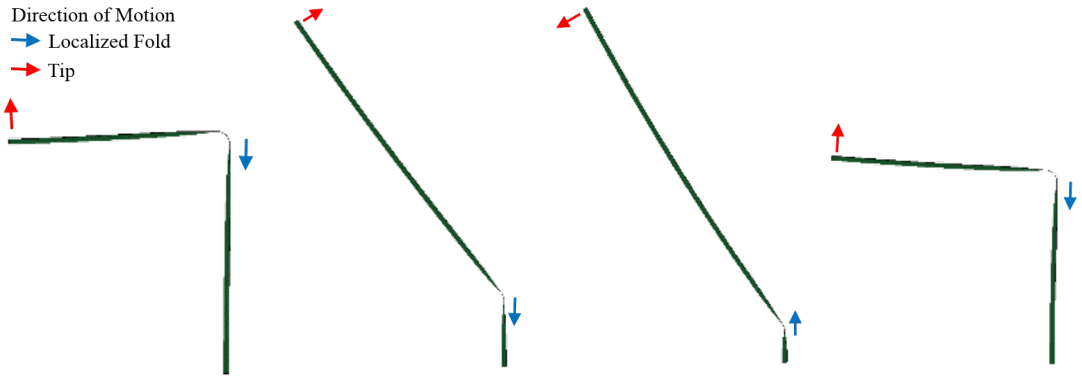

(a) 0.0 s (b) 0.09 s (c) 0.10 s (d) 0.11 s

(e) 0.19 s (f) 0.24 s (g) 0.30 s

Figure 4.7: Snapshots during tape spring deployment for a tape spring meshed with C^0 triangular shell elements. The red and blue arrows correspond to the direction the tip and localized fold are moving, respectively, at the time of the snapshot.

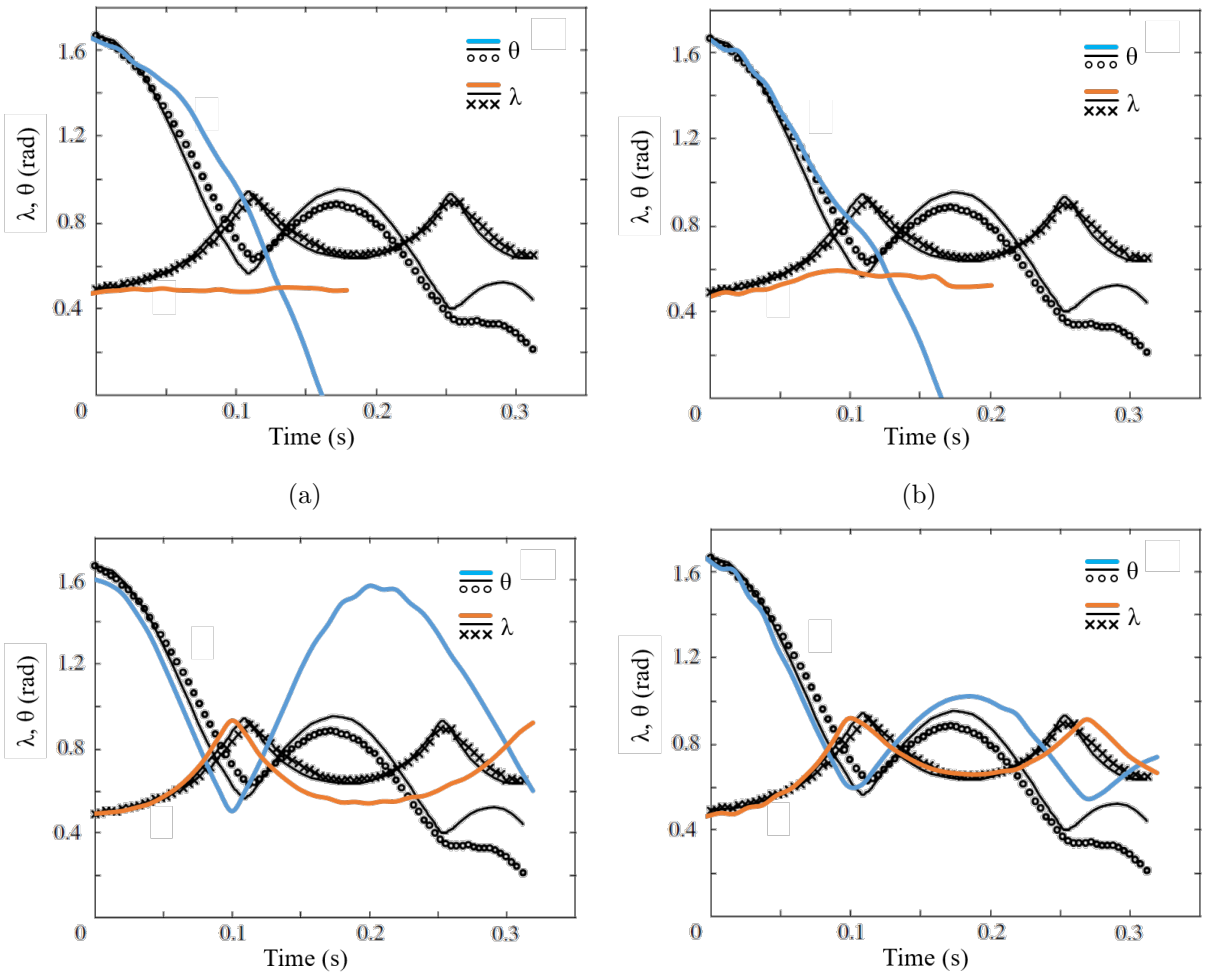

Figure 4.8: λ and θ results from simulation using (a) quadrilateral Belytschko-Tsay shells, (b) quadrilateral S/R Hughes-Liu shells, (c) C^0 triangular shell elements, and (d) fully integrated quadrilateral shell elements (Type -16). The black crosses and circles are the experimental data points and the solid black lines are from the analytical model.

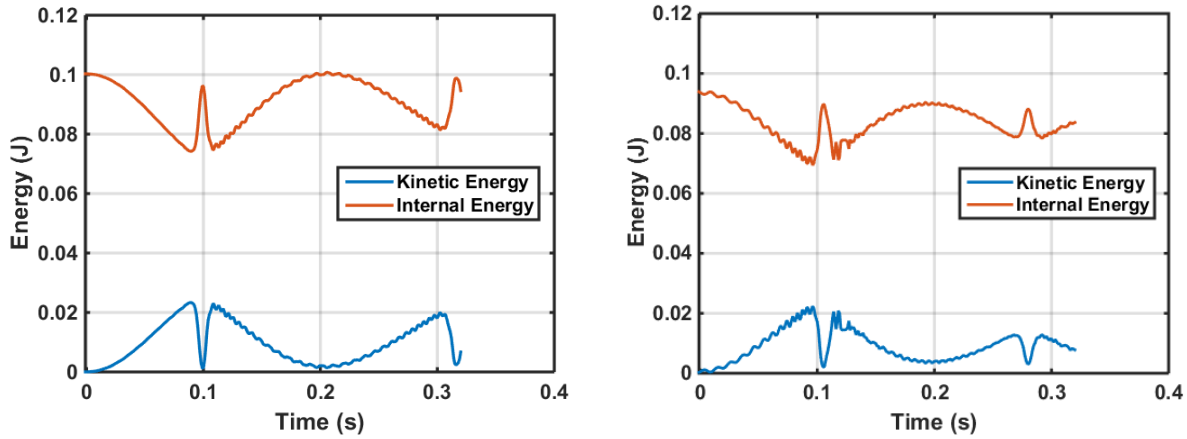

Figure 4.9: Kinetic and internal energy during unfolding for (a) C^0 triangular shell elements , and (b) fully integrated quadrilateral shell elements (Type -16).

For the Belytschko-Tsay simulation, the folded region did not propagate down the tape spring as the free end rotated, but remained locked in position providing a flat λ profile. In the simulations utilizing S/R Hughes-Liu shells, the localized fold traveled 60 mm down the tape spring before stopping.

The localized fold in the tape spring modeled with C^0 triangular elements traveled down the tape spring, and reflected off the clamped end at 0.11 s. However, unlike the experiment no energy was dissipated during the reflection and the system behaved like a perfect spring, with the localized fold traveling back up the tape spring at the same speed as when it first came into contact with the clamped end. At 0.2 s the tape spring almost returned to its original configuration, with $\lambda = 0.55$ and $\theta = 1.57$ rad, compared to $\lambda = 0.49$ and $\theta = 1.58$ rad at the start. The internal and kinetic energy during unfolding is shown in Figure 4.9(a).

For the simulations incorporating fully integrated quadrilateral shells (Type -16), the localized fold also travels down the tape spring and reflects off the clamped end. However, immediately after the reflection the boom buckles, as indicated in Figure 4.10(b). The boom snaps back into an unbuckled state 0.01 s later, however some of the kinetic energy has been converted into vibration and torsional motion. The localized fold therefore travels up the tape spring at a lower velocity than before the reflection. Figure 4.9(b) shows the internal and kinetic energy for the fully integrated quadrilateral shells case. It is unknown if this was the effect observed in the initial experiments, or

if energy was dissipated through a different mechanism.

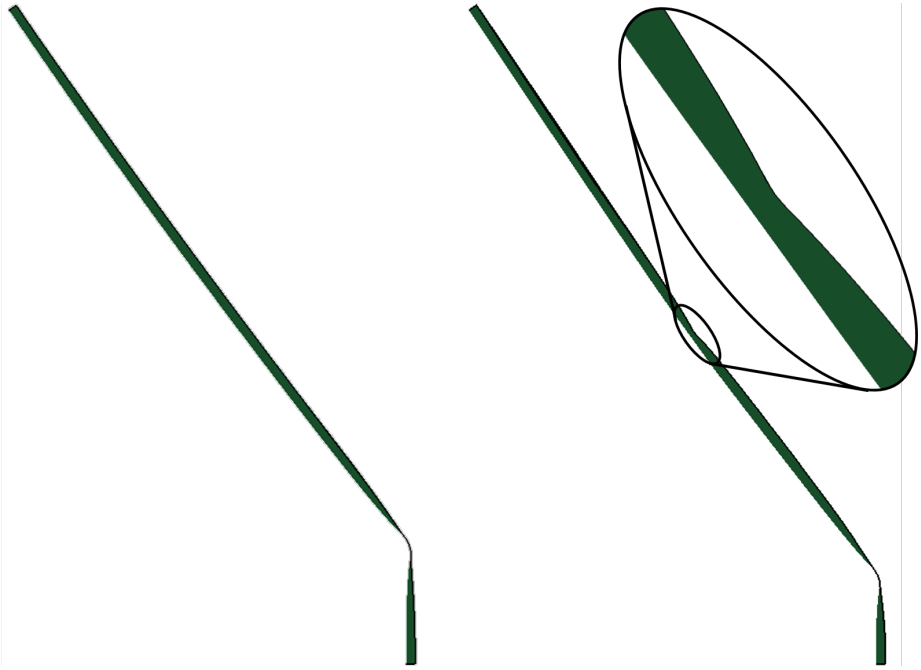

(a) (b)

Figure 4.10: The tape spring configuration immediately after the localized fold has reflected off the base for tape springs meshed with (a) C^0 triangular shell elements , and (b) fully integrated quadrilateral shell elements (Type -16). A close up of the region where the tape spring has buckled when meshed with quadrilateral shell elements is also shown.

4.2 Effect of Energy Absorption on Unfolding Dynamics

In the experiments energy appeared to be dissipated each time the localized fold reflected off the clamped end. To model this, two energy dissipation techniques were added to the fully integrated quadrilateral and C^0 triangular shell element simulations. The first was incorporating non-reflecting boundary conditions, and the second was to apply mass nodal damping.

4.2.1 Non-Reflecting Boundary Conditions

Mallikarachchi & Pellegrino [24, 26] modeled the behavior of similar composite tape spring booms in Abaqus/Explicit. There they used infinite elements to stop the clamped end from reflecting stress waves back into the system. Infinite elements are designed to model the far-field region and

act as remote dashpots that provide distributed damping along the boundary. In this simulation, solid elements were required as an interface between the composite boom and the infinite elements.

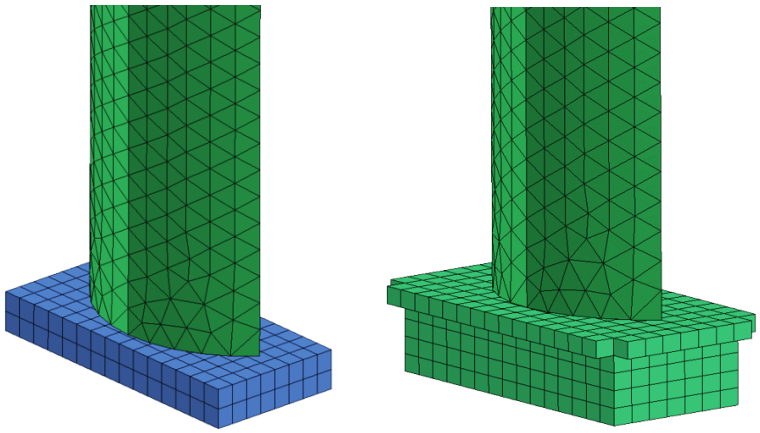

(a) (b)

Figure 4.11: (a) Non-reflecting boundary conditions applied to bottom surface only. (b) Non-reflecting boundary conditions applied to bottom surface, and sides of the solid element layer nearest the tape spring.

LS-Dyna models far-field effects by providing non-reflective boundary conditions which can be applied to a single face on given solid elements. In practice, these boundary conditions act similarly to infinite elements in Abaqus/Explicit. Two different LS-Dyna simulations were performed with non-reflecting boundary conditions. Figure 4.11(a) shows reflective boundary conditions applied to the bottom only (RB1), and applied to both bottom and sides in Figure 4.11(b) (RB2). Figure 4.12 shows the effect of these boundary conditions. While energy is lost for the C^0 case, and the second θ peak is lower, it is still 50% higher than either the analytical model or the experimental results. Non-reflecting boundary conditions have very little effect on the behavior of the tape spring meshed with fully integrated quadrilateral shell elements.

4.2.2 Viscous Damping

An alternative energy dissipation method used by previous work [24, 26] utilizes viscous damping to the system. While the damping mechanism itself is non-physical, viscosity can be tuned to remove from the simulation the energy that in reality is lost at the root of the boom. Seffen & Pellegrino [45] also added viscous damping terms of $8 \times 10^{-3}\dot{\lambda}$ and $8 \times 10^{-3}\dot{\theta}$ to the energy formulation equations to gradually remove energy from the system.

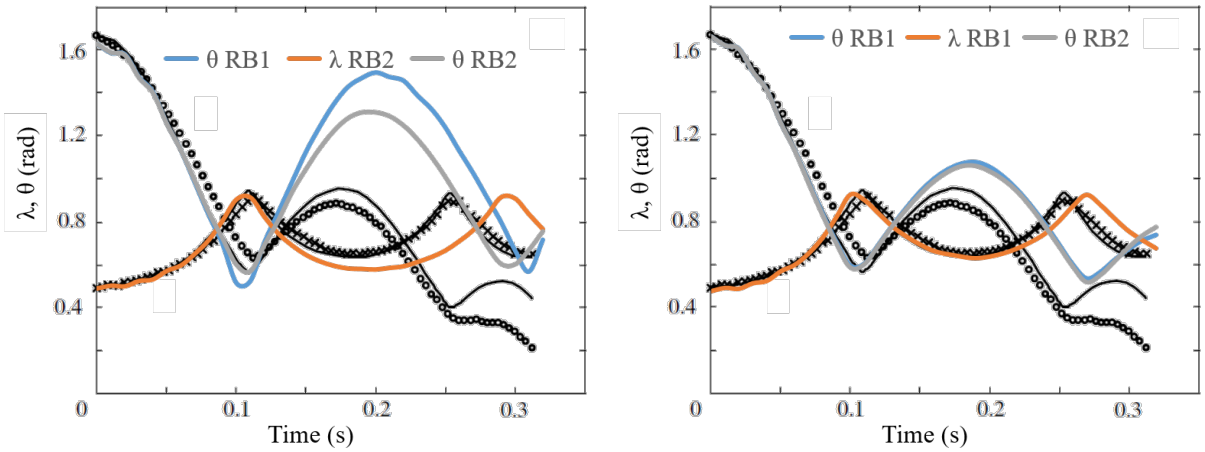

(a) (b)

Figure 4.12: λ and θ results from implementing non-reflective boundary conditions for simulations using (a) C^0 triangular shell elements, and (b) fully integrated quadrilateral shell elements, (Type -16). RB1 and RB2 correspond to setups in Figure 4.11(a) and 4.11(b).

Viscous / mass nodal damping was tuned so that for the C^0 mesh the peak θ value following the first reflection matched the experimental data to within 1%, as shown in Figure 4.13(a). Applying viscous damping has two effects. First, it removes kinetic energy from the system and so reduces the second θ peak value. The second effect is to increase the time it takes for the localized fold to travel along the tape spring. The localized fold reaches the clamped region at 0.115 s, compared with 0.1 s in the undamped simulation and 0.11 s experimentally. Potential future work could involve applying viscous damping to the tape spring only when the localized fold is in the process of being reflected.

4.3 Coiling and Dynamic Uncoiling of Tape Springs

In the previous section, the focus has been on comparing tape spring FEA unfolding models against experimental data, and applying tuning factors to match the energy loss. This section focuses on a direct comparison between the FEA and analytical models for a scenario that contains no energy dissipation mechanisms.

In the following sections, the predictions from the equations for the uncoiling of a tape spring in vacuum are compared against matching LS-Dyna models. The boom parameters used, listed in Table 4.3, match those Seffen & Pellegrino used in their original experiments. Section 4.3.1

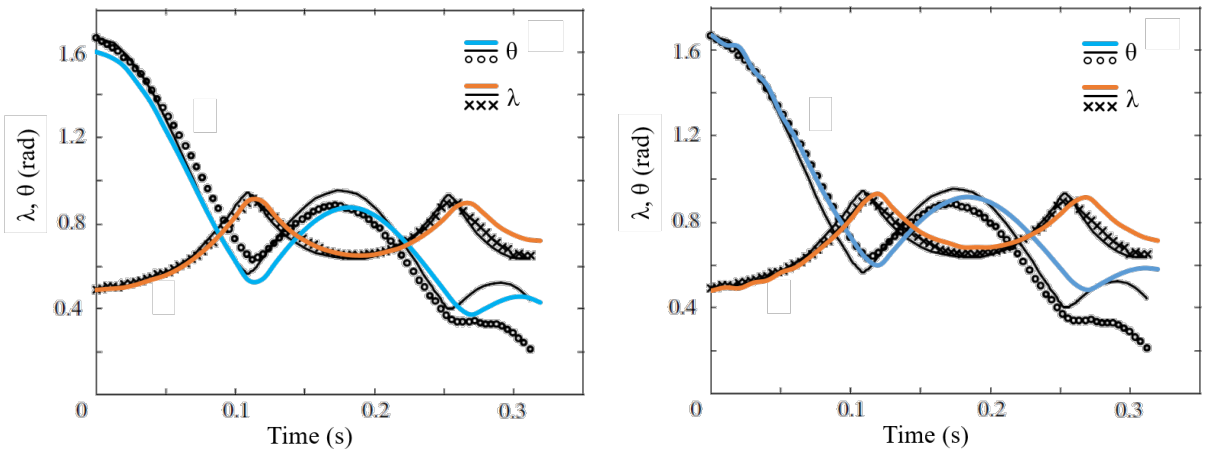

(a) (b)

Figure 4.13: Viscous pressure of 0.75 s^{-1} applied to tape spring surface during deployment to capture energy absorption. λ and θ results from simulation using (a) C^0 triangular shell elements, and (b) fully integrated quadrilateral shell elements (Type -16). The black crosses and circles are the experimental data points and the solid black lines are from the analytical model.

L (mm)	500
R_t (mm)	15.1
t (mm)	0.1
$\alpha(^o)$	135
E (GPa)*	133
ν *	0.295
ρ (kg/m^3)	3200

Table 4.3: Properties of tape spring tested in uncoiling experiments [45], * indicates values derived from bending moment experiments.

covers the coiling of the tape spring around a hub of $R_{hub} \approx R_i$ in LS-Dyna. Section 4.3.2 covers the uncoiling of the same tape spring and compares the results for equal-sense and opposite-sense bending.

4.3.1 Coiling

The LS-Dyna model consists of four components: the tape spring, as per Figure 4.14(a), a central hub comprised of two rigid cylinders, and a spool, shown in Figure 4.14(b). In the initial state the tape spring intersects the spool. To initiate the process, the edge nodes are displaced in the x direction whilst the midline is fixed in place. This flattens the tape spring. Contact is then provided between the tape spring and the rigid blue cylinders which no longer intersect the tape

spring.

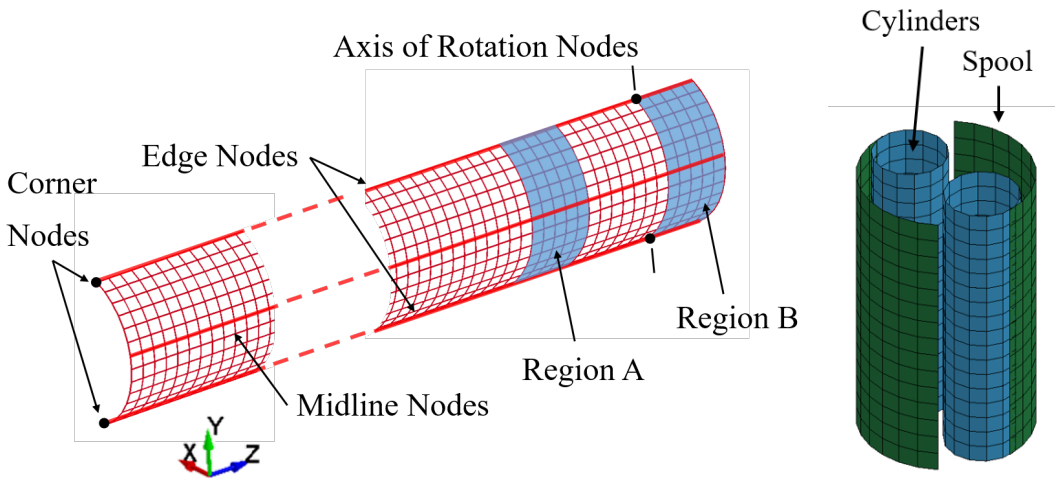

(a) (b)

Figure 4.14: Isometric views of (a) tape spring, including node sets and regions where boundary conditions are applied, and (b) the central hub. After flattening, the axis of rotation nodes are coincident to the green hub axis. The tape spring slots between the blue cylinders and the whole hub is rotated so that it wraps around the green arcs.

Once flattened, the nodes labeled 'axis of rotation nodes' in Figure 4.14(a) are fixed in the x and z directions. These nodes are now in the direct center of the green cylindrical section that forms the spool. The spool and two cylinders are now rotated through 28.4 radians, or 4.5 revolutions, about the spool's central y axis. During this step the corners of the free end of the tape spring are constrained to only move tangentially to the spool. After 0.96 s the tape spring coiling process is complete.

From 0.96 s to 1.16 s Region A is fully constrained in the x and z directions, while the boundary conditions on the rotation axis nodes are removed. Contact between the tape spring and the cylinders is also removed. This releases the tape spring end inside the spool as depicted in Figure 4.15(d). The purpose of this step is to reduce the curvature of the tape spring where it enters the spool. Finally, Region B, corresponding to the section of tape inside the spool is fully constrained in the X and Z directions. This sets up the tape spring for the uncoiling simulation in the next section. A complete description of the boundary conditions applied to produce the coiled configuration can be found in Table 4.4.

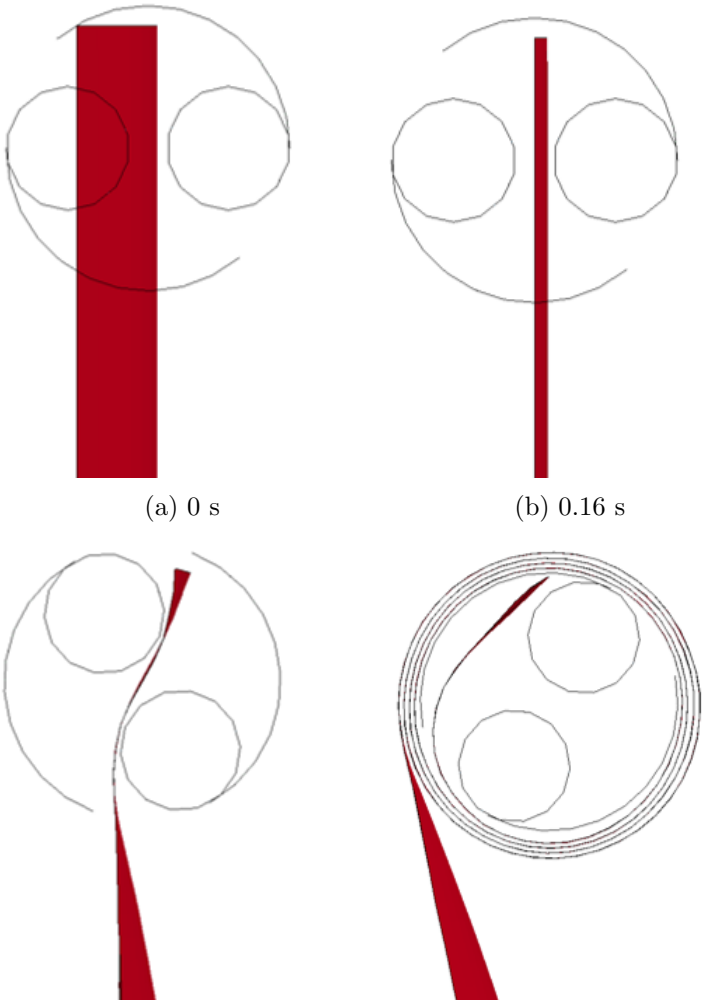

(a) 0 s (b) 0.16 s

(c) 0.28 s. (d) 1.16 s

Figure 4.15: Key stages in the coiling simulation. (a) Initial configuration, (b) Tape spring flattened & contact with cylinders applied, (c) spool and cylinders rotated 28.4 radians, contact between tape spring and spool applied, and (d) end of coiling simulation.

Description	Time (s)	Node Set	Boundary Condition Activated
Fix midline position to constrain out-of-plane motion	0 - ∞	Midline	$u_y = 0$
Fix spools	0 - 0.16	Rigid bodies	$\theta_y = 0$
Edges are displaced to flatten tape-spring	0 - 0.16	Edge Nodes	$u_x = -8.321$ mm
Fix midline position as edges are flattened	0 - 0.16	Midline	$u_x = u_z = 0$
Contact applied between cylinders and tape spring	0.16 - 0.96	All nodes	
Contact applied between spool and tape spring	0.3 - ∞	All nodes	
Rotate spool	0.16 - 0.96	Rigid bodies	$\theta_y = -22.8$ rad
Fix tape spring nodes at the center of the spool, so tape rotates about these nodes during coiling	0.16 - 0.96	Rotation axis nodes	$u_x = u_z = 0$
Constrain tape-spring free end to move tangent to spool during coiling	0.16 - 1.16	Free end corners	$U_\xi = 0$
Fix spools	0.96 - ∞	Rigid bodies	$\theta_y = 0$
Constrain node displacement to maintain coiled state as axis nodes are released	0.96 - 1.16	Regions A & B	$u_x = u_z = 0$
Clamp hub end nodes as tape-spring dynamically uncoils	1.16 - ∞	Region B	$u_x = u_y = 0$

Table 4.4: Boundary conditions applied to the tape spring to obtain a coiled configuration.

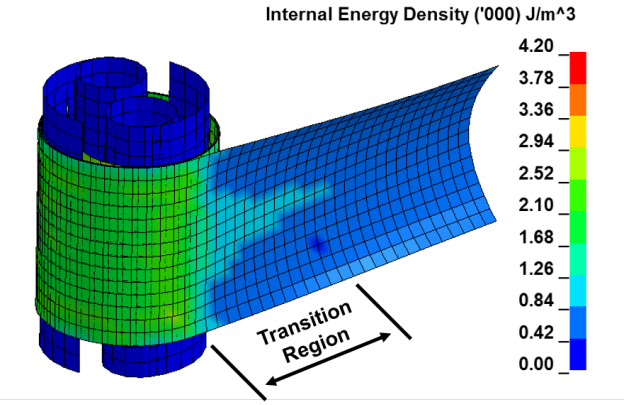

Figure 4.16: Energy density in the tape spring at the start of the uncoiling simulation.

4.3.2 Dynamic Uncoiling

The equations governing the uncoiling dynamics, detailed in Section 2.4.4, Equation 2.21 provide a closed form solution for $\dot{\gamma}$ as a function of γ, γ_0, and λ . These were used to generate a closed function for $\lambda(t)$, assuming the tape was fully coiled around the spool, i.e., $\lambda_0 = 0$. However, this assumption neglects the transition region in between the straight tape spring region where the cross-section is undeformed, and the region coiled around the spool which has a transverse curvature of $\kappa = 0$, as shown in Figure 4.16.

If $\lambda_0 = 0$, then the transition region has zero length. As λ increases the transition region length will also increase, until it reaches a constant length at $\lambda \approx \lambda_{crit}$. Therefore, if $\lambda_0 < \lambda_{crit}$ not all the stored strain energy will be converted into kinetic energy, a fraction will remain in the transition region, and therefore the analytical equation will underestimate the deployment speed. To avoid complications from this effect, the uncoiling simulations start with a non-zero λ_0. For the case studied here it was observed that $\lambda_{crit} \approx 0.05$.

An expression for $\dot{\lambda}$ that includes a non-zero λ_0 term can be derived by combining Equations 2.20 and 2.21 to give

$$(\frac{-\dot{\lambda}L}{R_{hub}})^2 = \frac{6\mu R_t R_{hub}\alpha}{\rho} \frac{(1-\lambda_0)\frac{L}{R_{hub}} - (1-\lambda)\frac{L}{R_{hub}}}{(L - R_{hub}((1-\lambda)\frac{L}{R_{hub}}))^3} \tag{4.3}$$

This can then be simplified to

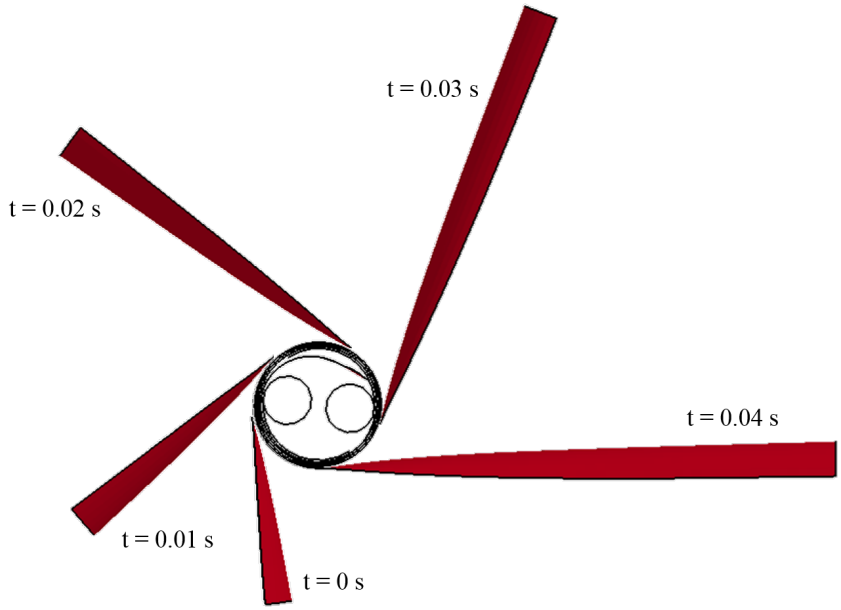

Figure 4.17: Snapshots of the uncoiling of tape spring wrapped in opposite sense, meshed with fully integrated LS-Dyna (Type -16), quadrilateral shell elements from around a fixed spool. t corresponds to the time from the start of deployment.

$$\dot{\lambda} = \frac{R_{hub}}{L}\sqrt{\frac{6\mu R_t \alpha}{\rho L^2}\frac{\lambda - \lambda_0}{\lambda^3}} \tag{4.4}$$

where for an isotropic material the energy areal density in the localized fold is

$$\mu = \frac{D(1 \pm \nu)}{R_t^2} \tag{4.5}$$

where $+$ corresponds to opposite-sense curvature, and $-$ to equal-sense curvature.

For each of the following LS-Dyna uncoiling simulations, the initial λ_0 was measured and inputted into Equation 4.4. MATLAB's ODE solver, 'ode45', was then used to calculate the resulting λ vs time profile for comparison.

Figure 4.17 shows the deployment of the tape spring over time. Figures 4.18(a) and 4.18(b) compare the numerical and analytical models. After 0.4 s of deployment, the analytical and numerical models match to within 1.2% and 0.9% for booms initially coiled in equal-sense and opposite-sense respectively. The noise in the numerical simulations correspond to vibrations present in the coiled

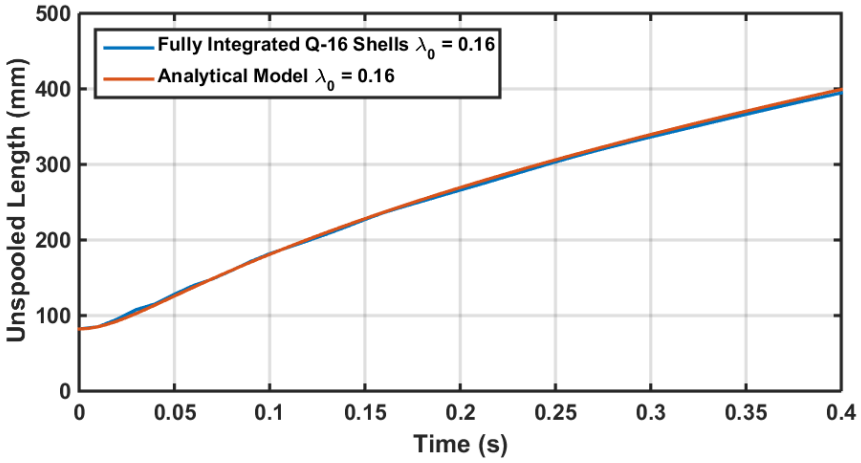

(a)

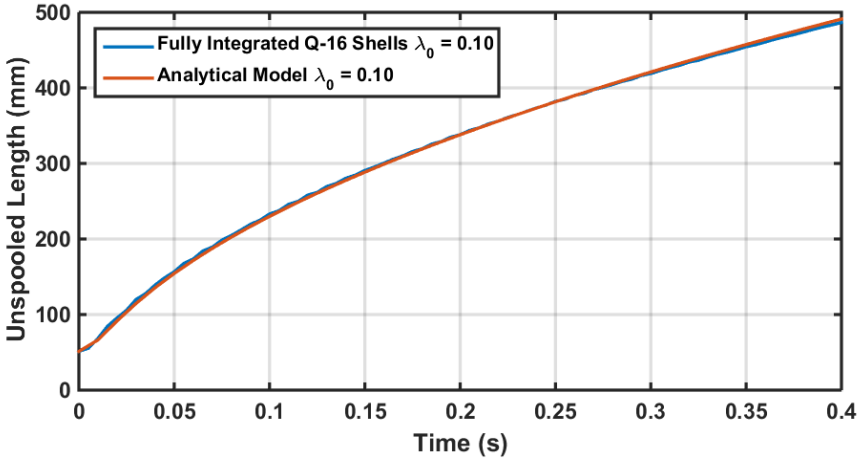

(b)

Figure 4.18: Comparison of the analytical model and the numerical model, utilizing fully integrated quadrilateral shell elements when deploying from an (a) equal-sense, and (b) opposite-sense coiled configuration.

tape spring that were not fully damped out at the end of the previous coiling step.

4.4 Discussion

Modeling with high accuracy the folding, deployment and uncoiling behavior of tape springs in LS-Dyna is achievable, with several caveats. The tape springs meshed with the reduced integration quadrilateral shell elements did not capture the rolling of localized folds along a tape spring as it deploys. In these simulations the fold remained fixed in place. The C^0 triangular and fully integrated quadrilateral shell elements were best able to capture this behavior, and when coupled to mass nodal (viscous) damping as an energy dissipation technique, was able to accurately match both experimental results and the analytical model.

The tape spring numerical model is also applicable to the dynamic uncoiling from around a hub of $R_{hub} \approx R_i$, with the analytical and numerical models matching to within 1.2%.

These results provide confidence that the tape spring numerical models accurately reflect reality, and provide a valid starting point for the simulations in the following chapter, where $R_{hub} \neq R_t$.

Chapter 5

Coiling of Tape Springs on Large Hubs

In this chapter a simple energy-based prediction of the formation of localized bends when wrapping a tape spring to a given radius is developed. The bifurcation of the localized bends, and the corresponding forces and locations are accurately captured by FEA methods and an analysis of the force required to fully wrap a steel tape spring around hubs of radii $0.4R_i < R_{hub} < 5.25R_i$ is carried out, and a linear trend is observed for $R_{hub} > 3.25R_i$. The numerical analysis is extended to ultra-light carbon fiber composite tape springs, with a focus on the effect of manufacturing imperfections on the predicted wrapping forces.

5.1 Formulation of Localized Bends

As noted in Section 2.4.2, the bending energy in a tape spring can be calculated from [8, 45]

$$U_{bending} = \frac{D\alpha R_t \theta R_i}{2}\left(\frac{1}{R_t^2} + \frac{2\nu}{R_t R_i} + \frac{1}{R_i^2}\right) \tag{5.1}$$

where the flexural bending stiffness $D = \frac{Et^3}{12(1-\nu^2)}$. R_i is the final longitudinal bend radius and R_t is the initial transverse radius of the tape spring. For an isotropic material, the lowest energy state occurs when $R_i = R_t$. The analysis below expands this work to cover tape springs that are wrapped or coiled around a hub of radius $R_{hub} \geq R_i$.

Consider a folded tape spring that is being wrapped around a hub of radius $R_{hub} > R_i$ by pulling one end so that the tape spring is forced to conform to the hub, as shown in Figure 5.1(a). The tape spring starts with a single fold with subtended angle γ and localized bend radius R_i. As

the end of the tape spring is displaced by distance d, the length of the tape spring covering the subtended arc angle γ of the hub decreases.

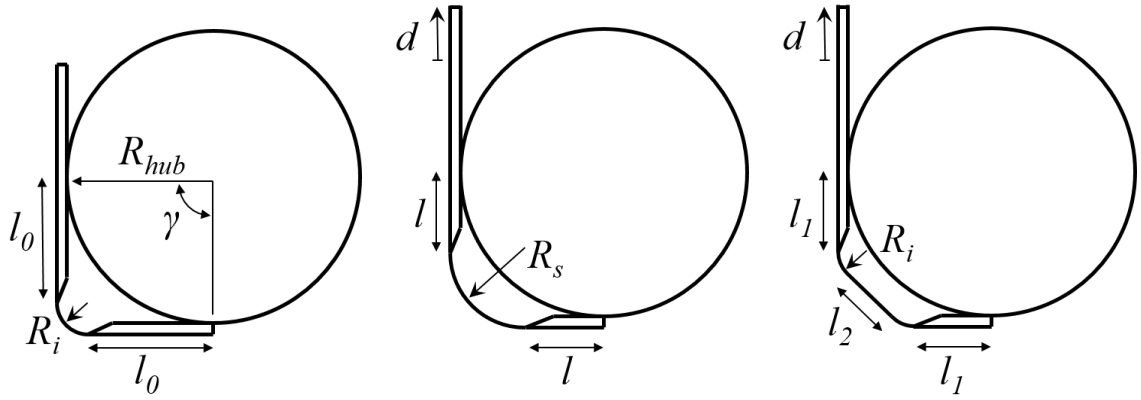

(a) Initial configuration (b) Case 1 (c) Case 2

Figure 5.1: Schematic of a tape spring folded around a cylindrical hub of radius R_h. (a) Initial configuration, including localized bend radius of R_i. When displacement d applied to tape spring end, either (b) the localized bend radius increases or (c) the localized fold bifurcates into two folds.

This can result in two separate scenarios. In the first, the localized bend increases in radius, as shown in Figure 5.1(b). In the second, the localized bend bifurcates into two, forming two folds of radius R_i, connected by a straight, flattened section, depicted in Figure 5.1(c). The radius R_s and the length of straight section joining the two localized folds in case 2, l_2, can be determined geometrically as a function of d

$$R_s = \frac{R_i(\gamma - 2\tan(\frac{\gamma}{2})) - d}{(\gamma - 2\tan(\frac{\gamma}{2}))} \tag{5.2}$$

$$\begin{aligned} l_1 =& \frac{2R_i\tan(\frac{\gamma}{2}) - R_i\gamma}{1 - \frac{1}{\cos(\frac{\gamma}{2})}} \\ l_2 =& (R_{hub} - R_i)\tan(\frac{\gamma}{2}) - \frac{l_1}{\cos(\frac{\gamma}{2})} \end{aligned} \tag{5.3}$$

In actuality the straight section of tape spring between the two localized folds will not be perfectly flat, but this is neglected in the analysis. It is also assumed that changes in the stretching strain energy are negligible, and that the fold radius of curvature in case 2 is exactly R_i. The bending strain energy of the two cases can be calculated for each value of d: for case 1 it is

$$U_1 = \frac{DR_s\gamma R_i\alpha}{2}\left(\frac{1}{R_s^2} + \frac{2\nu}{R_sR_i} + \frac{1}{R_i^2}\right) \tag{5.4}$$

and for case 2 it is

$$U_2 = D\gamma\alpha(1+\nu) + \frac{D\alpha}{2}\frac{l_2}{R_i} \tag{5.5}$$

In Equation 5.5 the first term is from the two localized folds each with radius R_i and subtended angle $\frac{\gamma}{2}$. The second term is from the flattened section of tape spring between the folds, of length l_2.

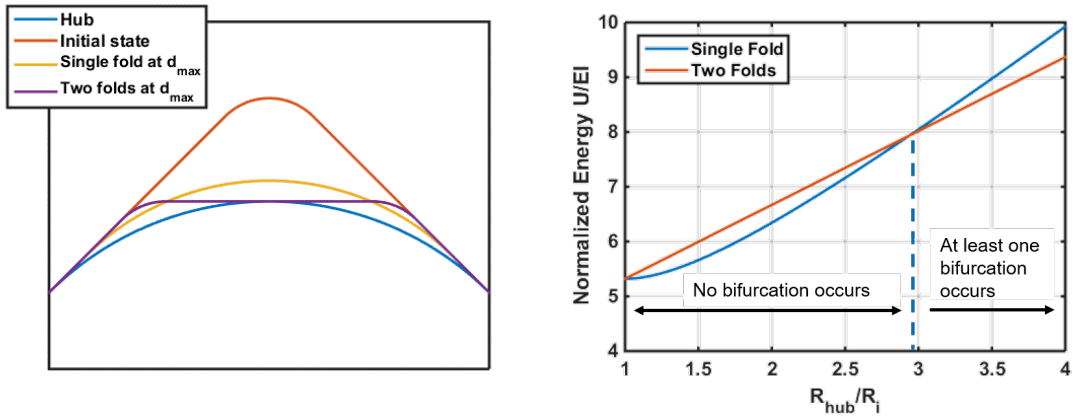

(a) (b)

Figure 5.2: (a) Case 1 and 2 superimposed for $\gamma = \frac{\pi}{2}$ at $d = d_{max}$, where the straight, flattened region is in contact with the hub. (b) The energy present in a tape spring at d_{max} and $\gamma = \frac{\pi}{2}$ for case 1 and 2.

Figure 5.2(a) shows a schematic for both cases when $\gamma = \frac{\pi}{2}$. The blue line corresponds to the hub and the red line to the starting configuration of the tape spring. The yellow and purple lines correspond to case 1 and case 2 respectively, when the tape spring is displaced by d_{max}. d_{max} is defined as the displacement of the tape spring that brings the flattened region, between the two localized folds, in case 2, fully into contact with the hub. The energy in both cases at d_{max} is plotted against $\frac{R_{hub}}{R_i}$ in Figure 5.2(b). There are three features in this plot of particular note. First, at $\frac{R_{hub}}{R_i} = 1$, the two cases contain equal amounts of energy as expected, because in case 2 the straight region connecting the two folds would be infinitesimally long. For $1 < \frac{R_{hub}}{R_i} < 3$ the lowest energy state is for a single fold. However, for $\frac{R_{hub}}{R_i} > 3$ the lowest energy state is for two localized folds of radius R_i connected by a straight, flattened region.

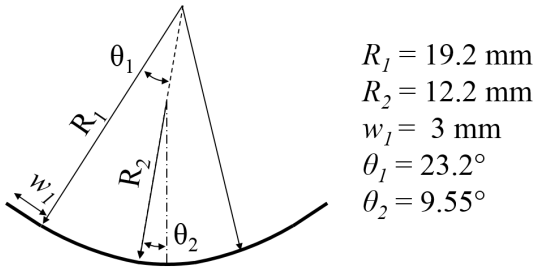

Figure 5.3: Piece-wise curvilinear cross-section of tape spring.

This result implies for that for $\gamma = \frac{\pi}{2}$, if $\frac{R_{hub}}{R_i} > 3$ then as d increases the localized bend radius will first increase in radius and then bifurcate into two folds before d_{max} is reached.

5.2 Opposite Sense Wrapping Experiment with $R_{hub} = 4.125R_i$

The bifurcation of tape spring hinges wrapped around hubs of radii $R_{hub} >> R_i$ was investigated in a wrapping experiment of an isotropic tape spring folded around a hub of radius $R_{hub} = 4.125R_i$.

5.2.1 Tape Spring Properties

The tape spring tested was a Craftsman 9-39530 E.Z.change locking tape replacement tape-measure sold by Sears Roebuck and Co., with Poisson's ratio $\nu = 0.3$, Young's modulus $E = 210$ GPa, and density of 8050 kg/m^3. The tape spring cross-section is piece-wise curvilinear, as depicted in Figure 5.3.

To find the minimum energy bend radius for a tape spring with a curvilinear cross-section, Equation 5.1 can be modified to include an arbitrary number of curved and flat components in the cross section. The more general form of the equation is

$$U_{tot} = \frac{DR_i\theta}{2}\left[\sum_{j=1}^{n} R_j\alpha_j\left(\frac{1}{R_j^2} \pm \frac{2\nu}{R_jR_i} + \frac{1}{R_i^2}\right) + \sum_{k=1}^{m} w_k\left(\frac{1}{R_i^2}\right)\right] \tag{5.6}$$

where R_j and α_j are the radius and subtended angle of each curved section, and w_k the length of each straight section. The minimum energy bend radius is then found by first differentiating with

respect to the bend radius R_i

$$\frac{dU_{tot}}{dR_i} = \frac{D\theta}{2}\left[\sum_{j=1}^{n}\left(\frac{\alpha_j}{R_j} - \frac{R_j\alpha_j}{R_i^2}\right) - \sum_{k=1}^{m}\left(\frac{w_k}{R_i^2}\right)\right] \tag{5.7}$$

Setting the derivative equal to zero, and solving for R_i, gives the minimum energy bend radius

$$R_i = \sqrt{\frac{\sum_{k=1}^{m} w_k + \sum_{j=1}^{n} R_j\alpha_j}{\sum_{j=1}^{n}\frac{\alpha_j}{R_j}}} \tag{5.8}$$

Using the cross-sectional properties from Figure 5.3, $R_i = 19.2$ mm for the tape spring used in the wrapping experiment.

5.2.2 Experimental Setup

The experimental setup is shown in Figure 5.4. It consists of a tape spring bent around a steel hub of diameter 165 mm. One end of the tape spring is bolted with $\frac{1}{4} - 20$ bolts to the hub. The tape spring was folded around the hub by creating two localized folds, and the non-clamped end attached to the loading beam of an Instron tensile testing machine. The hub was attached to a wood mounting plate, which in turn was bolted to the base of the Instron machine. A white background was placed behind the tape spring to provide a good background for photography.

5.2.3 Measuring the Friction Coefficient

Before performing the wrapping experiment, it was important to measure the kinetic friction coefficient between the tape spring and the hub. To do this a 3 mm wide and 500 mm long strip was cut from along the edge of the tape spring. As Figure 5.3 shows, this strip had zero transverse curvature, and thus could be wrapped around the hub without the formation of localized bends. The strip was wrapped around the hub once, and a mass M = 250 grams attached to one end, as shown in Figure 5.5(a). The other end of the strip was clamped to the loading beam of the Instron tensile testing machine. The experiment was displacement controlled at a rate of 22 mm/min, and carried out nine times on the same strip.

Figure 5.4: Experimental setup for wrapping a tape spring around a hub of radius $R_{hub} = 4.125R_i$.

The coefficient of friction was then calculated from the capstan equation [31]

$$\begin{aligned} T_{load} =& T_{hold} e^{\mu\gamma} \\ \mu =& \frac{\ln(\frac{T_{load}}{T_{hold}})}{\gamma} \end{aligned} \tag{5.9}$$

where $T_{load} = F$, T_{hold} =Mg = 2.45 N, and $\gamma = 2\pi$ rad is the total swept angle of the strip around the hub. Figure 5.5(b) shows a significant variation, ranging from coefficients between 0.15 to 0.2, with a mean of $\mu = 0.18$ and standard deviation of ± 0.012.

There are several potential causes for this variation. Firstly, this may be due to the static coefficient of friction that is higher than the kinematic coefficient, causing stick-slip behavior. Secondly, the hub is made from steel < 1 mm thick and the cross-section of the hub may not have remained perfectly circular, leading to loss of contact between part of the tape spring and the hub. Finally, as the strip was looped around the hub 360^o, the strip edges slid against each other during the experiment, potentially increasing the noise in the force output.

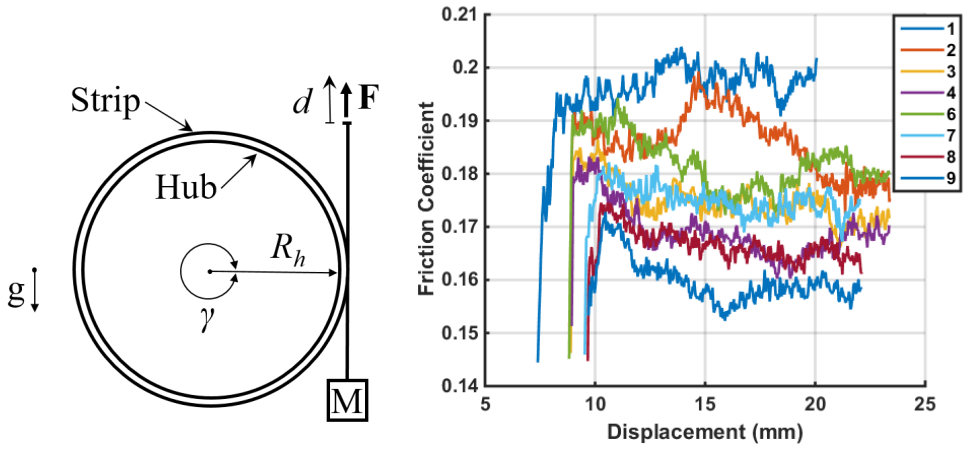

(a) (b)

Figure 5.5: (a) Schematic of experimental setup for measuring the coefficient of friction between the hub and the tape spring. (b) Kinetic friction coefficients (μ) obtained from nine experimental runs.

5.2.4 Wrapping Experimental Results

The force profile measured in the wrapping experiment is shown in Figure 5.6, with snapshots of key configurations in Figure 5.7. Once the straight section between the two localized folds came into contact with the hub, the left localized fold increased in radius, see Figure 5.7(b). This corresponds to a smooth increase in force, which can be seen in Figure 5.6. At $d = 26.75$ mm the force reached a maximum of 2.4 N, before decreasing. At $d = 29.5$ mm the left localized fold bifurcated in two, as seen in Figure 5.7(c), and the force dropped to 0.18 N. Each bifurcation corresponded to an immediate sharp drop in the tension force. The process of smooth increases in force, corresponding to the localized folds increasing in radius, and followed by a sharp bifurcation repeated for the bifurcations to four, five, and six localized folds. These bifurcations occurred at $d = 50.5$ mm, $d = 56.5$ mm, and $d = 59.25$ mm, respectively. In addition, the frequency of the bifurcation increased. Once in the six fold configuration, the folds ceased to bifurcate further. Instead, they slowly increased in radius until they completely conformed to the hub surface.

5.3 Comparison with LS-Dyna Simulation

The finite element model is shown in Figure 5.8. It consists of a fully deployed tape spring, four temporary cylinders of radius $R_{cy} = 20$ mm used to create the initial two folds, and a hub of radius

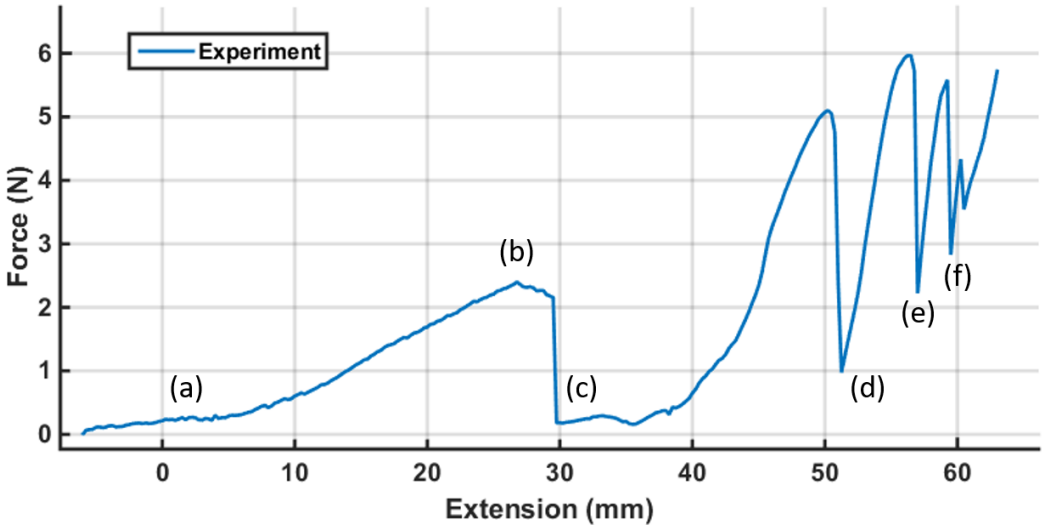

Figure 5.6: Force profile corresponding to the opposite-sense wrapping of a steel tape spring around a steel hub, where $R_{hub} = 4.125R_i$. Average of three repeated experiments.

$R_{hub} = 82.5$ mm. The temporary cylinders and hub are modeled as rigid bodies, fully constrained in all degrees of freedom.

Based on the results from Section 4.1.2 two tape spring models, meshed with C^0 triangular shell elements and fully integrated (Type -16) quadrilateral shell elements, were considered. The results for simulations with C^0 triangular shell elements are presented here. The results for simulations utilizing fully integrated (Type -16) quadrilateral shell elements are presented in Appendix B.

Contact between the hub and tape spring uses the friction coefficient $\mu = 0.18$ measured in Section 5.2.3. Contact damping of 0.05% of critical viscous damping was applied to reduce the noise in the force output due to vibration. Contact damping acts perpendicular to the contacting surfaces. LS-Dyna calculates the critical damping $\xi_{crit,contact-damping}$ by [13]

$$\xi_{crit,contact-damping} = 2m_{node}\omega \tag{5.10}$$

where $m = \min(m_{slave}, m_{master})$, the minimum of the master and slave node masses during contact and

$$\omega = \sqrt{k\frac{m_{slave} + m_{master}}{m_{slave}m_{master}}} \tag{5.11}$$

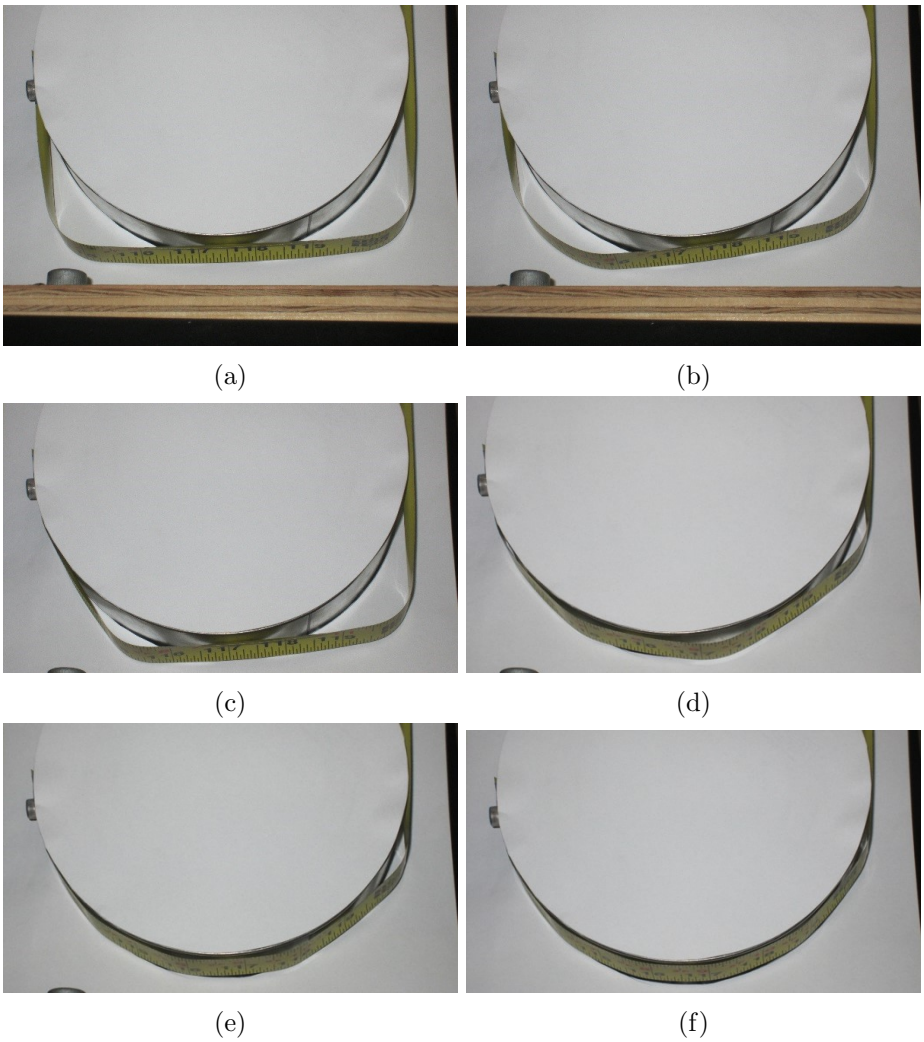

Figure 5.7: Snapshots of the wrapping experiment, corresponding to the forces in Figure 5.6. (a) Initial configuration and (b) immediately before bifurcation to three localized folds. Left localized fold has increased in radius. (c) Immediately after bifurcation to three localized folds, (d) four localized folds, (e) five localized folds, and (f) Six localized folds.

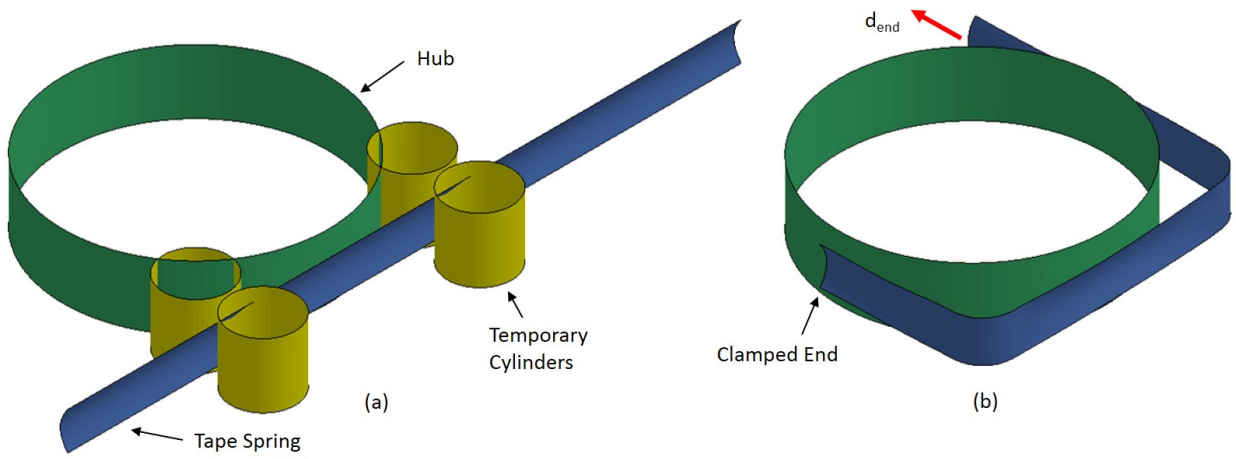

Figure 5.8: (a) Initial configuration of coiling numerical simulation. (b) Tape spring folded with two localized bends and temporary cylinders removed. Displacement d_{end} applied to fully coil tape spring.

where k is the interface stiffness.

5.3.1 Folding Steps

The simulation started with the tape spring in the fully deployed configuration, as shown in Figure 5.8(a). To fold the tape spring into the initial two-fold configuration, as in Figure 5.8(b), boundary conditions were applied to flatten the tape spring at the two fold locations. After flattening, these boundary conditions were removed, and frictionless contact with the four cylinders was enabled via the keyword `*AUTOMATIC_SURFACE_TO_SURFACE`. These cylinders constrained the tape spring to remain flattened. Displacement boundary conditions were then applied to the ends of the tape spring, completely constraining the motion of the ends as they were wrapped around two temporary cylinders. Equation 4.2 was used to determine the displacement boundary conditions required to fold the tape spring.

Contact with the temporary cylinders was then removed, and the tape spring allowed to find an equilibrium configuration. Mass nodal damping was applied to remove excess kinetic energy. This resulted in a two-fold configuration shown in Figure 5.8(b) that matches the initial configuration used in the experiments, as shown in Figure 5.7(a). A full description of the applied boundary and contact conditions is detailed in Table 5.1, with corresponding node sets defined in Appendix B.

Description	Time (s)	Node Set	Boundary Conditions Activated
Restrain out of plane displacement	0 - 0.17	Midline Nodes	$u_y = 0$
Restrain out of plane displacement	0 - ∞	Top end node	$u_y = 0$
Restrain out of plane displacement	0 - ∞	Bottom end node	$u_y = 0$
Edges are displaced to flatten tape-spring	0 - 0.04	Edge nodes	$u_x = 3.7$ mm
Fix midline position as edges are flattened	0 - 0.06	Midline nodes	$u_x = u_z = 0$
Contact applied between tape spring and cylinders	0.04 - 0.16	All nodes	
Fix central nodes in Z	0 - 0.20	Central nodes	$u_z = 0$
Fix central nodes in X	0.16 - 0.20	Central nodes	$u_x = 0$
+Z end node displaced to fold tape spring around cylinders	0.06 - 0.21	Top end node	$u_x = f_1(t), u_z = g_1(t)$
-Z end node displaced to fold tape spring around cylinders	0.06 - 0.21	Bottom end node	$u_x = f_2(t), u_z = g_2(t)$
Damping applied to remove kinetic energy	0.17 - 0.21	All nodes	$\beta = 100$
Fix hole region	0.2 - ∞	All nodes	$u_x = u_z = 0$
End node held in place	0.20 - 0.21	End node	$u_x = u_z = 0$

Table 5.1: Summary of simulation steps for wrapping an isotropic tape spring around a hub, where $R_{hub} > R_i$.

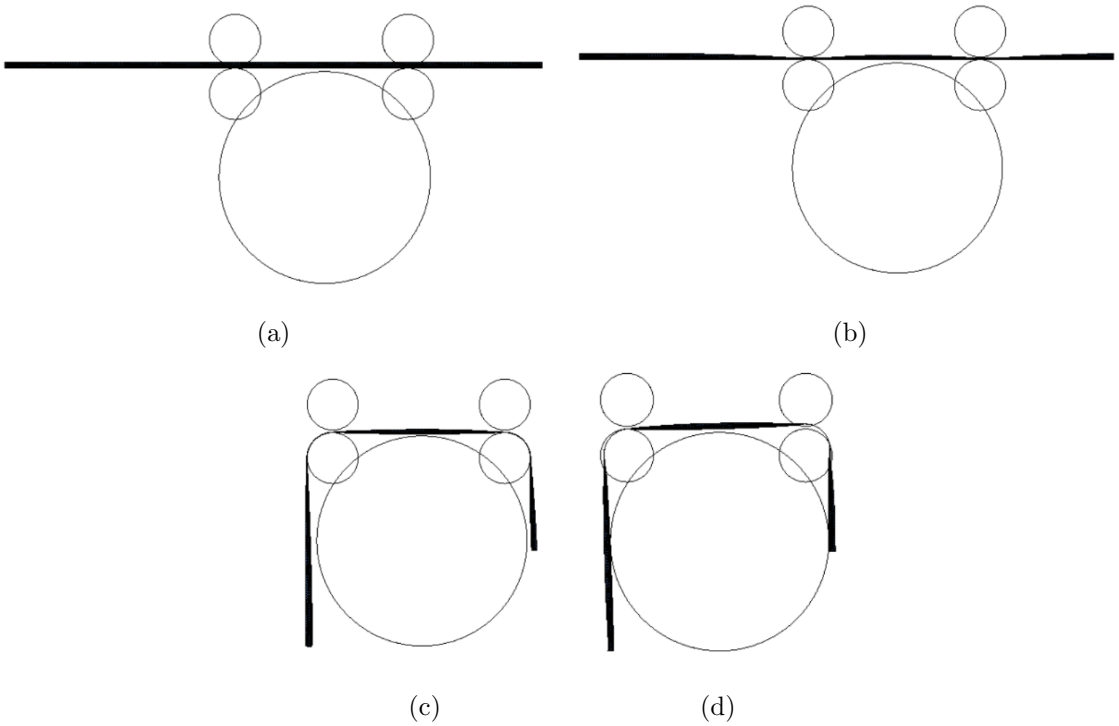

Figure 5.9: (a) Initial configuration, (b) 0.04 s tape spring edges are compress and contact with temporary cylinders enabled, (c) 0.17 s tape spring ends displaced so boom wraps around cylindrical crushers, (d) 0.21 s contact with temporary cylinders removed, and tape spring equilibrium configuration found.

5.3.2 Wrapping Simulation Mesh Sensitivity

As in the experiment, the tape spring was wrapped by applying a displacement boundary condition of d to the non-clamped end. To remove noise from the force data, mass nodal damping of $\beta = 10$ s^{-1} was applied for the duration of the wrapping simulation. As described in Section 3.6, mass nodal damping applies a force at each node opposite to that node's velocity vector. This force is governed by the velocity v, the node mass m, and the damping coefficient β

$$F_v = \beta m v \tag{5.12}$$

The mesh sensitivity of the wrapping simulation was investigated by meshing the tape spring with elements of edge length 3 mm, 2.5 mm, 2 mm, and 1.5 mm, then repeating the simulation. The effect on tension force experienced during wrapping is shown in Figure 5.10.

For the coarse mesh simulation where element side lengths were 3 mm, no bifurcations of the

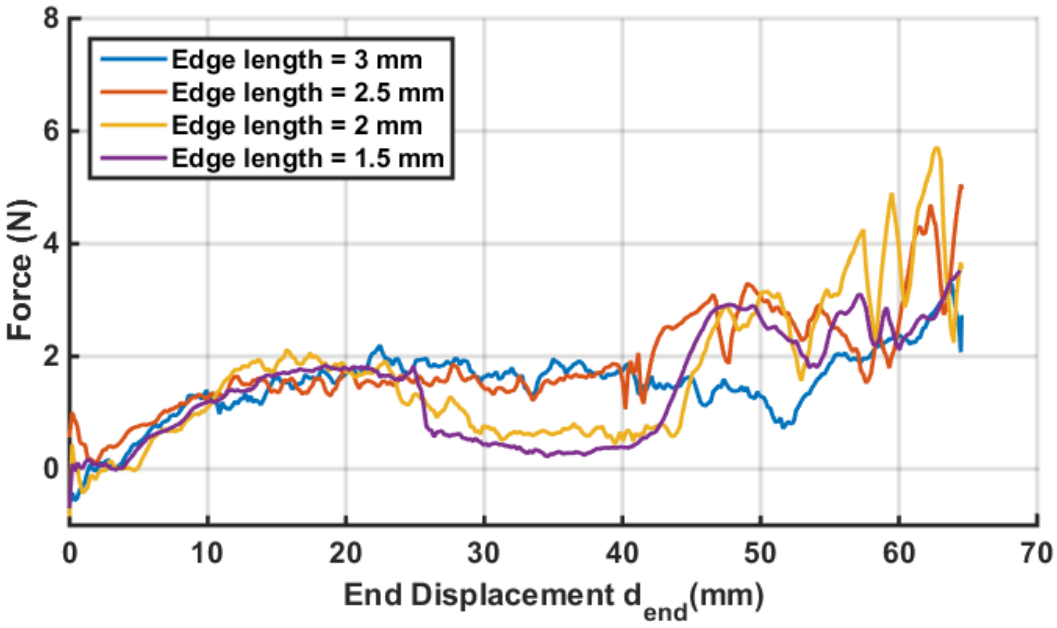

Figure 5.10: Comparison of simulation tension force results during wrapping for tape springs meshed with elements with side lengths = 3 mm, 2.5 mm, 2 mm, and 1.5 mm ($d_{end} = d$). Mass nodal damping was set to $\beta = 10$ s^{-1}, and the data smoothed with a 5 point moving average to remove noise.

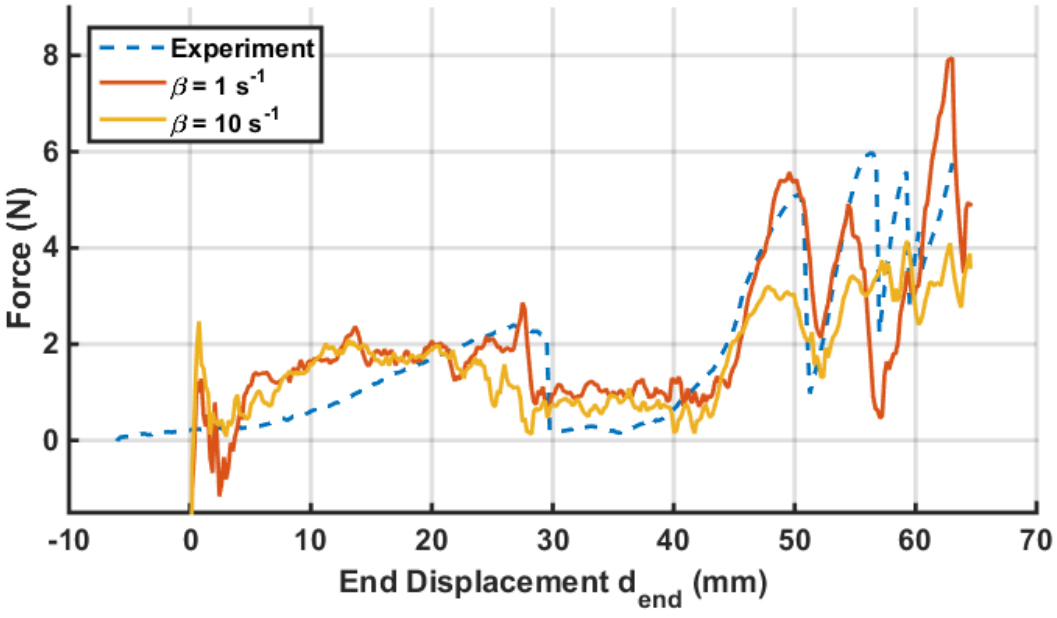

Figure 5.11: Comparison of experimental results and simulation results with mass nodal damping set to $\beta = 1$ s^{-1} and $\beta = 10$ s^{-1} for the entire wrapping simulation ($d_{end} = d$). The data has been smoothed with a 5 point moving average to remove noise.

localized folds were observed. Instead, the radius of the localized folds increased gradually, until they conformed to the radius of the hub. For the mesh with 2.5 mm, the localized fold furthest from the clamped end bifurcated at $d_{end} = 40.8$ mm, followed by additional bifurcations as d increased.

The meshes utilizing elements with 2 mm and 1.5 mm edge lengths have converged for the wrapping simulation for $0 \leq d_{end} \leq 58$ mm. The mesh incorporating 2 mm sized elements showed higher force peaks than the 1.5 mm case in the region where $58 < d_{end} \leq 65$ mm. Both simulations experience the bifurcation of the localized fold closest to the clamped end at $d_{end} = 25.8$ mm, with additional bifurcations at $d_{end} = 52.9$ mm, 58.4 mm, 60.4 mm, and 63.8 mm. Due to time constraints, the simulations in the following sections utilize tape springs meshed with 2 mm long elements.

5.3.3 Sensitivity to Mass Nodal Damping

To determine the maximum mass nodal damping to use in the wrapping simulations, simulations with $\beta = 0.1$ s^{-1} to 1000 s^{-1} were performed. The force profiles for the wrapping of the tape spring for $\beta = 1$ s^{-1} and 10 s^{-1}, are compared against the experiment in Figure 5.11. Plots comparing the results for $\beta = 0.1$, 1, 10, 100, and 1000 s^{-1} are in Appendix B. Also in Appendix B is a sensitivity study on the effect of the friction coefficient μ on the tension force during wrapping.

For $\beta \leq 1$ s^{-1}, the simulation and experiment closely match until the four-fold configuration is reached for an extension of $d = 54.8$ mm. This includes the force peaks at bifurcation of 2.2 N and 5.4 N, compared to 2.2 N and 5.1 N experimentally. At $d = 54.8$ mm the folds bifurcate early in the simulation into the five-fold configuration, compared to $d = 56.5$ experimentally.

Note that when $\beta \geq 10$ s^{-1} is used during wrapping, the force results differ substantially from the experimentally observed behavior, as seen in Figure 5.11(b). In these simulations, the localized bend opposite the clamped end bifurcates in two instead. This shows the bifurcation process is sensitive to external conditions, including minor increases in damping. Once this change occurs, the tape spring configuration never returns to the experimentally observed one. This result also indicates that the wrapping problem is non-unique, and the force required to tension the boom depends greatly on the configuration of the wrapped tape spring, not just on the displacement applied to wrap the tape spring.

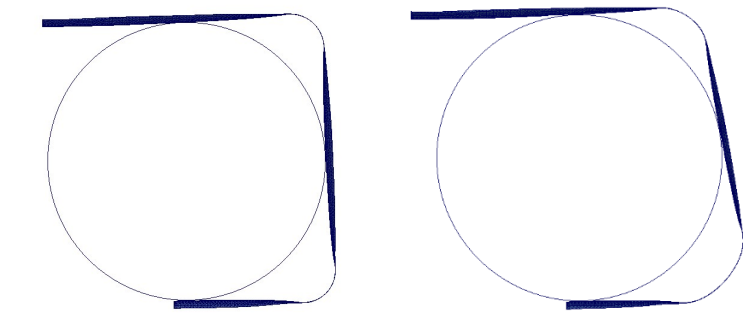

(a) $d = 0$ (b) $d = 14.2$ mm

(c) $d = 27.3$ mm (d) $d = 27.5$ mm

Figure 5.12: Boom configurations in (a) initial configuration, (b) 14.2 mm displacement causes bottom bend to increase in radius, (c) at 27.3 mm displacement bottom bend starts to bifurcate in two, and (d) bottom bend has bifurcated at 27.5 mm displacement, giving three localized bends.

5.3.4 Localized Fold Bifurcation

Figure 5.12 shows the configurations of the tape spring as two localized folds bifurcate into three, for the $\beta = 1$ s^{-1} case. In the initial configuration at $d = 0$ mm, the folds each have as expected a radius of 19 - 20 mm. As d increased, the localized fold closest to the clamped end increased in radius. At $d = 27.3$ mm the fold changed from a constant radius to one having two regions of high curvature at each end of the fold, joined by a flattened, almost straight section in between. At $d = 27.5$ mm the fold bifurcated into two distinct folds of radius $R \approx R_i$.

The bending strain energy per unit length of tape spring, corresponding to the fold bifurcation, is plotted in Figure 5.13. The bending energy is calculated by extracting the node locations from LS-Dyna and calculating the longitudinal and transverse curvature at each node. This is inputted into Equation 5.1 to give the areal energy density at each node, then integrated across the tape spring's transverse direction, to give the energy per unit length along the tape spring.

Figure 5.13(a) shows the initial configuration, where the energy in the localized bends is con-

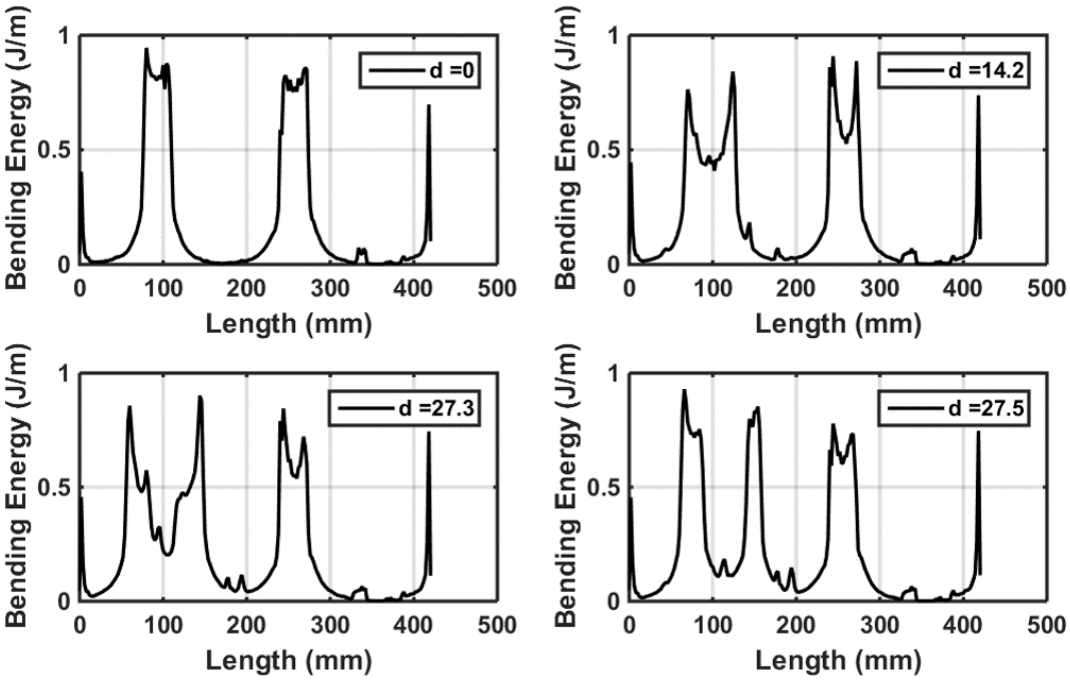

Figure 5.13: The bending energy per unit length along the booms corresponding to the boom configurations in Figures 5.12 (a) to (d). Length = 0 corresponds to the clamped end, and the total length of the boom is 420 mm.

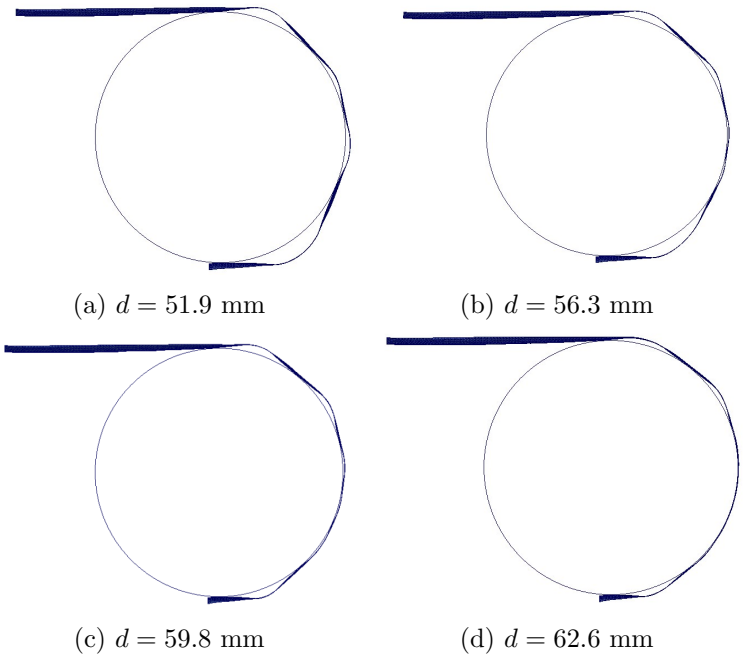

(a) $d = 51.9$ mm (b) $d = 56.3$ mm

(c) $d = 59.8$ mm (d) $d = 62.6$ mm

Figure 5.14: Boom configurations for the higher fidelity wrapping model in (a) four bends, (b) five bends, (c) six barely visible localized bends, and (d) at $d = 62.6$ mm displacement three bends have flattened and conform to the hub radius, leaving three remaining bends.

centrated near the edges of the transition region, with a slight dip in the middle. As d increases, the length of the boom that covers the subtended arc angle of the hub decreases leading to one or more folds increasing in radius. Once the bend radius grows sufficiently large, the majority of the energy is concentrated where the bends interface with the transition regions, with lower energy in the middle of the bend itself. At this point the bend with the largest radius bifurcates in two.

5.3.5 Higher Fidelity Wrapping Simulation

A higher fidelity simulation that more closely captures the experimentally observed behavior was carried out by modifying the the wrapping model as follows. Up until $d = 52.3$ mm the $\beta = 1$ s^{-1} model was used. After this point β was increased to 1000 s^{-1} in order to reduce the kinetic energy of the tape spring when $d \approx 54.8$ mm and thus model more accurately the bifurcation to four folds. This decreases the kinetic energy available to the tape spring to jump to different stable configurations. As displayed in Figure 5.15, the tape spring force profile then matched well the experiments until $d = 59$ mm.

The energy components present in this model are plotted in Figures 5.16(a) to (c). The internal

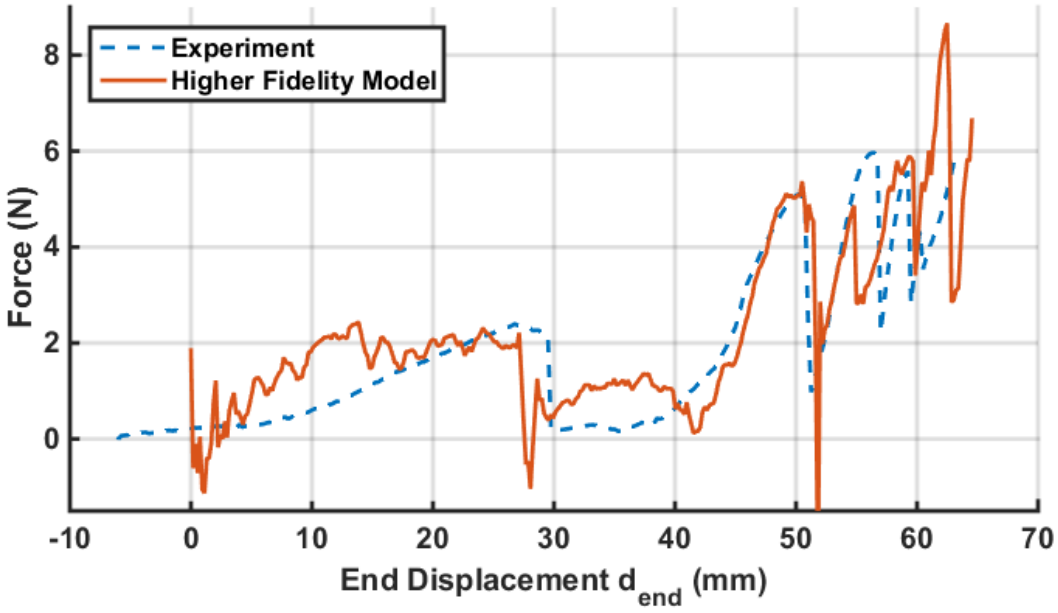

Figure 5.15: Force profile obtained from the high fidelity model.

energy steadily increases throughout the wrapping process with small dips at each bifurcation. The total change in internal energy from each bifurcation is $\leq 1\%$ of the internal energy. Figure 5.16(c) shows that this energy is converted into kinetic energy which subsequently decays due to the imposed damping. The magnitude of the kinetic energy remains $< 1\%$ of the internal energy throughout the simulation. In addition, the effect of increasing damping at $d = 52.3$ mm is clearly evident in the kinetic energy plot.

5.3.6 Fully Wrapped Configuration

The fully wrapped configuration was defined as the point where the centerline of the tape spring conformed to the hub surface to within 0.25 mm in the region $\gamma_{min} \leq \gamma \leq \gamma_{max}$, as defined in Figure 5.17(a). The separation distance between the tape spring centerline and the hub surface when fully wrapped is shown in Figure 5.17(c), and the corresponding longitudinal curvature (κ_l) in Figure 5.17(d).

To remove the effect of the localized fold closest to the clamped end, the first 70 mm of the tape spring (L_{remove}) was excluded from the region used to determine when the tape spring was the fully wrapped. Since this length comprises a reduced arc length of the hub as the hub radius

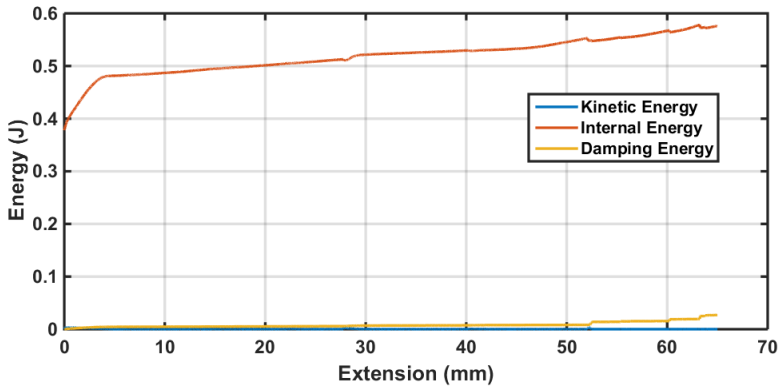

(a)

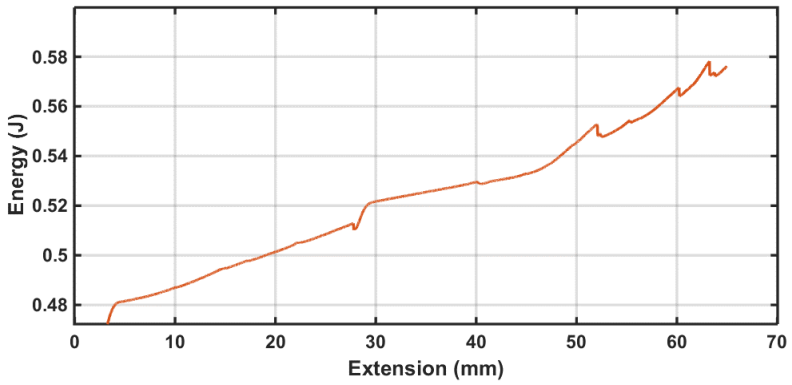

(b)

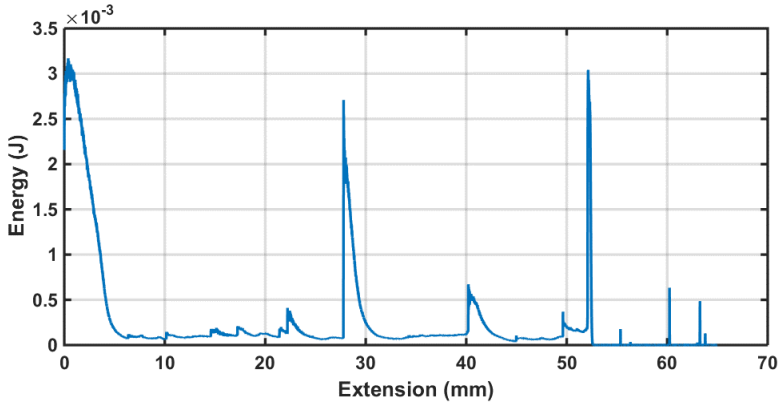

(c)

Figure 5.16: Energy components in the wrapping simulation after folding. (a) All energy, (b) close up of internal energy, drops correspond to bifurcations, and (c) close up of kinetic energy, where sudden build ups correspond to bifurcations.

increases, the angle removed is calculated by:

$$\gamma_{min} = 2\tan^{-1}\left(\frac{L_{remove}}{2R_{hub}}\right) \tag{5.13}$$

To remove the boundary condition effect due to the localized fold at $\gamma = 180^o$, γ_{max} was set to 140^o. The maximum allowed separation value of 0.25 mm was selected to minimize the effect on wrapping force of the secondary fold near the clamped end; see Figure 5.17(b). The secondary fold is a boundary condition effect caused by the clamped end, and it would require significantly more tension force on the tape spring to remove this fold than for any other localized folds in the $\gamma_{min} < \gamma < \gamma_{max}$ region. Allowing a 0.25 mm separation gap allows for a secondary fold region in the fully wrapped configuration. An equally valid approach would be to increase γ_{min}.

5.4 Effect of Hub Radius on Tension Force

A key objective of this work is to determine the effect of the hub radius on the wrapping of tape springs. To investigate the effect of the hub radius on the required tension force, the wrapping simulation was run for hub ratios $\frac{R_{hub}}{R_i} = 0.2$ to 5.25. The tape spring modeled has the same material and mechanical properties as used in the simulations in Section 5.3. The length of tape spring tested is consistent at 420 mm. To remove the contribution to the tension force from the length of tape spring in contact with the hub, friction was removed. For the entire duration of the wrapping simulations the damping coefficient was set as $\beta = 1000$ s^{-1} to reduce noise in the force values. Although this choice of β affects the bifurcation locations and times, the force measurement extracted from these simulations occurs at the end of the wrapping once all bifurcations have occurred. The method for determining when the tape spring had become fully wrapped was the same as used in Section 5.3.6.

For simulations with $\frac{R_{hub}}{R_i} > 1$ the setup is the same as described in Section 5.3 with one end of the tape spring clamped directly to the hub. However, for $\frac{R_{hub}}{R_i} < 1$ the boundary condition effects mentioned in Section 5.3.6 necessitate modifying the simulation, to avoid these effects from dominating the wrapping simulation. Instead, for $\frac{R_{hub}}{R_i} < 1$ the tape spring is folded symmetrically around the hub, one end pinned, and then the other end displaced d as before. An example of the simulation setup is in Figure 5.18.

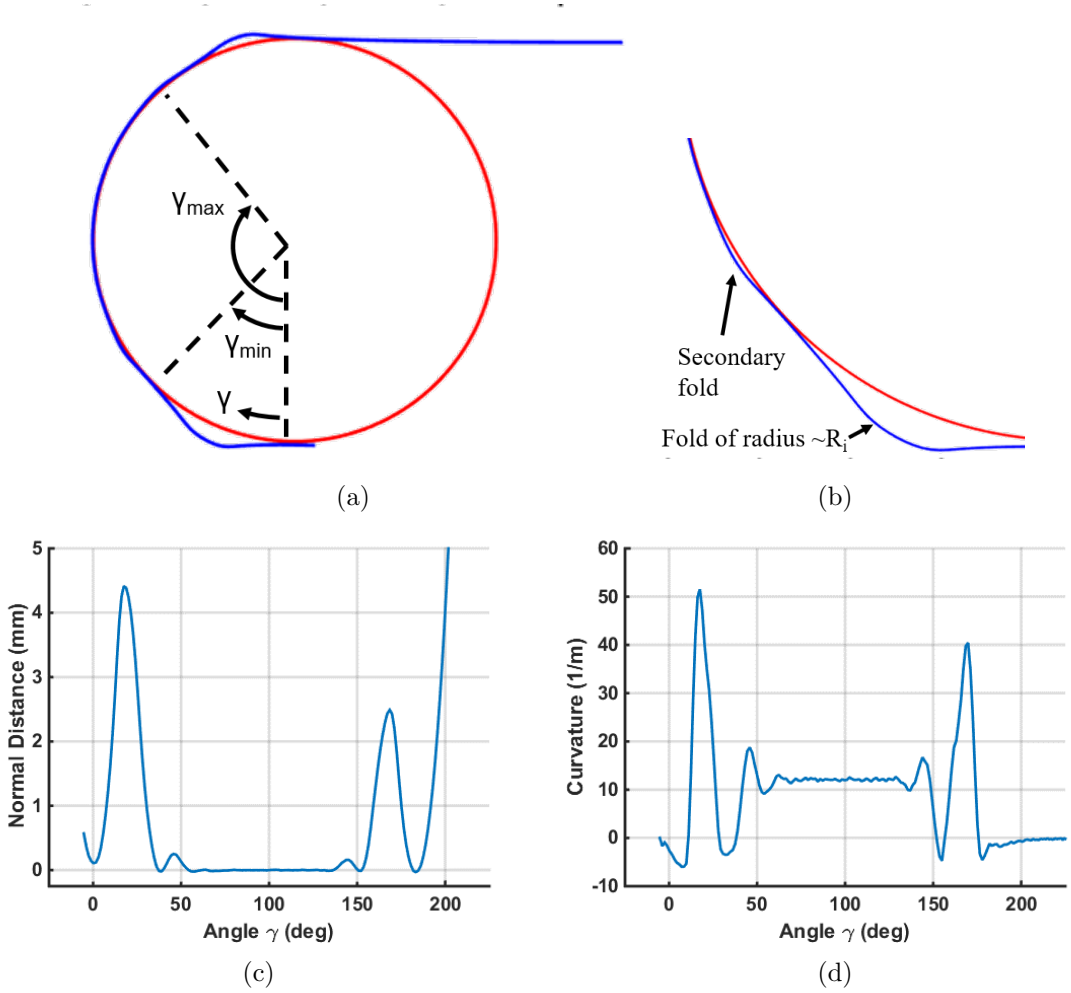

Figure 5.17: Tape spring at the end of the wrapping simulation (a) Top view. (b) Close up of secondary fold. (c) Normal distance between the hub and tape spring. (d) Longitudinal curvature of tape spring centerline in fully wrapped configuration

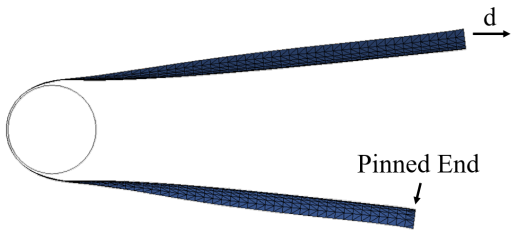

Figure 5.18: Simulation setup for $\frac{R_{hub}}{R_i} < 1$.

Obtaining direct experimental validation of the results was not feasible, as it would require measuring the separation distance between the tape spring and the hub over an arc of 180^o. Instead, the validation of the model in Section 5.3.2 was taken to be sufficient validation of the simulation accuracy.

5.4.1 Results

The force required to wrap a tape spring around a hub $0.4R_i \leq R_{hub} \leq 0.7R_i$ is shown in Figure 5.19. For these simulations the tape spring started with a single fold of radius R_i. As tension was applied the localized fold decreased in radius until it conformed to the hub surface. For ratios $0.7R_i \leq R_{hub} \leq R_i$ the exact tension force when the tape spring is fully wrapped required was difficult to obtain from the force vs displacement profiles. Due to the very low wrapping forces as the hub radius approaches the localized bend radius, the numerical noise in the force due to the tape spring vibrating against the hub had a significant effect the force value when the tape spring was fully wrapped.

For $R_{hub} < R_i$, the quadratic fit in Figure 5.19 can be explained by starting with the bending energy in a wrapped tape spring. A schematic of the coiling simulation is shown in Figure 5.20. First, start by replacing R_i with R in Equation 5.1. Then, differentiate this equation with respect to R to get

$$\frac{dU}{dR} = \frac{DR_t\alpha\gamma}{2}\left(\frac{1}{R_t^2} - \frac{1}{R^2}\right) \tag{5.14}$$

The energy U can also be written in terms of the work performed by the tensioning force

$$\begin{aligned} \Delta U &= F\Delta L \\ \frac{dU}{dL} &= F \end{aligned} \tag{5.15}$$

By geometry

$$\begin{aligned} -\gamma\Delta R &= \Delta L \\ \frac{dR}{dL} &= \frac{-1}{\gamma} \end{aligned} \tag{5.16}$$

Combining

$$F = \frac{dU}{dL} = \frac{dU}{dR}\frac{dR}{dL} = \frac{DR_t\alpha}{2}\left(\frac{1}{R^2} - \frac{1}{R_t^2}\right) \tag{5.17}$$

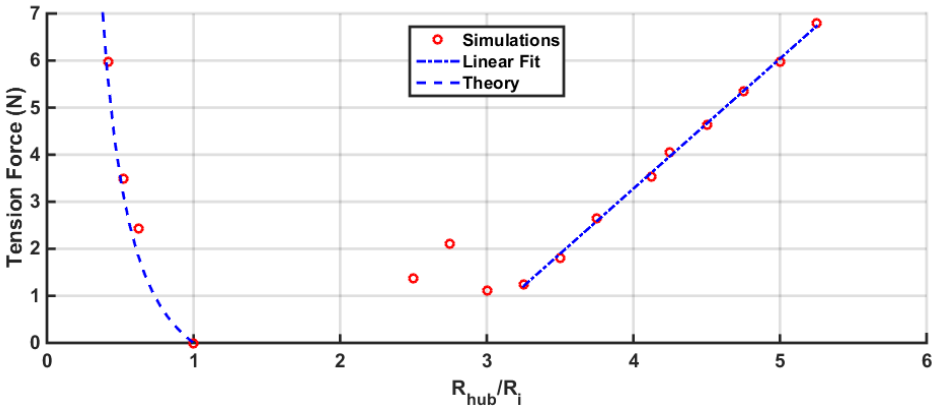

(a)

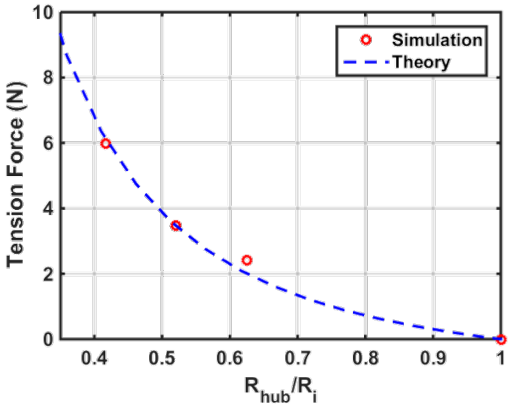

(b)

Figure 5.19: (a) Tension force required to fully wrap the steel tape spring for $0.4R_i < R_{hub} < 0.65R_i$ and $2.5R_i < R_{hub} < 5.25R_i$. (b) Close up of $0.35R_i < R_{hub} < R_i$ region.

When the tape spring is fully coiled around the hub $R = R_{hub}$ and

$$F = \frac{DR_t\alpha}{2}\left(\frac{1}{R_{hub}^2} - \frac{1}{R_t^2}\right) \tag{5.18}$$

Remember, that for an isotropic material $R_i = R_t$, thus, for $R_{hub} < R_i$, F follows an inverse square law. This derivation requires a key assumption, namely that the radius R is constant for the entire localized fold. To account for this effect, a fitting parameter η is added, giving

$$F = \frac{\eta DR_t\alpha}{2}\left(\frac{1}{R_{hub}^2} - \frac{1}{R_t^2}\right) \tag{5.19}$$

This is plotted against the simulation results in Figure 5.19(b), for $\eta = 2$.

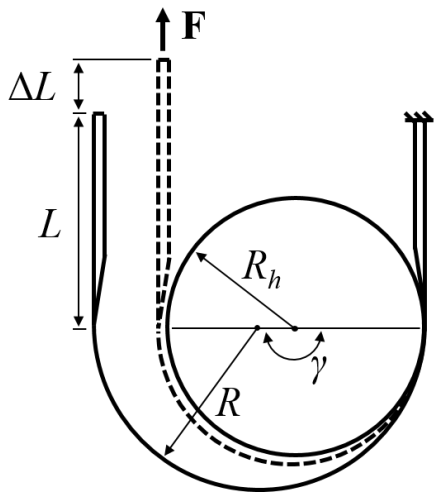

Figure 5.20: Schematic of coiling simulation for $R_{hub} < R_i$.

The force required to wrap a tape spring around a hub for $2.5R_i \leq R_{hub} \leq 5.25$ is shown in Figure 5.19(b). There are two very clear features. The first being that for $\frac{R_{hub}}{R} > 3.25$ a clear linear trend has developed.

$$F = 2.795\frac{R_{hub}}{R_i} - 8.465 \text{ Newtons} \tag{5.20}$$

Below $\frac{R_{hub}}{R} = 3.25$ the linear trend no longer holds true. In particular, $\frac{R_{hub}}{R} = 3.5$ is the smallest ratio where the tape spring localized folds bifurcated. For $2.5R_i \leq R_{hub} \leq 3.25$ the localized fold furthest from the clamped end increased in radius, until that radius matched the hub.

5.5 Extension to Non-Isotropic Tape Springs

When scaling up to large space structures, steel tape springs are too heavy and their large coefficient of thermal expansion is a severe limitation. For those reasons composite materials are of interest. As detailed in Section 2.4.2, the localized bend radius for an orthotropic tape spring is [8]

$$R_i = R_t\sqrt{\frac{D_{11}}{D_{22}}} \tag{5.21}$$

Tape springs were manufactured by Caltech graduate student Christophe Leclerc using 17 GSM uni-directional tape made of carbon fiber (T800 by Torayca) and epoxy resin (ThinPreg 120EPHTg-

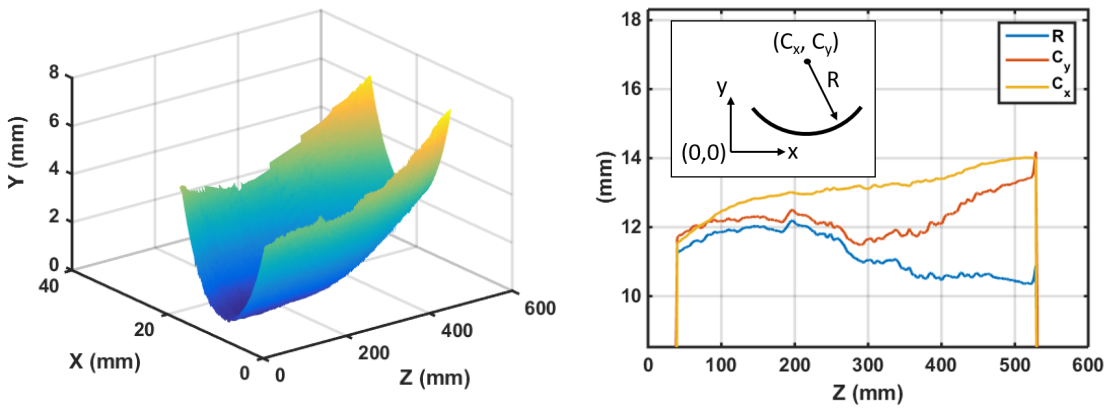

(a) (b)

Figure 5.21: (a) Point cloud of a carbon fiber tape spring specimen, generated from a FARO arm laser scanner. (b) Center and radius of the tape spring cross-section along the boom length.

402 by North Thin Ply Technology). This material had a cured thickness of approximately 18 µm per ply. When bonded into the chosen a four ply layup of $[0/90]_S$, the total thickness was ≈71 µm. The mold radius was $R_t = 12.7$ mm, and the initial subtended arc of the tape spring $\alpha = 90^o$. With these parameters, $D_{11} = 0.0034$ Nm, $D_{22} = 0.00065$ Nm, and for these values, Equation 5.21 gives a nominal localized bend radius $R_i = 29$ mm.

To measure the post-cure shape, and capture and manufacturing imperfections, a laser scanner on a FaroArm portable coordinate measuring machine was used to obtain a point cloud of the tape spring surface. The results are shown in Figure 5.21(a). Of particular note is the tape spring is initially bent in the Y direction by several millimeters along its length. The point cloud data was split into 100 cross-sectional slices, corresponding to 5 mm increments along the tape spring length. A circle fit in MATLAB was applied, to find the circle center and radius of the tape spring for each cross-sectional slice as shown in Figure 5.21(b). Note that the radius decreased during the curing phase, and varies between 10.5 and 12 mm along the length of the tape spring.

5.5.1 Wrapping Experiment with $3.3R_i = R_{hub}$

The experimental setup used on the carbon fiber tape spring was the same as used in Section 5.2.2. The cylindrical hub of diameter $R_{hub} = 82.5$ mm was rigidly attached to the base of an Instron tensile testing machine. The hub has a radius 6.5 times the mold radius the tape spring was cured on, however due to the orthotropic nature of the tape spring $\frac{R_{hub}}{R_i} = 3.3$. One end of the composite

tape spring was clamped to the side of the hub, and folded in opposite sense around the hub, as shown in Figure 5.22(a). The other end was attached to the load cell of an Instron material testing machine. The force was recorded as this end was displaced vertically at a rate of 22 mm/min.

(a) $d_{end} = 12.5$ mm (b) $d_{end} = 38$ mm (c) $d_{end} = 49$ mm

(d) $d_{end} = 51$ mm (e) $d_{end} = 66.5$ mm (f) $d_{end} = 75$ mm

Figure 5.22: Ultra-thin carbon fiber tape spring configurations during wrapping. (a) Initial configuration, (b) fold radii increases, (c) configuration just before fold bifurcation, (d) fold bifurcates into two, (e) four-fold configuration, and (f) fully wrapped configuration.

The results obtained over three separate tests are shown in Figure 5.23. At end displacement $d_{end} = 12.5$ mm, the tape spring region between the two folds comes into contact with the hub. Between $d_{end} = 12.5$ mm and 49 mm the fold radii gradually increase, until at 50 mm the fold closest to the clamped end bifurcates into two folds. At 66.5 mm bifurcation again occurs to create a four-fold configuration.

As d_{end} increases in the two-fold configuration, the point of contact between the hub and the tape spring moves around the hub. The force profile in Figure 5.23 clearly shows stick-slip behavior, where the applied force increases until static friction is overcome. Then the point of contact between the tape spring and hub slides along the hub surface. This explains the drops in force at $d_{end} = 38$ mm, 41.2 mm, and 46.4 mm.

5.5.2 LS-Dyna Simulations

Two LS-Dyna simulations of the carbon fiber tape spring were performed. These simulations were identical to the ones performed in Section 5.3.1, with the exception that the steel tape spring was

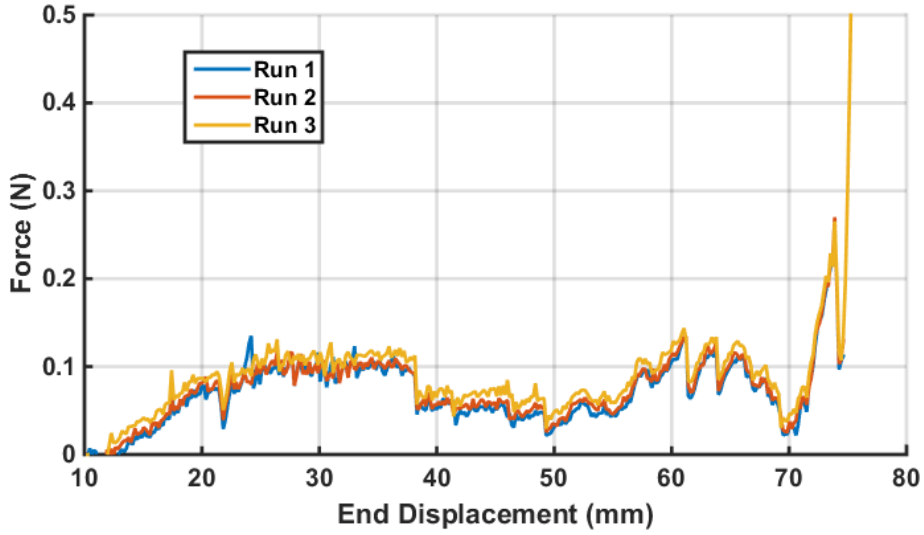

Figure 5.23: Force profiles corresponding to opposite-sense wrapping experiments of an ultra-thin carbon fiber tape spring around a steel hub.

replaced with carbon fiber. In the first simulation, it was assumed that the radius of the tape spring is uniform and equal to the radius of the mold $r = 12.7$ mm. In the second simulation, the actual cross-section dimensions were varied along the length of the tape spring as shown in Figure 5.21(b).

To generate the mesh for the second simulation, an initial mesh with constant cross-section along the length was generated. This mesh was imported into MATLAB, and the node locations scaled to match R, C_x, C_y along the length of the boom. The mesh was then exported back into LS-Dyna.

The simulation results are shown in Figure 5.24. Both simulations quantitatively agree with the experimental force results up to $d = 50$ mm. This corresponds to the localized fold increasing in radius prior to bifurcation. However, for the constant cross-section simulation, the fold furthest from the clamped end increased in radius, and bifurcated at $d = 39$ mm. As seen earlier in Section 5.3.2 the wrapping process is highly path dependent, and if one bifurcation does not match the experiments, the following bifurcations will then show increasing deviations. The bifurcation from three to four folds occurs at $d = 61$ mm. The force then increases as each of the localized folds increase in radius. The fold radii continue to increase until the localized folds fully conform to the hub surface.

The simulation that incorporates the actual cross-section agrees a bit better with the experi-

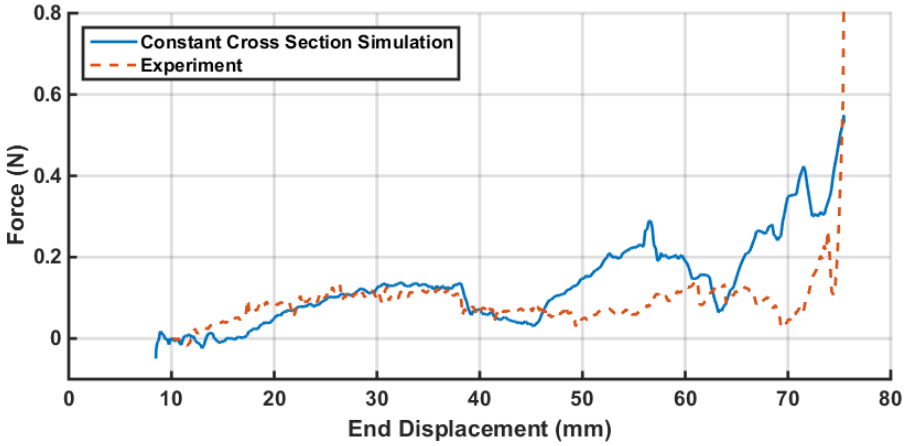

(a)

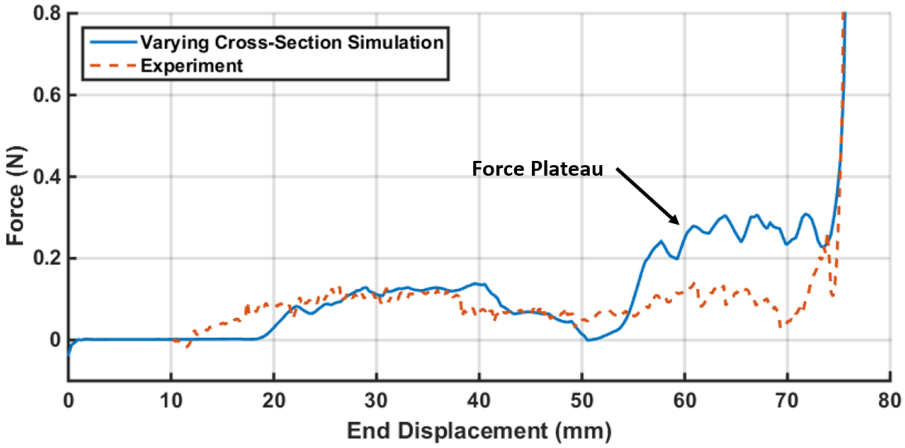

(b)

Figure 5.24: Comparison of force profiles required to tension an ultra-thin carbon fiber boom around a hub of $R_{hub} = 3.3R_i$ for (a) boom simulated with a constant cross-section, and (b) boom simulated with cross-section varying along length to better match physical model.

ment. Unlike the constant cross-section simulation, the localized fold closest to the clamped end bifurcates first. From $d_{end} = 55$ to $d_{end} = 75$ the localized folds increase in radius, and the force reaches a plateau of around 0.3 N. The bifurcation to four folds occurs at $d_{end} = 65$ mm and only results in a small change in force. This over-estimates the experimentally observed force plateau by a factor of approximately 3. At $d_{end} = 75$ the radii of all localized folds have increased to match the hub radius.

5.6 Discussion

An analytical model developed to capture fold bifurcation closely matches the observed simulation behavior when wrapping isotropic tape springs around hubs with $R_{hub} > R_i$. The model predicted that bifurcation would occur for $R_{hub} > 3R_i$. In the wrapping simulations, fold bifurcations occurred for $R_{hub} > 3.25R_i$.

When modeling the wrapping behavior of isotropic tape springs, the order of fold bifurcation is highly path dependent. Small changes in friction coefficient and viscous damping can significantly change the wrapping force profile. When validating against experimental data, if a single fold bifurcation does not match the experiment, the force profile will cease to match for the rest of the wrapping process. In the LS-Dyna simulations, meshing the tape springs with C^0 triangular shell elements allowed the bifurcation order and force profile to accurately match the experimental data until the third bifurcation. Tuning viscous damping ensured the results matched until after the fourth bifurcation.

When coiling the steel tape spring around hubs of various radii and excluding friction, two trends were observed. For $R_{hub} > 3.25R_i$ the force required to fully wrap the tape spring follows a linear trend. It is important to exclude boundary condition effects such as secondary folds when determining the fully wrapped configuration for this linear trend to be apparent. For $R_{hub} < 0.7R_i$ the force matches the proposed theory and follow an inverse quadratic profile. For $0.7R_i < R_{hub} < R_i$ determining the fully wrapped configuration and associated tension force is challenging as the localized bend radius is very close to the hub radius.

When extending the wrapping of tape springs to ultra-thin carbon fiber, it is important to capture the exact cross-section, including any manufacturing imperfections. As with friction and viscosity, these can have a significant influence on the bifurcation order and wrapping force.

Chapter 6

Packaging and Deployment of TRAC Booms

Similar to tape springs, TRAC booms can be wrapped tightly around a cylindrical hub as depicted in Figure 2.7. To wrap long booms, the case $R_{hub} \gg R_i$ is of interest. In this case, a tension force is required for the TRAC booms to conform to the wrapped radius R_{hub}, otherwise localized bends will form instead [45]. These bends have the potential to cause problems during deployment, including jamming, and may require higher deployment forces. The coiling of a TRAC boom was simulated and investigated experimentally to capture both the qualitative behavior and the force profile required to tightly wrap such a boom.

6.1 Wrapping Behavior

6.1.1 Localized Bend Radius

Equation 5.1 in Section 5.1 can be applied to find the localized bend radius of a TRAC boom, as for a tape spring. For the flanges $\Delta\kappa_l = \pm\frac{1}{R_i}$, $\Delta\kappa_t = \frac{1}{R_t}$ and $s = \alpha R_t$. For the bond region, $\Delta\kappa_l = \frac{1}{R}$, $\Delta\kappa_t = 0$ and $s = w$, the height of the bond region. Taken together, the total bending energy in the localized bend equates to

$$U_{total} = \frac{R_i \gamma R_t \alpha}{2}\left(\left(\frac{D_{11,f1}}{R_i^2} + 2\frac{D_{12,f1}}{R_i R_t} + \frac{D_{22,f1}}{R_t^2}\right) + \left(\frac{D_{11,f2}}{R_i^2} - 2\frac{D_{12,f2}}{R_i R_t} + \frac{D_{22,f2}}{R_t^2}\right)\right) + \frac{D_{11,b}}{2R_i^2} R_i \gamma w \tag{6.1}$$

where $D_{11,i}, D_{12,i}$, and $D_{22,i}$ correspond to the elements in the D matrix defined by Classical Lamination Theory in Section 2.4.1 that relate curvature to the bending moment in a composite

shell. Note that $i = f1, f2$ or B for the inner flange, outer flange, and bond region, respectively. For equal and symmetric laminates, $D_{11,f1} = D_{11,f2}$, $D_{12,f1} = D_{12,f2}$, $D_{22,f1} = D_{22,f2}$, and the equation simplifies to

$$U_{total} = R_i \gamma R_t \alpha \left(\frac{D_{11,f}}{R_i^2} + \frac{D_{22,f}}{R_t^2} \right) + \frac{D_{11,b}}{2R_i^2} R_i \gamma w \tag{6.2}$$

Differentiating with respect to R_i and setting the derivative equal to zero gives the minimum energy condition, which leads to an estimate of the localized bend radius for a TRAC boom made entirely from symmetric layups

$$R_i = \sqrt{\frac{2R_t \alpha D_{11,f} + w D_{11,b}}{2D_{22,f}} \frac{R_t}{\alpha}} \tag{6.3}$$

6.1.2 Simplified Version of Localized Bend Equation

Equation 6.3 contains three different material properties $D_{11,f}$, $D_{22,f}$ and $D_{11,b}$. Since the bond region is a symmetric layup obtained by bonding the two flanges (neglecting any epoxy thickness in the middle) it is possible to simplify Equation 6.3 such that it contains only flange material properties. The flange D matrix is therefore

$$D_{ij,f} = \frac{1}{3} \sum_{k=1}^{n} Q_{ij,f}^{k} \left(z_k^3 - z_{k-1}^3 \right) \tag{6.4}$$

where Q and z are defined in Section 2.4.1

To convert D_f into D_b, first, the neutral axis is shifted by $\frac{t}{2}$, with t the thickness of the flange. Second, the whole equation is multiplied by 2, since the bond region consists of two flange layups symmetric about the new neutral axis. This gives

$$
\begin{aligned}
D_{ij,b} &= \frac{2}{3}\sum_{k=1}^{n} Q_{ij,f}^{k}\left((z_k - \frac{t}{2})^3 - (z_{k-1} - \frac{t}{2})^3\right) \\
&= \frac{2}{3}\sum_{k=1}^{n} Q_{ij,f}^{k}\left((z_k^2 - tz_k + \frac{t^2}{4})(z_k - \frac{t}{2}) - (z_{k-1}^2 - tz_{k-1} + \frac{t^2}{4})(z_{k-1} - \frac{t}{2})\right) \\
&= \frac{2}{3}\sum_{k=1}^{n} Q_{ij,f}^{k}\left((z_k^3 - \frac{3t}{2}z_k + \frac{3t^2}{4}z_k) - (z_{k-1}^3 - \frac{3t}{2}z_{k-1} + \frac{3t^2}{4}z_{k-1})\right) \\
&= \frac{2}{3}\sum_{k=1}^{n} Q_{ij,f}^{k}(z_k^3 - z_{k-1}^3) - t\sum_{k=1}^{n} Q_{ij,f}(z_k^2 - z_{k-1}^2) + \frac{t^2}{2}\sum_{k=1}^{n} Q_{ij,f}^{k}(z_k - z_{k-1})
\end{aligned}
\tag{6.5}
$$

However, these terms correspond to the ABD matrix for the flange, where

$$
\begin{aligned}
A &= \sum_{k=1}^{n} Q_{ij}^{k}(z_k - z_{k-1}) \\
B &= \frac{1}{2}\sum_{k=1}^{n} Q_{ij}^{k}(z_k^2 - z_{k-1}^2)
\end{aligned}
\tag{6.6}
$$

Therefore, Equation 6.5 can be simplified further to

$$
D_b = 2D_f - 2tB_f + \frac{t^2}{2}A_f \tag{6.7}
$$

Since the flange is made from symmetric layups

$$
D_b = 2D_f + \frac{t^2}{2}A_f \tag{6.8}
$$

So finally, the bend radius equation simplifies to

$$
R_i = \sqrt{\frac{2(R_t^2\alpha + R_t w)D_{11,f} + \frac{t^2 R_t w}{2}A_{11,f}}{2\alpha D_{22,f}}} \tag{6.9}
$$

in terms of only flange properties.

6.1.3 Numerical Analysis of Coiling Behavior

The LS-Dyna FEA model is shown in Figure 6.1. It consists of a fully deployed TRAC boom, four temporary cylinders of diameter $R_{cy} = 20$ mm used to create the initial two folds, and a rigid,

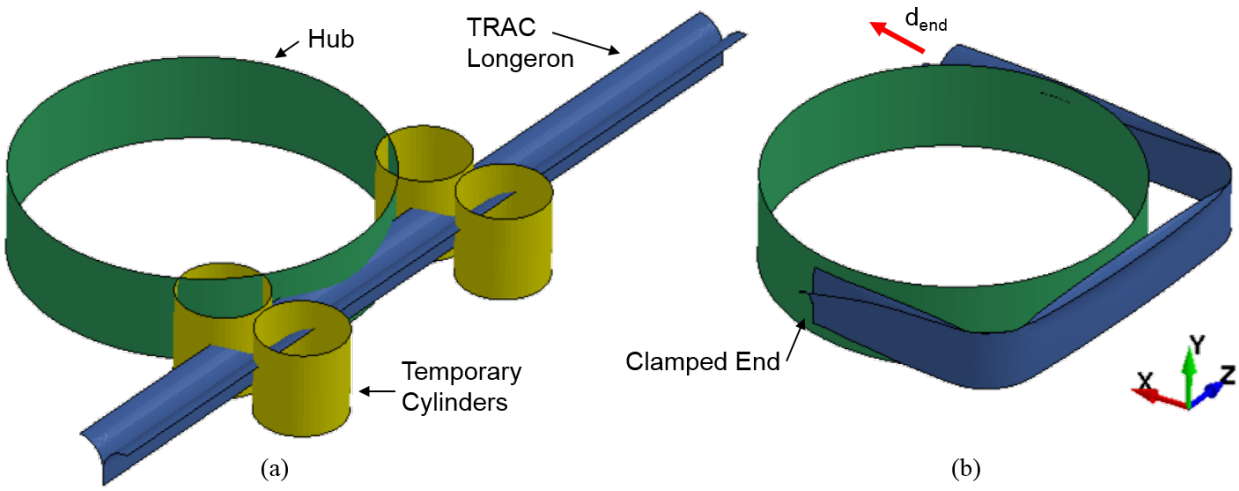

Figure 6.1: (a) Initial configuration of coiling numerical simulation. (b) boom folded with two localized bends and temporary cylinders removed. Displacement d_{end} applied to fully coil boom.

cylindrical hub of diameter $R_{hub} = 82.5$ mm. The temporary cylinders and hub were modeled as rigid bodies, fully constrained in all degrees of freedom. The TRAC boom was meshed with C^0 triangular shell elements. Contact is applied through LS-Dyna's automatic surface-to-surface and automatic single surface keywords. The friction coefficient obtained experimentally was set at $\mu = 0.195$. The carbon-fibre layup and ply properties were the same as detailed in Section 5.5. The flange regions use 17 GSM uni-directional plies made of carbon fiber (T800 by Torayca) and epoxy resin (ThinPreg 120EPHTg-402 by North Thin Ply Technology). This material had a cured thickness of approximately 18 µm per ply. When bonded into the chosen flange four ply layup of $[0/90]_S$, the total thickness was ≈71 µm. The bond region consists of two flanges bonded together, with a resulting eight ply layup of $[0/90/90/0]_S$. The flange thickness was therefore modeled as 0.071 mm, and the bond region thickness double that at 0.142 mm.

The flange cross section has radius $R_t = 10.8$ mm and subtended angle $\alpha = 104°$. These correspond to average values of the boom tested later in Section 6.1.4. With these parameters, $D_{11,f} = 0.0033$ Nm, $D_{22,f} = 0.00065$ Nm, and $D_{11,b} = 0.019$ Nm. For these values, Equation 6.3 predicts a localized bend radius $R_i = 36$ mm.

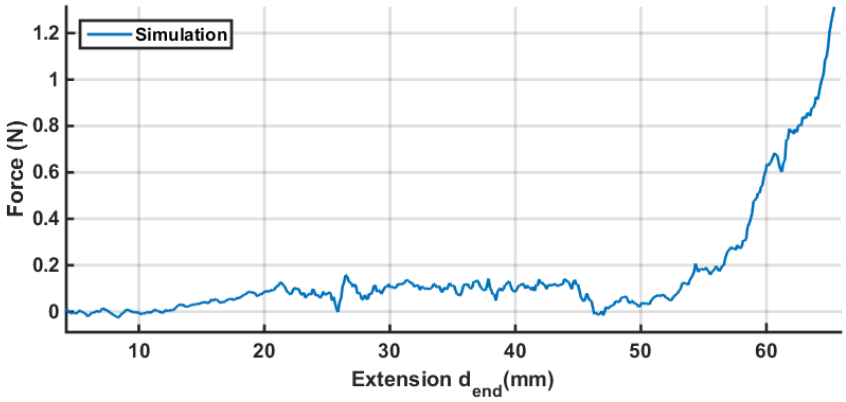

Figure 6.2: Simulation results for a carbon-fibre TRAC longeron with constant cross-section and bond region thickness of 0.142 mm.

6.1.3.1 Folding Step

The simulation started with the boom in the fully deployed configuration, shown in Figure 6.1(a). To fold the boom into the initial two-fold configuration, shown in Figure 6.1(b), boundary conditions were applied to the flange edges to flatten the flanges at the two fold locations. After flattening, these boundary conditions were removed, and contact with the four cylinders enabled. These cylinders force the TRAC boom to remain flattened. Displacement boundary conditions were then applied to the ends of the boom to wrap the boom around two temporary cylinders. Contact with the temporary cylinders was then removed, and the TRAC boom was allowed to find an equilibrium configuration. Damping was applied to remove excess kinetic energy. This resulted in the two-fold configuration shown in Figure 6.1(b). The exact boundary conditions and node set definitions can be found in Appendix C.

6.1.3.2 Coiling Results

With one end of the boom held clamped as shown in Figure 6.1(b) displacement boundary conditions were applied to the other end. A plot of the resulting tension force as a function of the end displacement, d_{end}, is shown in Figure 6.2. Key boom configurations obtained from the simulation are displayed in Figure 6.3.

As expected, the initial boom equilibrium state has two localized bends as in Figure 6.3(a). As the displacement of one side was increased, the localized bends increase in radius; see Figure 6.3(b).

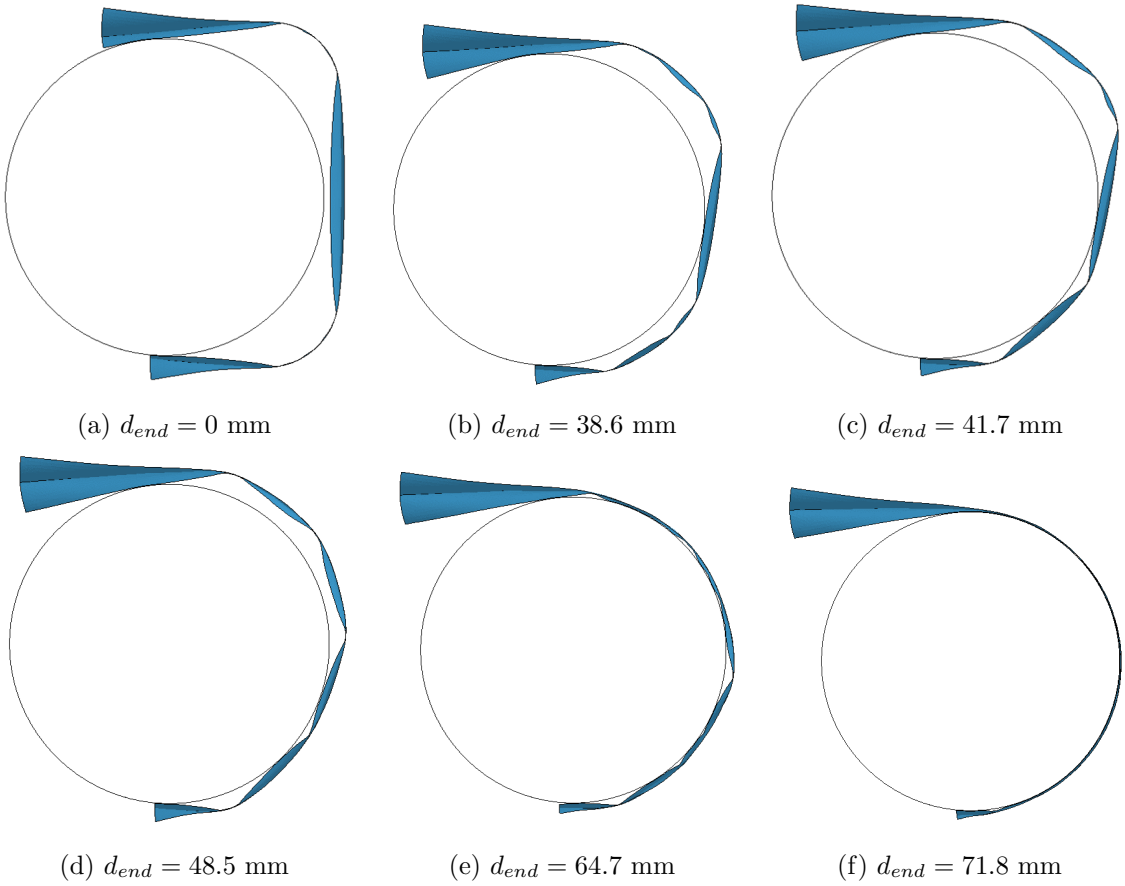

(a) $d_{end} = 0$ mm (b) $d_{end} = 38.6$ mm (c) $d_{end} = 41.7$ mm

(d) $d_{end} = 48.5$ mm (e) $d_{end} = 64.7$ mm (f) $d_{end} = 71.8$ mm

Figure 6.3: Localized fold configurations that develop during the coiling of boom with uniform cross-section and bond region thickness of 0.142 mm. (a) Initial two-fold configuration, (b) configuration just before bottom fold bifurcates, (c) configuration when the bottom fold has bifurcated into two, (d) configuration after bifurcation to five folds, (e) flanges start to flatten instead of the localized folds bifurcating and, (f) fully coiled configuration

As the bend radii increase, the inner flange opens while the outer flange continues to conform to the localized bend radius. At $d_{end} = 41.7$ mm the bottom fold bifurcates in two. This trend continues, with another bifurcation at $d_{end} = 48.5$ mm. These bifurcations are reflected in the force plot shown in Figure 6.2. The sharp jumps correspond to fold bifurcations.

The coordinates of the bond region nodes were extracted and used to calculate the localized bend radius at $d_{end} = 0$, corresponding to Figure 6.3(a). In the simulation, R_i ranged from 35.4 to 39 mm, which is practically identical to the analytical prediction of 36 mm. The radius of curvature was lowest near the edges of the localized bend, and highest in the middle.

6.1.4 Coiling Experiments

An experiment was carried out to validate the simulations in Section 6.1.3. A cylindrical hub of diameter $d_{hub} = 165$ mm was rigidly attached to the base of an Instron materials testing machine. A composite TRAC boom with the same material properties as simulated in Section 6.1.3 was manufactured by Caltech graduate student Christophe Leclerc. This boom was clamped to the side of the hub, then folded around the hub, as per Figure 6.4. The other end was attached to the load cell of the testing machine. The force was recorded as this end was displaced vertically at a rate of 30 mm/min.

The experimental results highlight two aspects. First, the initial folded configuration is non-unique, and depends exactly on how the fixed end is clamped, and second, upon the method of folding. In Figure 6.4(a) there are initially four localized folds. In Figure 6.4(c) there are three and in Figure 6.4(e) there are only two. In Figure 6.4(a) and 6.4(b) one localized bend at the clamped end is obscured by the hub. The effect of the number of localized folds is evident in the corresponding force plots.

For all initial configurations, the tension force required is almost zero until the inner flange, in between the localized folds, comes into contact with the hub. At this point the tension force rapidly increases, which corresponds to $d_{end} = 48.2$ mm, 41.4 mm, and 38.8 mm for the four-fold, three-fold, and two-fold initial configurations respectively. In the two and three-fold initial configurations, the distance between localized folds is greatest, allowing the inner flange to open further and therefore come into contact with the hub sooner than the four-fold initial configuration. In two-fold initial configuration, the inner flange is compressed against the hub in only one place leading to a force plateau at 0.08 N. In the three-fold initial configuration the inner flange is in contact with the hub in two locations, and the resulting plateau is at 0.1 N.

The two-fold initial configuration is the closest to that modeled in LS-Dyna. Both the simulation and the experiment exhibit a force plateau, although in the experiment the plateau was measured at 0.08 N, compared with 0.1 N in the simulation. In addition, the simulation force increases from zero at $d_{end} = 12.7$ mm, much earlier than in the experiment at $d_{end} = 38.8$ mm. Finally, at $d_{end} = 0$ mm the localized folds in the simulation are much smaller than in the experiments.

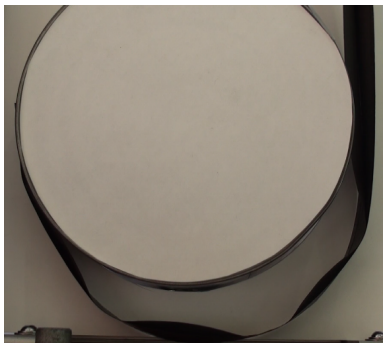

(a) Four fold initial configuration.

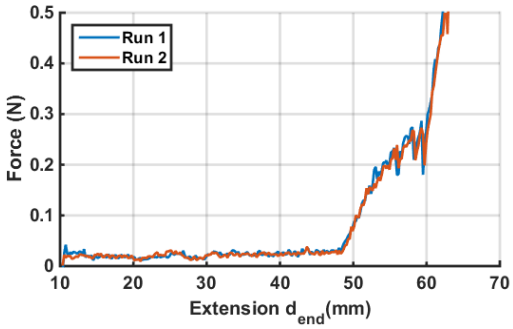

(b) Experiment forces corresponding to four fold initial configuration.

(c) Three fold initial configuration.

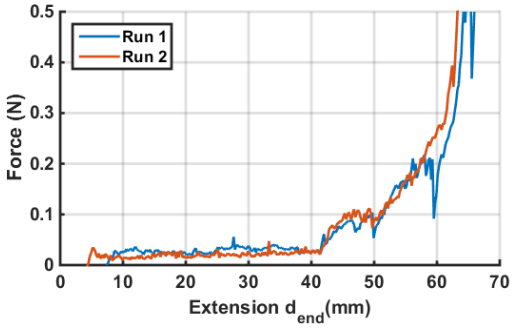

(d) Experiment forces corresponding to three fold initial configuration.

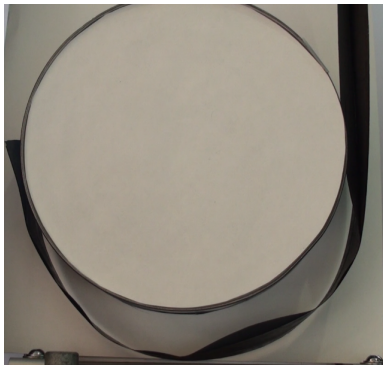

(e) Two fold initial configuration.

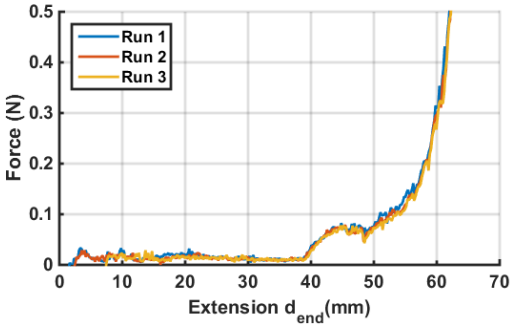

(f) Experiment forces corresponding to two fold initial configuration.

Figure 6.4: Left: Initial TRAC boom experimental folded configurations. The left end of the boom is rigidly mounted to the cylindrical hub, and the right end to an Instron tensile testing machine. Right: Corresponding force profiles obtained during coiling.

6.1.5 Capturing Imperfections in Boom Geometry

One reason the simulation in Section 6.1.3.2 did not accurately capture the experimental behavior is because the model did not account for the imperfections that exist in the boom that was tested. The laser scanner on a FaroArm portable coordinate measuring machine was used to obtain a point cloud of the TRAC boom surface. The point cloud data also captured that the boom is initially bent out-of-plane in the Y-direction, as shown in Figure 6.5(a). Additional measurements were taken with a micrometer to determine the thickness variation along the boom length. Figure 6.5(b) shows the thickness of the bond region, with measurements taken by a micrometer at 2 mm and 6 mm away from the edge of the bond region. With this information a new mesh was generated that included the initial Y displacement. In addition, the bond-region thickness was increased to 195 µm. The thicker bond region results in $D_{11,b} = 0.044$ Nm and from Equation 6.3, a localized bend of $R_i = 47$ mm. The flange radii and subtended angle were left unchanged and constant along the boom length.

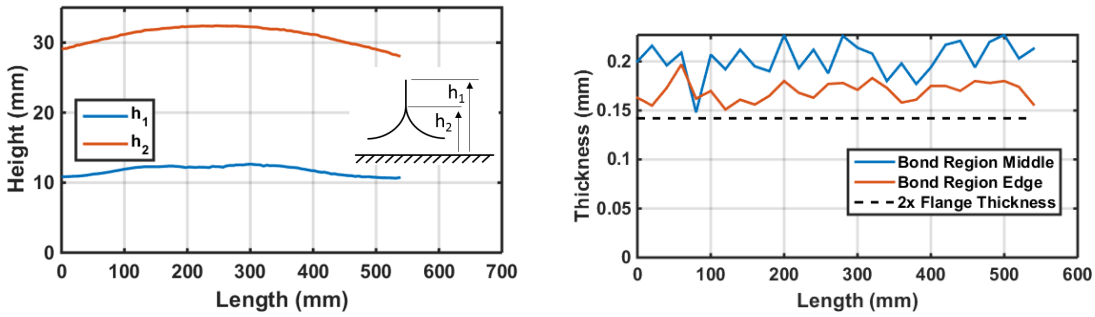

(a) (b)

Figure 6.5: Physical dimensions of the actual boom tested. (a) Height of bond region from a reference surface when boom is resting on its flanges. Note that the flanges are only in contact with the reference surface at Length = 0 and 535 mm. (b) Thickness of bond region along the boom length.

Figure 6.6(b) is a plot of the force results from the modified simulations together with the experimental data for the two-fold initial configuration. The inner flange between the two localized folds comes into contact with the hub at $d_{end} = 28$ mm, an improvement of 15 mm compared to the previous simulation. Once the inner flange in the corresponding experiment comes into contact with the hub at $d_{end} = 38$ mm there is close agreement between the experiment and simulation. The simulation saw-tooth force profile before $d_{end} = 28$ mm is a direct result of friction causing stick-slip

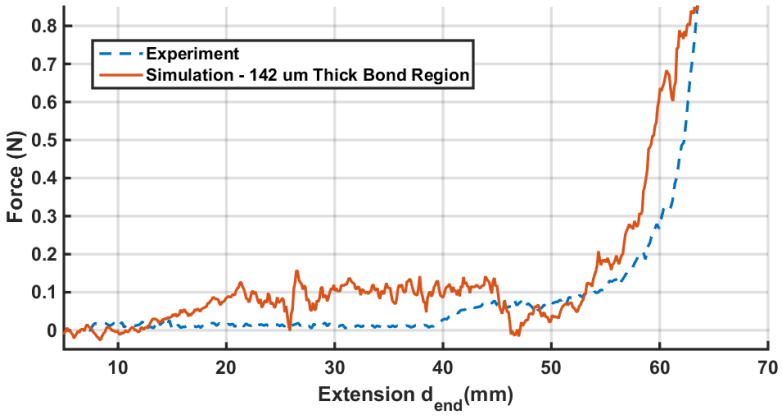

(a)

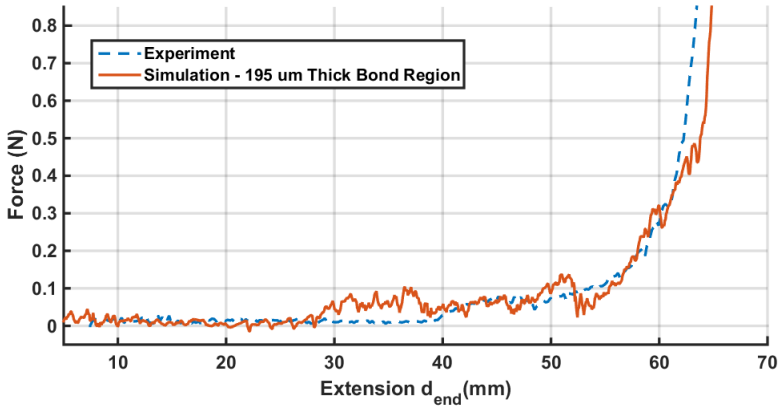

(b)

Figure 6.6: Comparison of experimental results with (a) nominal simulation with no imperfections and a modeled bond region thickness of 142 µm and (b) simulation incorporating manufacturing imperfections, including a bond region thickness of 195 µm.

behavior. The reason for the force plateau can be understood from Figure 6.7(b). The boom still has two localized folds which just increase in radius. The jumps in force between $d_{end} = 28$ mm and $d_{end} = 52.4$ mm correspond to both friction, and to the formation and bifurcation of smaller localized bends in the inner flange. Finally, at $d_{end} = 0$ the localized bend radius is $Ri = 49$ to 56 mm. This is larger than the estimate of 47 mm. The reason is that, even in the initial two-fold configuration, the inner flange opens out along the localized bend, as seen in Figure 6.8(a), while Figure 6.8(b) clearly shows the outer flange edge and bond region have almost identical curvatures. The opening of the inner flange relieves some of the bending energy in this flange, and results in a slightly larger radius of curvature in the bond region.

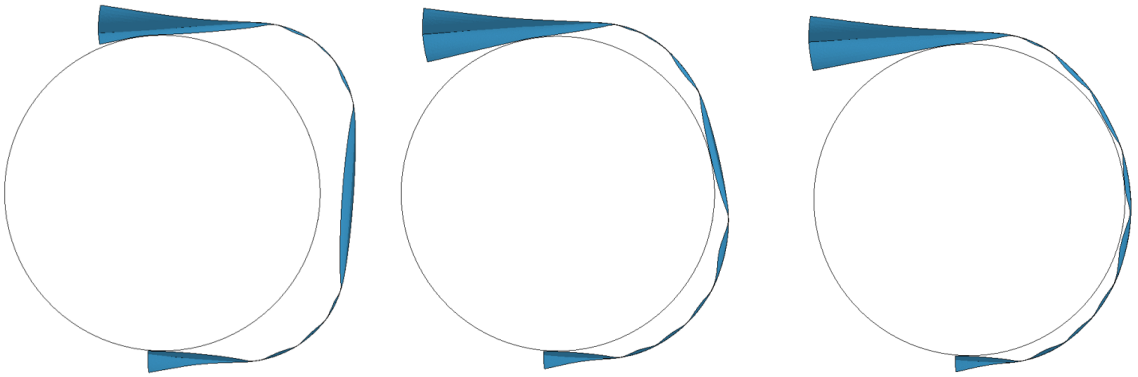

(a) $d_{end} = 0$ mm (b) $d_{end} = 38.8$ mm (c) $d_{end} = 52.4$ mm

Figure 6.7: Localized fold configurations that develop during coiling of boom with constant cross-section and bond region thickness of 0.195 mm. (a) Initial folded configuration, (b) the two localized folds have increased in radii, and (c) inner flange is in contact with the hub in multiple locations.

6.2 Unwrapping and Re-wrapping

The simulations in the previous section dealt exclusively with the tensioning of a TRAC boom around a hub. The case where a coiled boom is unloaded, that is, reducing the tension force, is also of interest since the force required to coil the boom may differ from the force required to keep it in the coiled configuration. Of particular interest is if during unloading the boom forms a global configuration of localized bends along the entire length of the boom.

6.2.1 Simulated Coiled Configuration

The simulation setup was based on the model in Section 6.1.3, and is shown in Figure 6.9. The simulation started with the boom in the fully deployed configuration; see Figure 6.9(a). To fold the boom into an initial single-fold configuration (Figure 6.9(b)) boundary conditions were applied to the flange edges to flatten the flanges at the two-fold location and where the boom initially touches the hub. After flattening, these boundary conditions were removed and contact with the two cylinders and hub enabled. The cylinders force the boom to remain flattened. Displacement boundary conditions were then applied to the left end of the boom, completely constraining the motion of the end as it was wrapped around two temporary cylinders.

Contact with the temporary cylinders was then removed and the boom allowed to find an equilibrium configuration. Damping was applied to remove excess kinetic energy. This resulted in

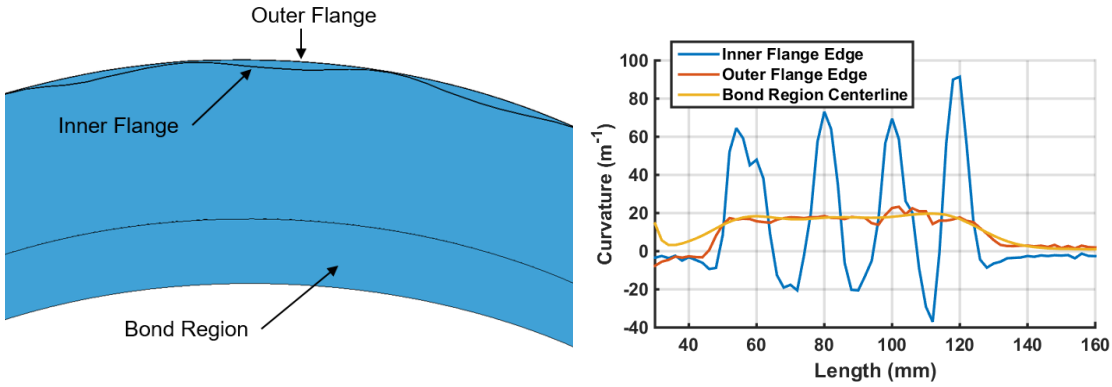

(a) (b)

Figure 6.8: (a) Close up of the localized fold closest to the clamped end in the initial folded configuration, corresponding to Figure 6.7(a). (b) Curvature of inner flange edge, outer flange edge and bond region centerline in the localized fold. Fold ends at length = 130 mm.

the single-fold configuration in Figure 6.9(b). Tension force of F_{max} was then applied to the boom end, tightly coiling the boom about a 90^o arc of the hub as shown in Figure 6.9(c). Finally, the hub and pinned end of the TRAC boom rotated about the hub axis, resulting in the coiled configuration of Figure 6.9(d). The exact boundary conditions, node sets and force loading curve is detailed in Appendix C.

The effect on the uncoiling force of the simulation time, magnitude of F_{max}, type of the end boundary condition, length of uncoiled boom and wrapped angle were investigated. The length of the uncoiled boom and wrapped angle were found to be the important factors.

6.2.2 Effect of Uncoiled Length on Unloading

To determine the effect of the uncoiled length on the unloading behavior of a coiled boom, booms with lengths of $420 \leq L \leq 600$ mm were coiled 225^o around a hub with diameter 165 mm.

A schematic of the coiled configuration is shown in Figure 6.10(a), with the simulation results in Figures 6.10(b) to 6.10(c). The key outcome is that the free length L_F of the boom changes the the unloading behavior of the boom. For relatively short L_F, such as $L_F = 95$ mm, the inner flange opens and forms multiple localized bends in along the entire lenth of the boom once the force drops below $F_{crit} \approx 0.12$ N as shown in Figure 6.10(c). For longer free length, of $L_F = 275$ mm, the localized bend at point B opens instead as shown in Figure 6.10(d).

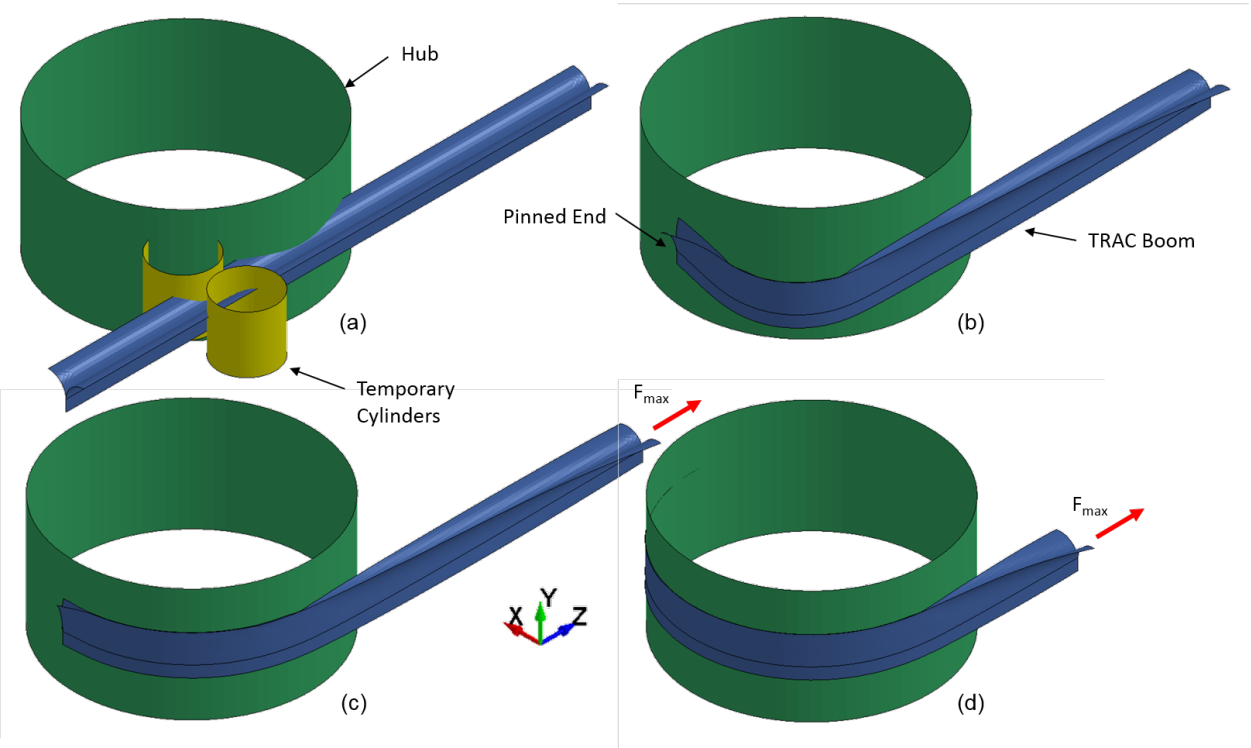

Figure 6.9: (a) Initial configuration of coiling simulation. (b) Boom folded with single localized bends and temporary cylinders removed. (c) Tension force F_{max} is applied, tightly wrapping boom about 90^o arc of the hub. (d) Hub and pinned end rotated about hub axis, coiling boom.

This behavior is caused by the normal force on the hub from the inner flange at point A. As the free length increases, the flange at point A can open further for a given tension force F. This has the effect of opening the localized fold further at point B, and changing the overall unloading behavior.

This effect is shown by the force profile in Figure 6.10(b). For $L_F = 275$ mm, the tip sharply deflects downwards at $F = 0.36$ N as the localized fold at point B opens. For the $L_F = 175$ mm case the localized fold opens slightly once the force drops below 0.36 N, but opens further at $F = 0.25$ N. For $L_F = 95$ mm, tip deflection caused by the localized fold opening occurs until the force drops to 0.12 N, then the sudden deflection change is caused by the inner flange opening in a global sense.

6.2.3 Unloading & Re-Loading Coiled Boom

The wrapping simulation was repeated for wrapped angles of 135^o, 190^o, and 225^o while keeping the free length fixed at $F_L = 95$ mm, as shown in Figure 6.11. Above 0.1 N, changes in tip displacement correspond to the localized fold at point B opening. When the force drops to $F_{crit} = 0.1$ N, the inner flange forms localized bends globally along the entire length of the boom, as illustrated in Figure 6.12.

Once the tension force reaches zero, the load was linearly increased to 0.6 N over 0.5 s. The reloading curve in Figure 6.11 differed for each simulation until $F = 0.47$ N. At this force the localized bends along the boom inner flange have conformed to the hub surface, leaving only the localized bend at point B. This force was consistent across the total wrapped angle.

6.3 Discussion

The localized bend radius of a carbon-fiber TRAC boom can be analytically determined when using Equation 5.1 as a starting point, the energy equation traditionally used for calculating tape spring localized bend radii. This radius can be calculated in terms of the flange and bond region properties, or purely the flange properties.

When wrapping TRAC booms, there are multiple equilibrium starting conditions. During wrapping, the localized folds increase in radius until they bifurcate in a manner similar to tape springs. As the localized folds grow, the inner flange opens, forming its own independent localized folds. These folds were experimentally observed in previous work, and were described as ‘triangular

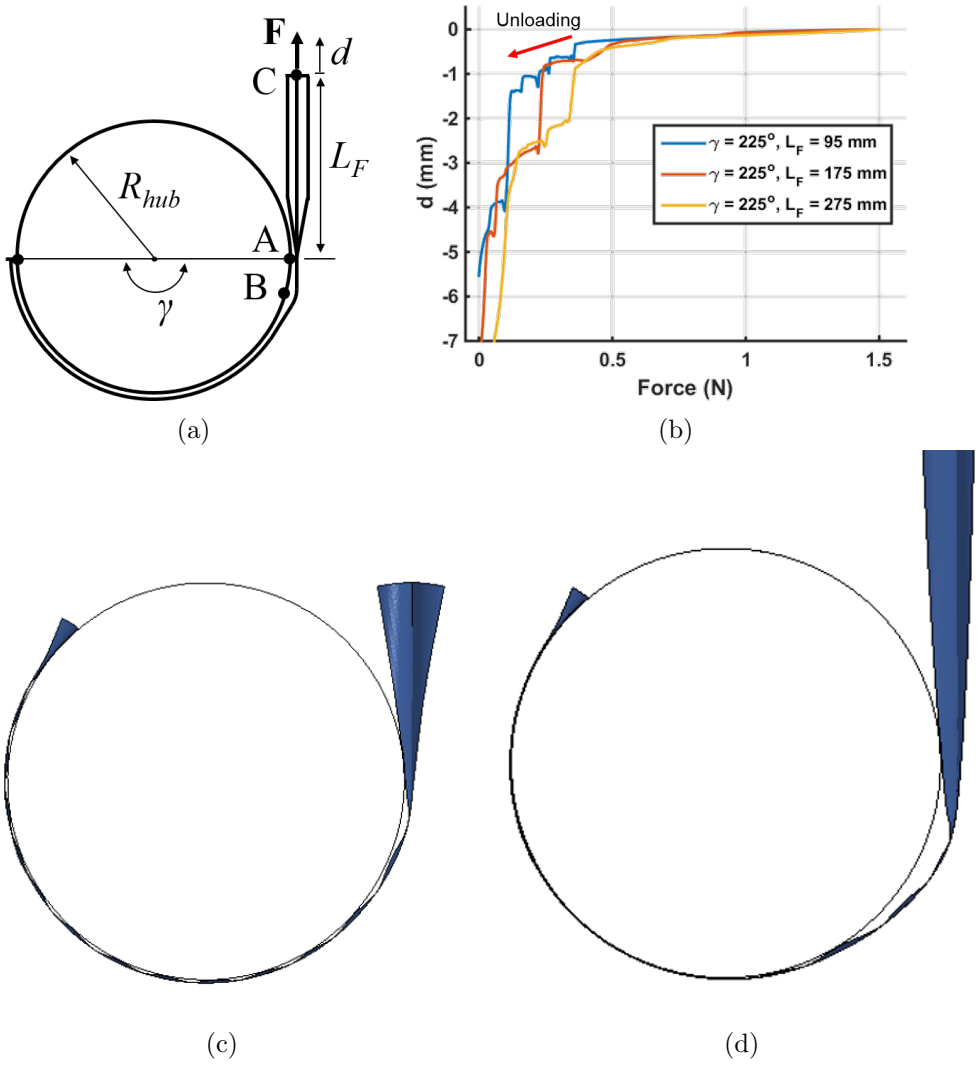

(a) (b)

(c) (d)

Figure 6.10: (a) Schematic of coiled boom, (b) Force vs tips deflection for unloading curve when controlling γ and varying free length L_F. (c) and (d) Boom configurations at $F = 0.1$ N for $L_F =$ 95 mm and 275 mm respectively.

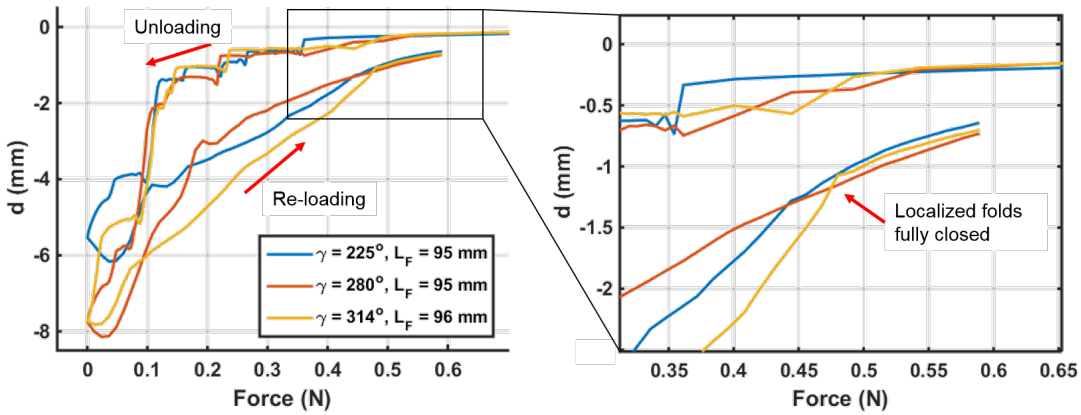

Figure 6.11: Unloading and loading force vs tip displacement when free length is fixed at $F_L = 95$ mm.

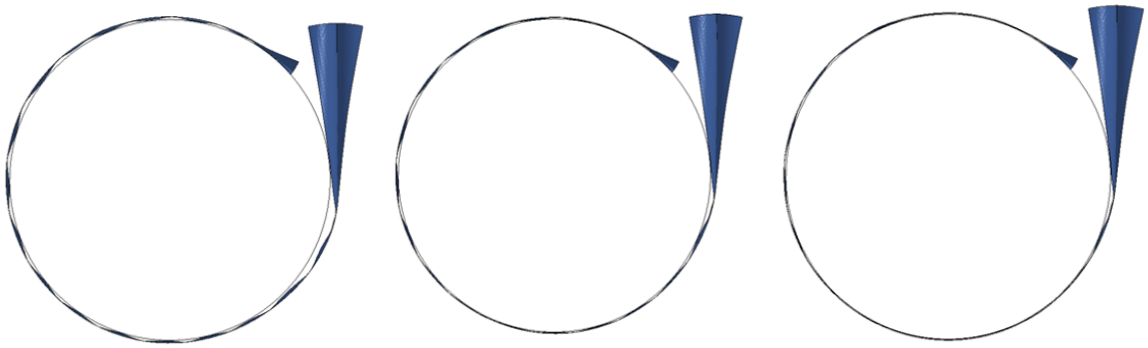

(a) (b) (c)

Figure 6.12: Top views of a boom wrapped to $\gamma = 225^o$ and initial free length of $L_F = 95$ mm, during re-loading of the boom after tension force has reached zero. Tension force is (a) 0 N, (b) 0.3 N, and (c) 0.444 N.

buckles' [34].

Like the ultra-thin carbon fiber tape springs in Section 5.5, capturing the actual physical cross-section is required to obtain the actual wrapping force profile. In addition, if the thickness of the bond region is more than double the flange thickness the localized bend radii will increase according to Equation 6.3.

Once fully wrapped, the TRAC boom can be unloaded and then reloaded. During unloading, the localized bend where the free end meets the hub increases in size. Once the tension force drops below a critical value, the small localized folds form in the inner flange along the entire length of the boom. The free length of the boom changes the unloading behavior significantly. The longer the free length, the larger the localized fold where the free end meets the hub is for a given tension force.

Neglecting friction, the coiling angle does not affect the unloading behavior significantly, and the critical unloading force remains constant for a given free length. Upon reloading, all the localized folds that formed in the inner flange, close at a fixed force, independent of the wrapped angle. For the carbon fiber TRAC boom simulated, this force was 4.5 times the magnitude of the critical unloading force, where the inner flange forms localized folds along the entire length.

Chapter 7

Conclusions and Future Work

Ultralight deployable structures are an important component of modern spacecraft. These include creased thin-film sheets that are used in solar sails, drag sails, and deployable antennae, as well as deployable booms such as tape springs and TRAC booms. Ground testing of these structures is highly challenging. Gravity can cause sagging, and air resistance reduces deployment speed, both of which change the deployment dynamics. The solution is to use computer modeling to predict the deployment behavior of these ultralight structures, and validate these models with ground tests.

This thesis has two broad research objectives: firstly, to develop and validate a technique for modeling creased thin-films in commercial FEA software, including packaging, and deployment behavior and forces, and secondly, to use numerical analysis to understand and predict the wrapping behavior of tape springs and TRAC booms.

7.1 Modeling Creased Thin-Film Structures

The modeling of thin-films containing multiple creases traditionally requires custom models developed for a particular application such as the IKAROS solar sail mission. This thesis shows the deployment behavior of a creased sheet can be captured in commercial FEA packages when modeling the creases as a row of pin joints with zero bending stiffness. In particular, the equilibrium configurations and peak forces experienced during deployment match experimental results. In addition, the MCFF approach has been developed, which allows creased sheets to be folded into a packaged configuration. The resulting deployment behavior has been compared with the corresponding behavior of a simulation starting in an approximated folded configuration. The use of folding forces in MCFF ensures the folded configuration contains straight, uncrumpled creases.

7.2 Tape Springs and TRAC Booms

An analytical model to determine when the localized folds in a tape spring will bifurcate was developed and validated against simulation results. Simulations and experiments of wrapping an isotropic tape spring around a hub 4.125 times the localized fold radii were performed.

Fold bifurcation is highly path dependent. Which particular localized fold will bifurcate, and at what point in the wrapping process, depends heavily on which previous localized fold bifurcated. LS-Dyna simulations were able to accurately capture the first three bifurcations, including the associated forces. Tuning the viscous damping allowed four bifurcations to accurately match the experimentally observed behavior.

This model was extended to a range of hub radii that differed from the tape spring localized bend radius. A linearly increasing trend in the force required to completely wrap the tape springs was observed for wrapping tape springs around hubs where at least one bifurcation occurs.

These wrapping simulations were extended to ultra-thin composite tape springs and TRAC booms. To obtain agreement with experiment, the exact cross-section was found via laser scanner and mapped to the simulation meshes. Excluding the effect of manufacturing imperfections results in a different bifurcation path during wrapping.

Simulations of loading and unloading of a coiled carbon fiber TRAC boom were performed. The length of the uncoiled boom has a significant impact on the uncoiling behavior. Shorter lengths result in the inner flange of the TRAC boom forming multiple localized folds along the entire length of the boom and opening in a global sense. Longer lengths result in a single localized fold increasing in size instead of the global response. Finally, when re-loading the TRAC boom, the force when the inner flange fully closes is consistent across wrapped angles, and for the case simulated, 4.5 times higher than the unloading force when the inner flange opened.

This is important when using tape spring and TRAC booms in space applications. Firstly, when wrapping long booms the coiled radii will be significantly longer than the natural bend radius. Secondly, tension force is required to fully coil the boom, and the force linearly increases with the coiled radius for tape springs. During deployment of the boom, either tension on the boom is required or an external cage that moves inwards and keeps the boom tightly wrapped. Otherwise the inner flange will open and form localized folds, potentially leading to the boom jamming during deployment.

7.3 Future Work

To further develop the work presented in this thesis, the next logical steps are:

1. Expand the problems tackled by the MCFF model to larger creased sheets
2. Validate the removal of crease bending moment on other crease patterns
3. Refine the magnitudes of the folding forces used in the MCFF approach so less iteration is required
4. Perform TRAC boom simulations for uncoiling and re-loading for larger hub diameters
5. Determine if the linear trend in tension force required to fully wrap an isotropic boom extends beyond $R_{hub} > 6R_i$, and confirm this relationship holds true for TRAC booms as well
6. Design and build mechanisms capable of applying sufficient tension on wrapped TRAC booms during deployment, to avoid the inner flange from opening.

Bibliography

[1] Abaqus, V. 6.14 documentation. *Dassault Systemes Simulia Corporation* (2014).

[2] Arenberg, J., Flynn, J., Cohen, A., Lynch, R., and Cooper, J. Status of the jwst sunshield and spacecraft. In *SPIE Astronomical Telescopes+ Instrumentation* (2016), International Society for Optics and Photonics, pp. 990405–990405.

[3] Arya, M., and Pellegrino, S. Deployment mechanics of highly compacted thin membrane structures. In *AIAA Spacecraft Structures Conference* (2014).

[4] Banik, J., and Murphey, T. Performance validation of the triangular rollable and collapsible mast.

[5] Belytschko, T., Liu, W. K., Moran, B., and Elkhodary, K. *Nonlinear finite elements for continua and structures*. John wiley & sons, 2013.

[6] Biddy, C., and Svitek, T. Lightsail-1 solar sail design and qualification. In *Proceedings of the 41st Aerospace Mechanisms Symposium* (2012), Jet Propulsion Lab., National Aeronautics and Space Administration Pasadena, CA, pp. 451–463.

[7] Block, J., Straubel, M., and Wiedemann, M. Ultralight deployable booms for solar sails and other large gossamer structures in space. *Acta Astronautica 68*, 7 (2011), 984–992.

[8] Calladine, C. The theory of thin shell structures 1888–1988. *Proceedings of the Institution of Mechanical Engineers, Part A: Journal of Power and Energy 202*, 3 (1988), 141–149.

[9] Daniel, I. M., Ishai, O., Daniel, I. M., and Daniel, I. *Engineering mechanics of composite materials*, vol. 3. Oxford university press New York, 1994.

[10] Estvanko, B., Maji, A., and Ng, P. Numerical analysis of a tape spring hinge folded about two axes. In *Earth and Space 2012@ Engineering, Science, Construction, and Operations in Challenging Environments* (2012), ASCE, pp. 714–721.

[11] Fang, H., Lou, M., and Hah, J. Deployment study of a self-rigidizable inflatable boom. *Journal of spacecraft and rockets 43*, 1 (2006), 25–30.

[12] Guest, S. D., and Pellegrino, S. Inextensional wrapping of flat membranes. In *Proceedings of the First International Seminar on Structural Morphology* (September 1992), pp. 203–215.

[13] Hallquist, J. O. *LS-DYNA keyword users manual*, 970 ed. Livermore Software Technology Corporation, 2007.

[14] Huang, H., Hagman, A., and Nygrds, M. Quasi static analysis of creasing and folding for three paperboards. *Mechanics of Materials 69*, 1 (2014), 11–34.

[15] Hull, S. NASA orbital debris requirements and best practices.

[16] Jeon, S., and Murphey, T. Design and analysis of a meter-class cubesat boom with a motor-less deployment by bi-stable tape springs. In *52nd AIAA/ASME/ASCE/AHS/ASC Structures, Structural Dynamics and Materials Conference 19th AIAA/ASME/AHS Adaptive Structures Conference 13t* (2011), p. 1731.

[17] Johnson, L., Whorton, M., Heaton, A., Pinson, R., Laue, G., and Adams, C. NanoSail-D: A solar sail demonstration mission. *Acta Astronautica 68*, 5 (2011), 571–575.

[18] Kumar, P., and Pellegrino, S. Kinematic bifurfactions in the simulation of deployable structures. In *Computational Methods for Shell and Spatial Structres* (2000), M. Papadrakakis, A. Samartin, and E. Oñate, Eds.

[19] Lappas, V., Adeli, N., Visagie, L., Fernandez, J., Theodorou, T., Steyn, W., and Perren, M. Cubesail: A low cost cubesat based solar sail demonstration mission. *Advances in Space Research 48*, 11 (2011), 1890–1901.

[20] Lechenault, F., Thiria, B., and Adda-Bedia, M. The mechanical response of a creased sheet. *Physical Review Letters 112*, 24 (April 2014), 244301.

[21] Liu, K., and Paulino, G. H. Merlin: A matlab implementation to capture highly nonlinear behavior of non-rigid origami. In *Proceedings of the 4th International Association for Shell and Spatial Structures Symposium* (2016).

[22] Liu, T., Wu, Q., Sun, B., and Han, F. Microgravity level measurement of the Beijing drop tower using a sensitive accelerometer. *Scientific reports 6* (2016).

[23] LS-DYNA Aerospace Working Group. Modeling guidelines document, 2012.

[24] Mallikarachchi, H. *Thin-walled composite deployable booms with tape-spring hinges.* PhD thesis, University of Cambridge, 2011.

[25] Mallikarachchi, H., and Pellegrino, S. Quasi-static folding and deployment of ultrathin composite tape-spring hinges. *Journal of Spacecraft and Rockets 48*, 1 (2011), 187–198.

[26] Mallikarachchi, H., and Pellegrino, S. Deployment dynamics of ultrathin composite booms with tape-spring hinges. *Journal of Spacecraft and Rockets 51*, 2 (2014), 604–613.

[27] Mallol Parera, P. *Deployment Simulations of a Composite Boom for Small Satellites.* PhD thesis, KTH Royal Institute of Technology, 2013.

[28] Mann, T., Behun, V., Lichodziejewski, D., Derbes, B., and Sleight, D. Ground testing a 20-meter inflation deployed solar sail. In *47th AIAA/ASME/ASCE/AHS/ASC Structures, Structural Dynamics, and Materials Conference 14th AIAA/ASME/AHS Adaptive Structures Conference 7th* (2006), p. 1707.

[29] Mezits, J., Common, R. J., and Rusi, J. A. Apparatus for sealing and restraining the flexible pressure boundary of an inflatable spacecraft, Dec. 13 2005. US Patent 6,974,109.

[30] Mobrem, M., Peterson, L., Cormarkovic, V., and Montazersadgh, F. An evaluation of structural analysis methodologies for space deployable structures. In *4th AIAA Spacecraft Structures Conference* (2017), p. 0851.

[31] Moseley, H. *Mechanical Principles of Engineering and Architecture: With Illustrations on Wood.* Wiley, 1860.

[32] Murphey, T., Jeon, S., Biskner, A., and Sanford, G. Deployable booms and antennas using bi-stable tape-springs.

[33] Murphey, T. W., and Banik, J. Triangular rollable and collapsible boom, Mar. 1 2011. US Patent 7,895,795.

[34] Murphey, T. W., Turse, D., and Adams, L. Trac boom structural mechanics. In *4th AIAA Spacecraft Structures Conference* (2017), p. 0171.

[35] Murphy, D., McEachen, M., Macy, B., and Gaspar, J. Demonstration of a 20-m solar sail system. In *46th AIAA/ASME/ASCE/AHS/ASC Structures, Structural Dynamics and Materials Conference* (2005), p. 2126.

[36] Okuizumi, N., Azusa Mura, S. M., Sakamoto, H., Shirasawa, Y., and Mori, O. Small-scale experiments and simulations of centrifugal membrane deployment of solar sail craft "IKAROS.". In *52nd AIAA/ASME/ASCE/AHS/ASC Structures, Structural Dynamics and Materials Conference 19th AIAA/ASME/AHS Adaptive Structures Conference* (April 2011), p. 1888.

[37] Okuizumi, N., and Yamamoto, T. Centrifugal deployment of membrane with spiral folding: Experiment and simulation. *Journal of Space Engineering 2*, 1 (2009), 41–50.

[38] Olson, G., Pellegrino, S., Costantine, J., and Banik, J. Structural architectures for a deployable wideband uhf antenna. In *53rd AIAA/ASME/ASCE/AHS/ASC Structures, Structural Dynamics and Materials Conference 20th AIAA/ASME/AHS Adaptive Structures Conference 14th AIAA* (2012), p. 1836.

[39] Osborne, B., and Welch, C. Short duration reduced gravity drop tower design and development. *Journal of the British Interplanetary Society 65*, 2 (2012), 71.

[40] Papa, A., and Pellegrino, S. Systematically creased thin-film membrane structures. *Journal of Spacecraft and Rockets 45*, 1 (2008), 10–18.

[41] Peterson, L., and Mobrem, M. Structural analysis methodology for space deployable structures using a high performance parallel nonlinear finite element solver. In *4th AIAA Spacecraft Structures Conference* (2017), p. 0852.

[42] Rimrott, F., and Fritzsche, G. Fundamentals of stem mechanics. In *IUTAM-IASS Symposium on Deployable Structures: Theory and Applications* (2000), Springer, pp. 321–333.

[43] Sawada, H., Mori, O., Okuizumi, N., Shirasawa, Y., Miyazaki, Y., Natori, M., Matunaga, S., Furuya, H., and Sakamoto, H. Mission report on the solar power sail deployment demonstration of IKAROS. In *52nd AIAA/ASME/ASCE/AHS/ASC Structures, Structural Dynamics and Materials Conference 19th AIAA/ASME/AHS Adaptive Structures Conference 13t* (2011), p. 1887.

[44] Schenk, M., Viquerat, A. D., Seffen, K. A., and Guest, S. D. Review of inflatable booms for deployable space structures: packing and rigidization. *Journal of Spacecraft and Rockets 51*, 3 (2014), 762–778.

[45] Seffen, K., and Pellegrino, S. Deployment dynamics of tape springs. In *Proceedings of the Royal Society of London A: Mathematical, Physical and Engineering Sciences* (1999), vol. 455, The Royal Society, pp. 1003–1048.

[46] Shirasawa, Y., Mori, O., Miyazaki, Y., Sakamoto, H., Hasome, M., Okuizumi, N., Sawada, H., Furuya, H., Matsunaga, S., Natori, M., and Kawaguchi, J. Analysis of membrane dynamics using multi-particle model for solar sail demonstrator "IKAROS". In *Proceeding of 52nd AIAA/ASME/ASCE/AHS/ASC Structures, Structural Dynamics, and Materials Conference* (2011), pp. 1–14.

[47] Stabile, A., and Laurenzi, S. Coiling dynamic analysis of thin-walled composite deployable boom. *Composite Structures 113* (2014), 429–436.

[48] Stohlman, O. R., Fernandez, J. M., Lappas, V., Hillebrandt, M., Hühne, C., and Straubel, M. Testing of the deorbitsail drag sail subsystem. In *54th AIAA/ASME/ASCE/AHS/ASC Structures, Structural Dynamics, and Materials Conference* (2013), p. 1807.

[49] Thomas, G., Swenson, P., Cobb, R., Swenson, E., and Black, J. Prototype development and dynamic characterization of deployable cubesat booms. In *51st AIAA/ASME/ASCE/AHS/ASC Structures, Structural Dynamics, and Materials Conference 18th AIAA/ASME/AHS Adaptive Structures Conference 12th* (2010), p. 2907.

[50] Walker, S. J., and Aglietti, G. S. An investigation of tape spring fold curvature. In *Proceedings of the 6th International Conference on Dynamics and Control of Systems and Structures in Space* (2004), Citeseer.

[51] Watt, A. M. *Deployable structures with self-locking hinges*. PhD thesis, University of Cambridge, 2003.

[52] Whorton, M., Heaton, A., Pinson, R., Laue, G., and Adams, C. NanoSail-D: the first flight demonstration of solar sails for nanosatellites. *22nd AIAA/USU Conference on Small Satellites* (2008).

[53] Woo, K., and Jenkins, C. H. Analysis of crease-wrinkle interaction for thin sheets. *Journal of Mechanical Science and Technology 26*, 3 (2012), 905–916.

[54] Woo, K., Nandurkar, K., and Jenkins, C. H. Effective modulus of creased thin membranes. *Journal of Spacecraft and Rockets 45*, 1 (), 19–26.

[55] Yee, J., and Pellegrino, S. Composite tube hinges. *Journal of Aerospace Engineering 18*, 4 (2005), 224–231.

Appendix A

GP92 MCFF Simulation Details

This appendix provides the details of the exact forces and damping loads used to fold the GP92 crease pattern according to the MCFF approach, as outlined in Chapter 3. The GP92 crease pattern is shown in Figure A.1(a), and regions where loads are applied is shown in Figure A.1(b).

The final folding pressure, line and point loads applied to fold the GP92 crease pattern in LS-Dyna is shown in Table A.1.

Figure A.4 shows the viscous damping profile applied to remove the kinetic energy once the sheet was fully folded. Damping is applied four times, with rest periods without damping to allow internal strain energy to be converted into kinetic energy. This ensures that at the end of the damping step an equilibrium configuration has been found.

Region	Location
A	Crease $V_{i,0} - V_{i,7}$
B	Crease $V_{i,0} - V_{i,1}$
C	Crease $V_{i,1} - V_{i,2}$
D	Triangle $V_{i,0}V_{i,1}V_{i+1,0}$
E	Trapezoid $V_{i,0}P_0P_1V_{i+1,0}$
F	Vertex $V_{i,1}$

Table A.1: Regions corresponding to Figure 3.3. To generate the hill and valley folds, for i = even forces are downwards (-z), for i = odd, forces are upwards (+z).

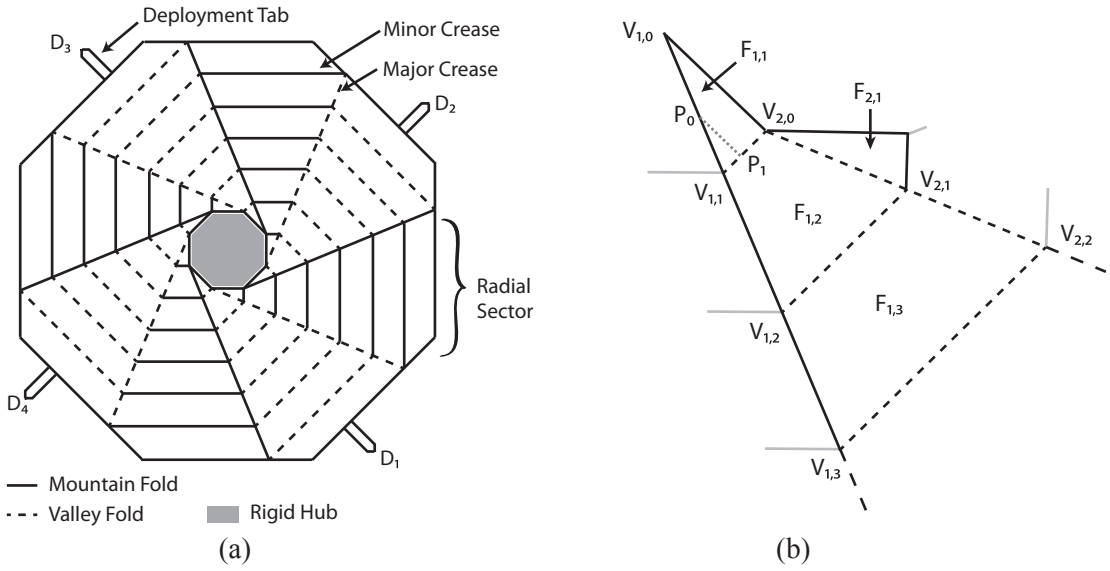

Figure A.1: (a) Test case GP92 crease pattern that enables wrapping a thin-film around a polygonal hub. Here there $n = 8$ major creases and $m = 6$ minor creases per radial sector. This corresponds to six quadrilateral and one triangular facets per radial sector. (b) First three facets in radial sector 1, facets are labeled $F_{i,j}$ and vertices $V_{i,j}$.

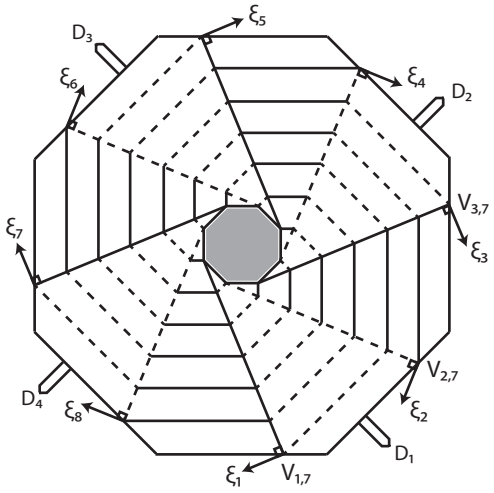

Figure A.2: GP92 fold pattern showing local coordinate directions ξ_i, associated with vertices $V_{i,7}$. To enforce symmetry these vertices are constrained to not move in ξ_i directions during folding. During the deployment stage radial displacement boundary conditions are applied to $D_1 - D_4$.

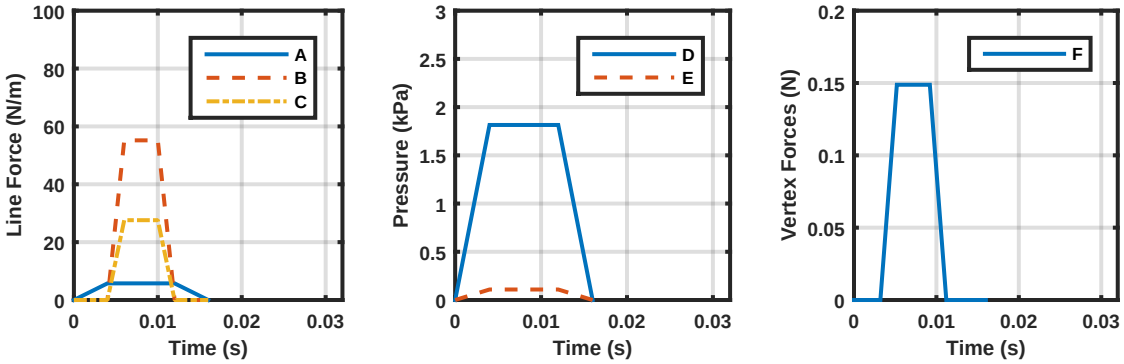

(a) (b) (c)

Figure A.3: Profiles of (a) line loads, (b) pressure loads and (c) point loads required to produce the wrapped state. These forces correspond to the regions defined in Table A.1

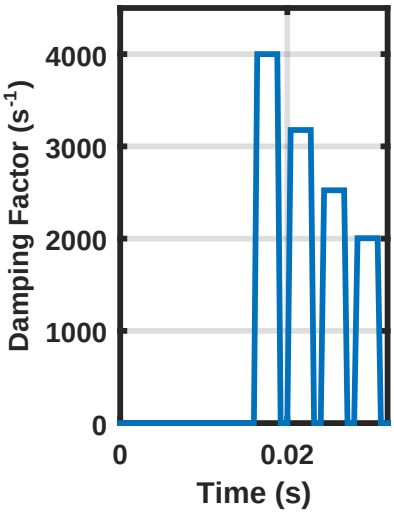

Figure A.4: Viscous damping profile applied after wrapping to remove kinetic energy and find an equilibrium rest state

Appendix B

Tape Spring Wrapping Simulation

Section B.1 contains the boundary conditions and corresponding figure showing the node sets for the simulations detailed in Section 5.3. Sections B.2 and B.3 detail the effect on the wrapping force profile when varying mass nodal damping and friction respectively. Section B.4 shows the effect that using fully integrated quadrilateral shell elements (Type -16) in LS-Dyna has on the same wrapping force profile.

B.1 Wrapping Simulation Details

The boundary conditions for the wrapping simulation in Section 5.3 are detailed in Table B.1 and the corresponding node sets defined in Figure B.1.

B.2 Effect of Varying Mass Nodal Damping

The effect of mass nodal damping on the tape spring wrapping simulations performed in Section 5.3.2 was investigated for a wider range of β values. Plots comparing the results for $\beta = 0.1$, 1, 10, 100, and 1000 s^{-1} against the experimental result are shown in Figures B.2(a) and B.2(b). There is a clear change in behavior between $\beta \leq 1$ s^{-1} and $\beta \geq 10$ s^{-1}. The friction coefficient for both the static and kinetic friction was set to the experimentally observed mean of $\mu = 0.185$.

Description	Time (s)	Node Set	Boundary Conditions Activated
Fix midline position as edges are flattened	0 - 0.06	Midline Nodes	$u_x = u_y = u_z = 0$
Edges are displaced to flatten tape-spring	0 - 0.04	Edge Nodes	$u_x = 3.7$ mm
Contact with cylindrical crushers enabled	0.04 - 0.06	All nodes	
Fix central nodes	0.00 - 0.20	Central nodes	$u_z = 0$
Tape spring ends controlled to create two localized bends	0.06 - 0.21	Tip 1 node	$u_y = f_1(t), u_z = g_2(t), u_y = 0$
Tape spring ends controlled to create two localized bends	0.06 - 0.21	Tip 2 node	$u_y = f_1(t), u_z = g_2(t), u_y = 0$
Fix midline to constrain out-of-plane motion	0.06 - 0.17	Midline Nodes	$u_y = 0$
Mass nodal damping applied to remove kinetic energy	0.17 - 0.21		$\beta = 100$
Match clamped end conditions	0.20 - ∞	Hole Nodes	$u_x = u_z = 0$
Match clamped end conditions	0.21 - ∞	Tip 2 node	$u_x = u_z = 0$
Damping applied to reduce kinetic energy during wrapping	0.21 - 11.5		$\beta = 1$
Top end displaced by 65 mm, tensioning tape spring	0.21 - 14.21	Tip 1 node	$u_y = 0$, $u_x = 65$ mm
Damping applied to reduce kinetic energy during wrapping	11.5 - 14.21		$\beta = 1000$

Table B.1: Boundary conditions for the simulation in Section 5.3. $f_1(t), f_2(t), g_1(t), g_2(t)$ were calculated with Equation 4.2

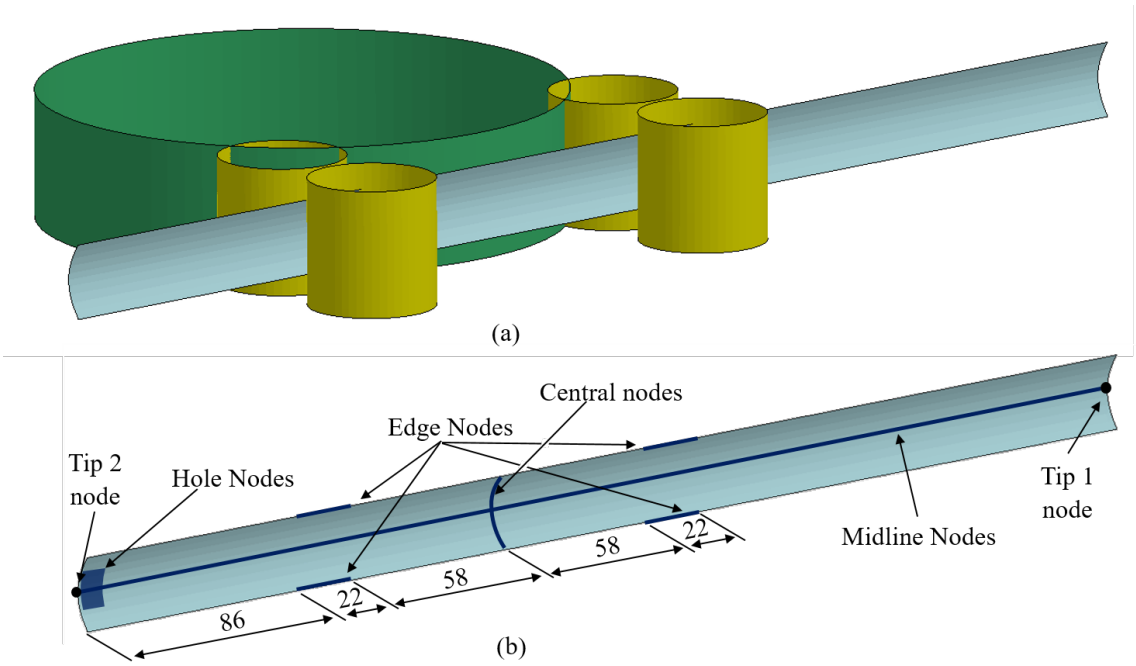

Figure B.1: (a) Initial setup of the tape spring wrapping simulations in Section 5.3. (b) Associated dimensions and node sets.

B.3 Effect of Varying Friction Coefficient

The friction coefficient between the tape spring and hub that was measured in Section 5.2.3 varied between 0.15 and 0.2, with a mean of 0.185 and a standard deviation of 0.016. While $\mu = 0.185$ was used in the simulations in Section 5.3, the effect of friction on the simulation was also studied. In particular, the wrapping simulation was repeated for $\mu = 0.15$, 0.16, 0.17, 0.18, 0.19, and 0.20, and the tension force results are shown in Figure B.3. For all simulations mass nodal damping was set to $\beta = 1\ \mathrm{s}^{-1}$.

As Figure B.3 shows, changes in μ do not lead to significant changes to the tension force magnitudes for a given configuration of localized folds. However, μ does have an effect on the bifurcation order, including which localized fold bifurcates and at what extension, d_{end}, the bifurcation occurs.

Regardless of the friction coefficient tested, the localized fold closest to the clamped region is the first fold to bifurcate. For $\mu \geq 0.18$, the larger friction coefficients correspond to the bifurcation occurring at large extensions.

Also for friction coefficients $\mu \geq 0.18$ the second bifurcation differs from that observed experimentally. In particular, the localized fold closest to the clamped region bifurcates for a second

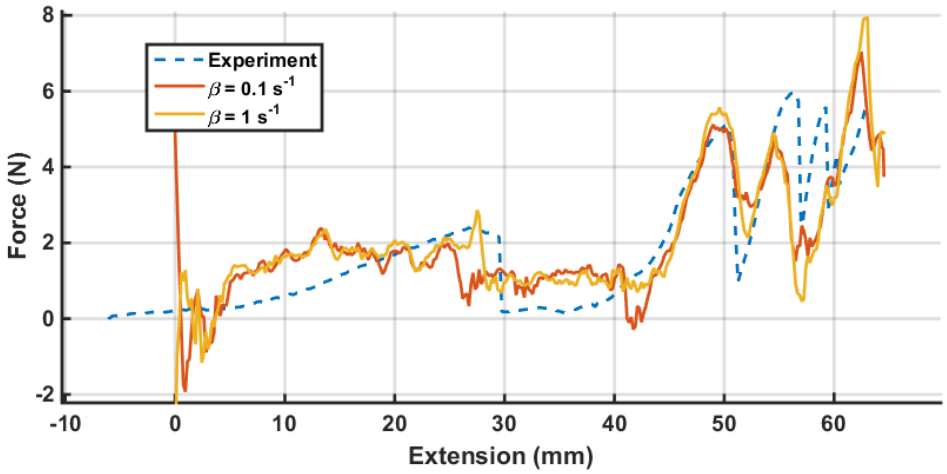

(a)

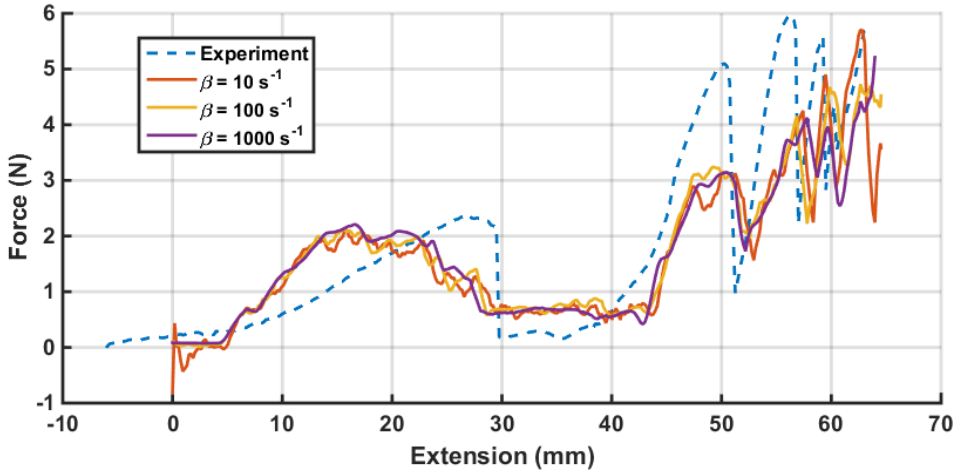

(b)

Figure B.2: Comparison of experimental results and simulation results with mass nodal damping set to (a) $\beta = 0.1 - 1$ s^{-1} and (b) $\beta = 10 - 1000$ s^{-1} for the entire wrapping simulation. The data has been smoothed with a 5 point moving average to remove noise.

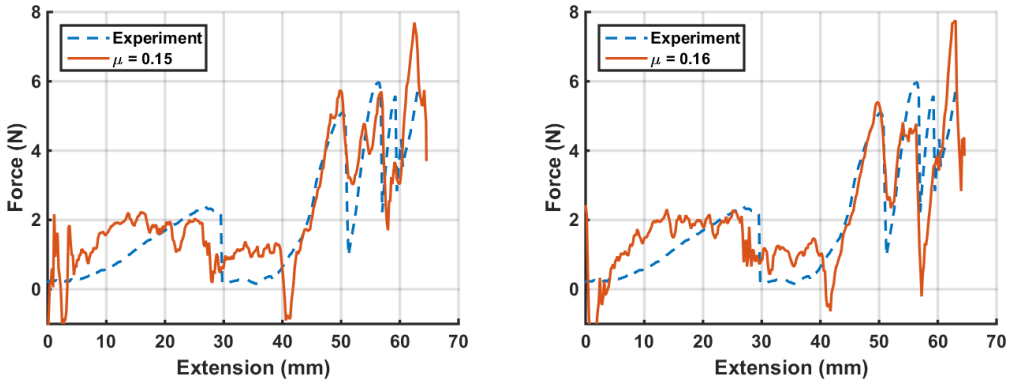

(a) $\mu = 0.15$

(b) $\mu = 0.16$

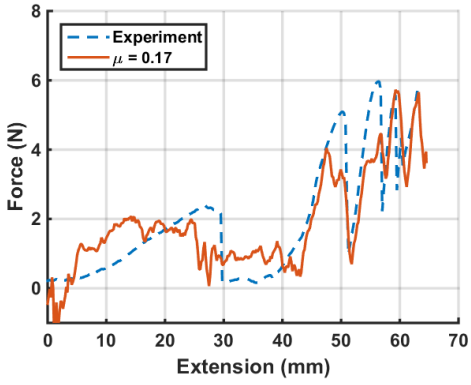

(c) $\mu = 0.17$

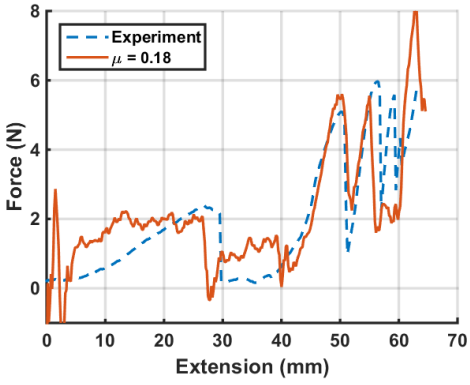

(d) $\mu = 0.18$

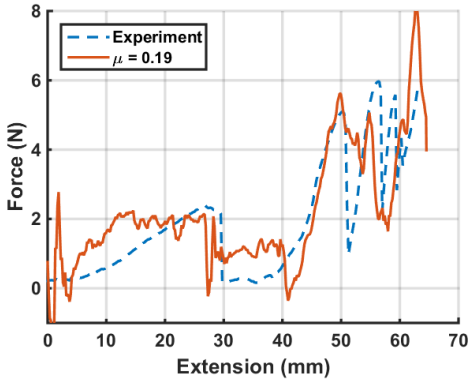

(e) $\mu = 0.19$

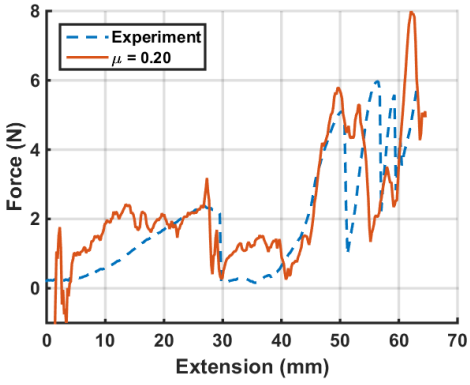

(f) $\mu = 0.20$

Figure B.3: Wrapping simulation tension force results when the static and kinetic friction coefficients (μ) are varied, plotted against the observed experimental result.

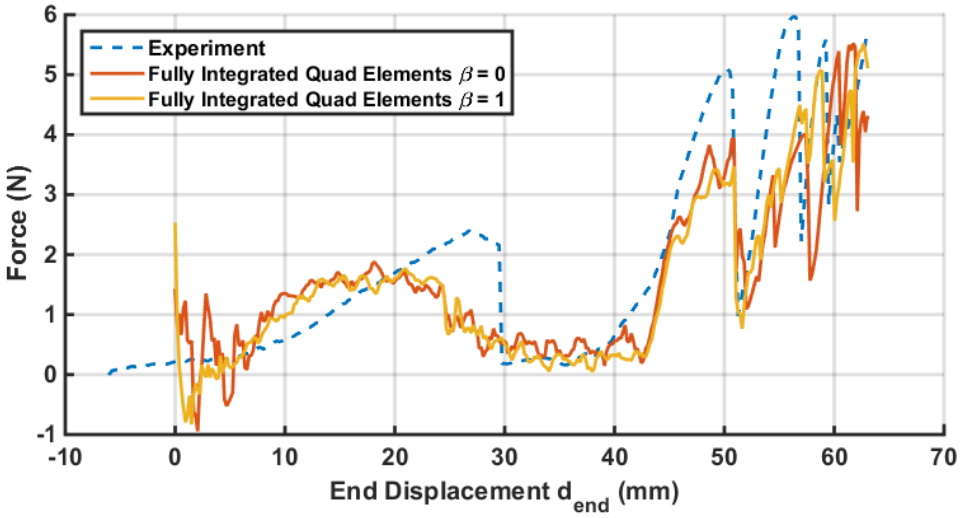

Figure B.4: Comparison of experimental results and simulation results with mass nodal damping set to $\beta = 0 - 1$ s^{-1} for the entire wrapping simulation. The data has been smoothed with a 5 point moving average to remove noise.

time, instead of the middle localized fold which is the case for $\mu < 0.18$. In addition, for $\mu \geq 0.19$ the third bifurcation occurs later, at $d_{end} = 55$ mm, without the sharp drop in tension force at $d_f = 0.51$ mm observed experimentally or for simulations with lower friction coefficients.

B.4 Effect of Meshing with Fully Integrated Quadrilateral Shells

The tape spring in Section 5.3 was also meshed with fully integrated quadrilateral shell elements (Type -16). The force profile observed during wrapping is shown in Figure B.4. Unlike the simulations where the tape spring was meshed with C^0 triangular shells, regardless of the viscous damping applied the wrapping simulations always moved down a different bifurcation path to the experiments when fully integrated quadrilaterals were used.

Appendix C

TRAC Boom Simulation Details

C.1 Wrapping Simulation Details

The boundary conditions for the wrapping simulation in Section 6.1.3 are detailed in Table C.1. and the corresponding node sets defined in Figure C.1.

C.2 Coiling, Uncoiling & Re-loading Simulation Details

The boundary conditions for the wrapping simulation in Section 6.2 are detailed in Table C.2 and the corresponding node sets defined in Figure C.1.

The tension force profile applied to the TRAC boom during coiling, unloading, and re-loading is shown in Figure C.2.

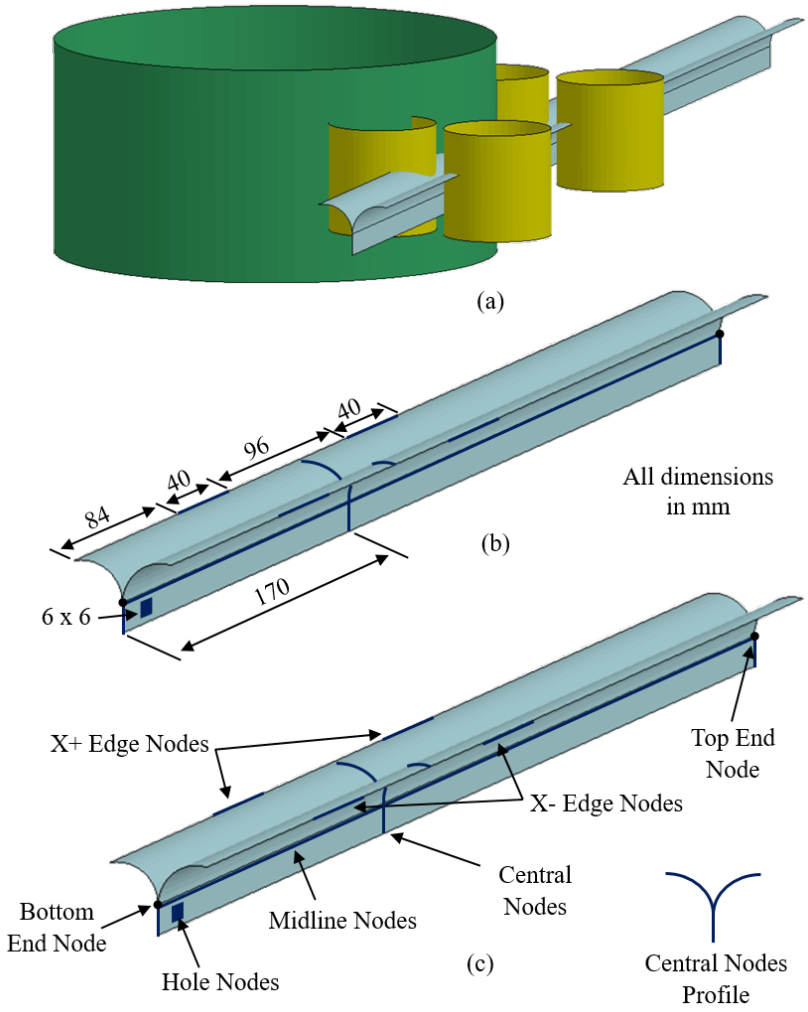

Figure C.1: (a) Initial setup of the TRAC boom wrapping and coiling simulations in Sections 6.1.3 and 6.2. (b), (c) Associated dimensions and node sets.

Description	Time (s)	Node Set	Boundary Conditions Activated
Fix midline position as edges are flattened	0 - 0.06	Midline Nodes	$u_x = u_y = u_z = 0$
X+ edges are displaced to flatten flanges	0 - 0.04	X+ Edge Nodes	$u_x = -11.4558$ mm
X- edges are displaced to flatten flanges	0 - 0.04	X- Edge Nodes	$u_x = 11.4558$ mm
Contact with cylindrical crushers enabled	0.04 - 0.06	All nodes	
Fix central nodes	0.00 - 0.20	Central nodes	$u_z = 0$
Fix central nodes	0.16 - 0.20	Central nodes	$u_x = 0$
Tape spring ends controlled to create two localized bends	0.06 - 0.21	Tip 1 node	$u_y = f_1(t), u_z = g_1(t), u_y = 0$
Tape spring ends controlled to create two localized bends	0.06 - 0.21	Tip 2 node	$u_y = f_2(t), u_z = g_2(t), u_y = 0$
Fix midline to constrain out-of-plane motion	0.06 - 0.17	Midline Nodes	$u_y = 0$
Mass nodal damping applied to remove kinetic energy	0.17 - 0.21		$\beta = 100$
Match clamped end conditions	0.20 - ∞	Hole Nodes	$u_x = u_z = 0$
Match clamped end conditions	0.21 - ∞	Tip 2 node	$u_x = u_z = 0$
Damping applied to reduce kinetic energy during wrapping	0.21 - 14.21		$\beta = 1$
Top end displaced by 70 mm, tensioning tape spring	0.21 - 14.21	Tip 1 node	$u_y = 0$, $u_x = 70$ mm

Table C.1: Boundary conditions for the simulation in Section 6.1.3. $f_1(t), f_2(t), g_1(t), g_2(t)$ were calculated from Equation 4.2

Description	Time (s)	Node Set	Boundary Conditions Activated
Fix midline position as edges are flattened	0 - 0.06	Midline Nodes	$u_x = u_y = u_z = 0$
X+ edges are displaced to flatten flanges	0 - 0.04	X+ Edge Nodes	$u_x = -11.46$ mm
X- edges are displaced to flatten flanges	0 - 0.04	X- Edge Nodes	$u_x = 11.46$ mm
Contact with cylindrical crushers enabled	0.04 - 0.06	All nodes	
Fix central nodes	0.00 - 0.20	Central nodes	$u_z = 0$
Fix central nodes	0.16 - 0.20	Central nodes	$u_x = 0$
Tape spring ends controlled to create two localized bends	0.06 - 0.21	Tip 1 node	$u_y = f_1(t), u_z = g_1(t), u_y = 0$
Tape spring ends controlled to create two localized bends	0.06 - 0.21	Tip 2 node	$u_y = f_2(t), u_z = g_2(t), u_y = 0$
Fix midline to constrain out-of-plane motion	0.06 - 0.17	Midline Nodes	$u_y = 0$
Mass nodal damping applied to remove kinetic energy	0.17 - 0.21		$\beta = 100$
Match clamped end conditions	0.20 - ∞	Hole Nodes	$u_x = u_z = 0$
Match clamped end conditions	0.21 - ∞	Tip 2 node	$u_x = u_z = 0$
Damping applied to reduce kinetic energy during wrapping	0.21 - 14.21		$\beta = 1$
Top end displaced by 70 mm, tensioning tape spring	0.21 - 14.21	Tip 1 node	$u_y = 0$, $u_x = 70$ mm

Table C.2: Boundary conditions for the simulation in Section 6.2. $f_1(t), f_2(t), g_1(t), g_2(t)$ were calculated from Equation 4.2.

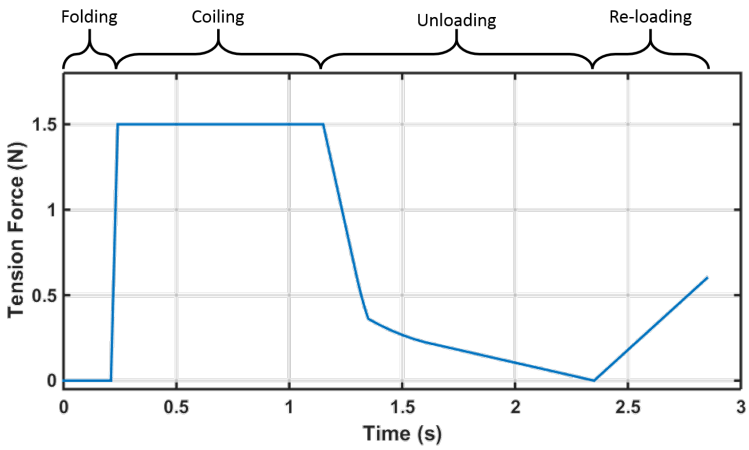

Figure C.2: Tension force profile applied to TRAC boom during coiling simulation in Section 6.2.